Mapping and Quantifying Early Tidal Wetland Evolution

Using Remotely Piloted Aircraft System Imagery and Object-Based Image Analysis

By
Reyhan Akyol

A Thesis Submitted to
Saint Mary's University, Halifax, Nova Scotia
in Partial Fulfillment of the Requirements for
the Degree of Master of Science in Applied Science.

March 2020, Halifax, Nova Scotia

Approved:	Danika van Proosdij, PhD Supervisor Department of Geography and Environmental Sciences
Approved:	Jeremy Lundholm, PhD Supervisory Committee Member Department of Biology
Approved:	Dirk Werle, MSc Supervisory Committee Member AERDE Environmental Research
Approved:	Peter Bush, PhD External Examiner Nova Scotia Provincial Government
Approved:	Adam J. Sarty, PhD Graduate Studies Representative Associate Vice-President, Research Dean, Faculty of Graduate Studies and Research

March 26th, 2020

Abstract

Mapping and Quantifying Early Tidal Wetland Evolution
Using Remotely Piloted Aircraft System Imagery and Object-based Image Analysis

By Reyhan Akyol

This research presents recommendations to effectively monitor the transition from former agricultural land back into salt marsh habitat following the dyke managed realignment at the Converse Marsh. For this analysis, two sets of multispectral RPAS imagery was collected pre- and a post-breach in September 2018 and May 2019 respectively. Both images were classified using Object-based Image Analysis (OBIA) and Random Forest, resulting in overall accuracies of 61% (Kappa 0.55) and 71% (Kappa 0.69). The results were compared with the Inundation Frequency to quantify classes by area and relative positioning. The use of OBIA is a feasible method for intertidal wetland delineation, however, it requires more objectivity in the process. The RGB camera and near-infrared sensor were missing critical sensitivity measures for radiometric calibration. The implementation of Random Forest proved to be a strong algorithm for intertidal habitat mapping. For future analysis, it is critical to have long-term tide recordings available.

March 26th, 2020

Acknowledgements

Firstly, I would like to thank my supervisor Dr. Danika van Proosdij for her indispensable support, guidance, and assistance throughout the entire journey of my Masters. I would also like to thank my supervisory committee members for their tireless support and feedback, especially in the last phase of finishing this work.

Thank you to everyone who contributed to the success of this research during my time at Saint Mary's University. Especially the team of MP_SpARC, InCoaST and CB Wetlands and Environmental Specialists. It was a great experience and pleasure to have been able to work with all of you.

Many thanks to Larissa Sweeney for her endless positivity and commitment to supporting me in my fieldwork and beyond. Thanks to Graeme Matheson for the countless hours of encouragement and being the best lab-friend, I could have wished for. Special thanks to Greg Baker for all the help with the RPAS, support with software related concerns and for sharing many clues that were so critical in all technical aspects of this research.

Vor allem möchte ich meinen Eltern für all die Liebe, Ermutigung und Unterstützung, die ihr mir stets entgegen gebracht habt, danken. Ohne euch und ohne meine Schwestern, Yasemin, Elif und Selma, wäre ich heute nicht hier, wo ich bin, und nicht der Mensch, der ich geworden bin. And Armando, thank you for being my best friend, my greatest supporter, and the best cheerleader for the past three years. I could not have imagined going through all these ups and downs without you and little baby Nova.

Table of Contents

List of Figures

List of Tables

Chapter 1: Introduction

1.1 Project Context and Goal

There are no accurate recordings of the historic loss of wetlands in Nova Scotia. Estimates show that approximately 80 percent of the salt marshes along the Bay of Fundy have been lost due to dyking for agricultural purposes beginning as early as in the 1700s (Byers & Chmura, 2007). As a consequence, the provision of ecosystem services and critical ecological functions decreased all across the Maritimes. The impact of human activities on coastal wetlands resulted in the loss of one of the most productive and diverse ecosystems on earth. They strengthen local biodiversity by providing food resources and habitat to fish, wildlife and plant populations. According to the Nova Scotia Wetland Conservancy Policy (Government of Nova Scotia, 2011), the Genuine Progress Index for Atlantic Canada assessed the remaining salt marshes in Nova Scotia and estimated monetary value of over 400 million Canadian Dollars per year by considering flood prevention, erosion control and protection of infrastructure against storm surges. Municipalities also show an increasing interest in conserving, constructing or restoring wetlands for water purification and to enhance the productivity of fisheries (Government of Nova Scotia, 2011; Tibbetts & van Proosdij, 2013). The province of Nova Scotia has developed the *No Net Loss of Wetlands* policy in response to the Environment Goals and Sustainable Prosperity Act (EGSPA) (Government of Nova Scotia, 2009). The greatest challenge for local jurisdictions is, however, related to the consequences of climate change. With the use of new technologies and advanced analysis methods, this research aims to develop best practice solutions to decrease costs and increase efficiency when monitoring tidal wetland restoration in the Bay of Fundy.

The consequences of climate change and greenhouse gas emissions of the past will impact places and citizens of coastal regions and therefore urgently calls for proper strategies to ensure resiliency and sustainability of vulnerable upland areas (Daigle Enviro, 2017). According to the latest Intergovernmental Panel on Climate Change (IPCC) report (Working Group 1 of the Fifth Assessment Report), the averaged global surface temperature showed a linear trend in the warming of the Earth's atmosphere of 0.85 ℃ for the period 1880 to 2012. The report further states that based on consistent measurements from tide-gauge and satellite altimeter data, the mean rate of global averaged sea-level rise was 3.2 mm per year between the period 1993 and 2010. The scientists continue with high confidence that since the early 1970s, 75% of the observed global mean sea-level rise can be lead back to glacier mass loss and ocean thermal expansion due to the warming climate (IPCC, 2013). It is predicted that ocean temperatures will increase and accelerate polar ice sheets and land glacier melting, resulting in the rise of global sea-levels of about one metre by 2100 (Daigle Enviro, 2017). The rise in the global mean sea-level would bring an increase in flooding frequency and extent, and with that, the risk of flooding areas that are usually above the levels of astronomical high tides.

The predicted extreme weather events causing storm surges is especially significant for Atlantic Canada's coasts and the Bay of Fundy in particular (Shaw et al., 1998), emphasizing the importance of regional sea-level rise scenarios to improve the calculated and predicted consequences of global warming for Nova Scotia. Several studies considered the regional implications of sea-level rise and flooding scenarios based on projections from the IPCC Fifth Assessment Report and incorporated the regional components of isostatic and eustatic sea-level rise (Singh et al., 2007; Daigle Enviro,

2017). More specifically, the components of vertical land movement, land glacier and ice sheet meltwater redistribution, dynamic oceanographic effects, land water storage and expected increases in the tidal range in the Bay of Fundy. These calculations are extreme sea level predictions of regional sea-level rise and predicted to be 0.88 m (± 0.38) at a 95% uncertainty factor within the next century (Daigle Enviro, 2017). This number was calculated for the eastern part of the upper Bay of Fundy, applying to coastlines of Chignecto Bay, based on the Representative Concentration Pathway 8.5 (RCP8.5) projection of the IPCC Fifth Assessment Report (AR5) (Daigle Enviro, 2017).

The impacts of coastal flooding and erosion by the rise of sea-levels in Atlantic Canada increase the sensitivity of coastlines significantly and calls for immediate adaptation strategies to ensure resiliency and sustainability of local communities. In particular, the magnitude and frequency of extreme weather events causing more damaging waves and storm surge, amplifying the risk of flooding for the low-lying areas behind dykes. Moreover, fewer winter sea ice seasons as a response to warming ocean temperatures will further increase damage to coastal ecosystems and structures (Duarte et al., 2013; Daigle Enviro, 2017).

In Nova Scotia, dykes have been built to create and protect agricultural land. However now, since the low-lying coastal areas are facing more challenges, the same coastal defences can no longer be maintained at their current location in many areas around the Bay of Fundy. Dykes have to be breached and moved further back towards the upland to assure continuous protective functions and decrease vulnerability. One of the most sensitive environments on Canada's coasts are salt marshes and intertidal habitats in general, which are threatened by permanent inundation, erosion, and other risks, such as changes in rates of marsh accretion or storm surge due to coastal squeeze. Moving present

coastal defences further back would allow those habitats the opportunity to respond to the rising sea levels (Shaw et al., 1998). As a favourable consequence, salt marsh ecosystems are being restored, aiding with its many functions in climate change adaptation (Duarte et al., 2013; Bowron et al., 2015). In particular, there are three main qualities of salt marshes in the Bay of Fundy relevant in their adaptive function, as outlined by Singh et al. in 2007:

1) The ability of salt marshes to self-adapt with sufficient sediments available, providing material for vertical accretion as well as the minerals to support plant colonization.
2) The role of salt marsh systems in providing buffer zones between land and sea.
3) The long-term economic efficiency of salt marshes in comparison to the construction and maintenance of hard structures along the coasts.

The Nova Scotia Department of Agriculture (NSDA) carries the responsibility of maintaining 241 kilometres of dykes to protect roughly 16,000 hectares of valuable agricultural land in the province. While many of these dykes were topped to update their critical elevations in early 2000, there are still dykes at several location in the Bay of Fundy that are highly vulnerable to dyke overtopping caused by sea-level rise and storm surge (Tibbetts & van Proosdij, 2013; van Proosdij et al., 2018). The critical elevation in the Bay of Fundy is determined by calculating the average high tide plus approximately 0.61 metres for exposed dykes and less for the ones located upriver (van Proosdij & Page, 2012).

Due to the factors mentioned earlier, the Government of Canada provided funding through the Coastal Restoration Fund of the Department of Fisheries and Ocean and the

National Wetland Conservation Fund of Environment and Climate Change Canada to the *Making Room for Wetlands* project (www.transcoastaladaptations.com), which is co-led by Saint Mary's University and CB Wetlands and Environmental Specialists (CBWES Inc.). Within this project, academics and industry work together to find nature-based solutions related to promote and undertake climate change adaptation. The overall mission of this project is to help build climate resilient coastal communities and ecosystems by restoring natural processes.

In Nova Scotia, several monitoring projects are being carried out to follow the re-establishment of natural ecosystems and re-development of high habitat diversities in tidal marshlands to provide essential ecosystem services (Bowron et al., 2015). These efforts need strategic planning and management. With advanced knowledge of the evolution of tidal wetlands, these kinds of projects will provide a better understanding of restoring coastal salt marsh trajectories in the Bay of Fundy; they are also leading to greater insights for planners, consultants, and scientists, thereby contributing to higher success rates in future managed realignment projects.

Reliable tools need to be developed to support the strategic planning of coastal land management. Notably, the quantitative assessment of vegetation and geomorphic recovery in restoration projects can provide important indicators about factors driving or limiting a recovering system. Frequent monitoring during the first few years of a breach event can provide key answers about the recovery of salt marsh systems in highly turbid macro-tidal environments and high suspended sediment concentrations (Bowron et al., 2012). In addition, monitoring can help to better manage and alleviate the physical changes in intertidal systems which in turn profoundly impacts socio-economic and ecological components of adaptation and mitigation planning (Shaw et al., 1998).

In order to support restoration activities in Nova Scotia, this research study deployed different types of sensors mounted on a Remotely Piloted Aircraft to collect hyper-spatial imagery ranging across several spectral bands of the electromagnetic spectrum to monitor and quantify the evolution of an intertidal habitat following managed dyke realignment at the Converse site in the upper Bay of Fundy. The imagery was first collected before the dyke breach, and once again about five months after the dyke was breached and tidal flow was re-introduced to the previously protected fallow agricultural land. To further improve the accuracy and reliability of this assessment, the images were classified using the method of Object-based Image Analysis and machine learning algorithms. It further tests the feasibility of the application of RPAS imagery with an attached near-infrared sensor and the use of machine learning algorithms for the classification. The technology and methods applied in this study will further be explained in more detail in later chapters of this work. In sum, this research provides a framework and recommendations for the implementation of Object-based Image Analysis for quantifying the evolution of a restoring salt marsh habitat.

1.2 Restoring Tidal Wetlands

Currently, there is one officially recognized classification system in Canada – the Canadian Wetland Classification System (CWCS). A marsh is one of the five wetland classes identified in the CWCS and is controlled by daily, seasonally or annually fluctuating water levels, often due to tides. Marshes can be further subdivided into different forms based on the source of water and basin topography. A common form in the Bay of Fundy is the tidal marsh. Tidal marshes develop in sheltered intertidal areas with available sediments under regular tidal saltwater flooding and no significant influence of

freshwater. Vegetation on tidal marshes is controlled by the duration of tidal exposure, slope gradients, distribution of tidal channels, and salinity (Warner & Rubec, 1997). Tidal marshes, also referred to as tidal wetland, inhabit a specific type of ecosystem, which is known as a salt marsh. By definition, a salt marsh is a vegetated wetland that is flooded regularly by tidal water or is influenced by salt spray or seepage, such that the water and soil are saline or brackish. These habitats are also known to exist within a network of tidal channels and often have ponds present (Province of Nova Scotia, 2017). The most recent wetland inventory by the Nova Scotia Department of Natural Resources (NSDNR) in 2004 indicates a total area of 17,060 hectares of salt marsh habitat in the province (Government of Nova Scotia, 2011). Most of it occurs in small pocket estuaries at river mouths or extends along existing dykes and shorelines in the Bay of Fundy (Bowron et al., 2012; Roman & Burdick, 2012). For the purpose of this study, tidal marshes, tidal wetlands, and salt marshes will be considered synonymous and used interchangeably throughout this work.

The high value of services provided by tidal wetland systems has been known for several decades (Bartlett & Klemas, 1980). Apart from the provision of habitat for ecologically significant species and protection of coastal zones from storm damage and high erosion rates, tidal wetlands are composed of the most fertile soils and ecosystems worldwide and have the ability to accumulate carbon (Figure 1.1) (Connor et al., 2001; Singh et al., 2007; Porter et al., 2015).

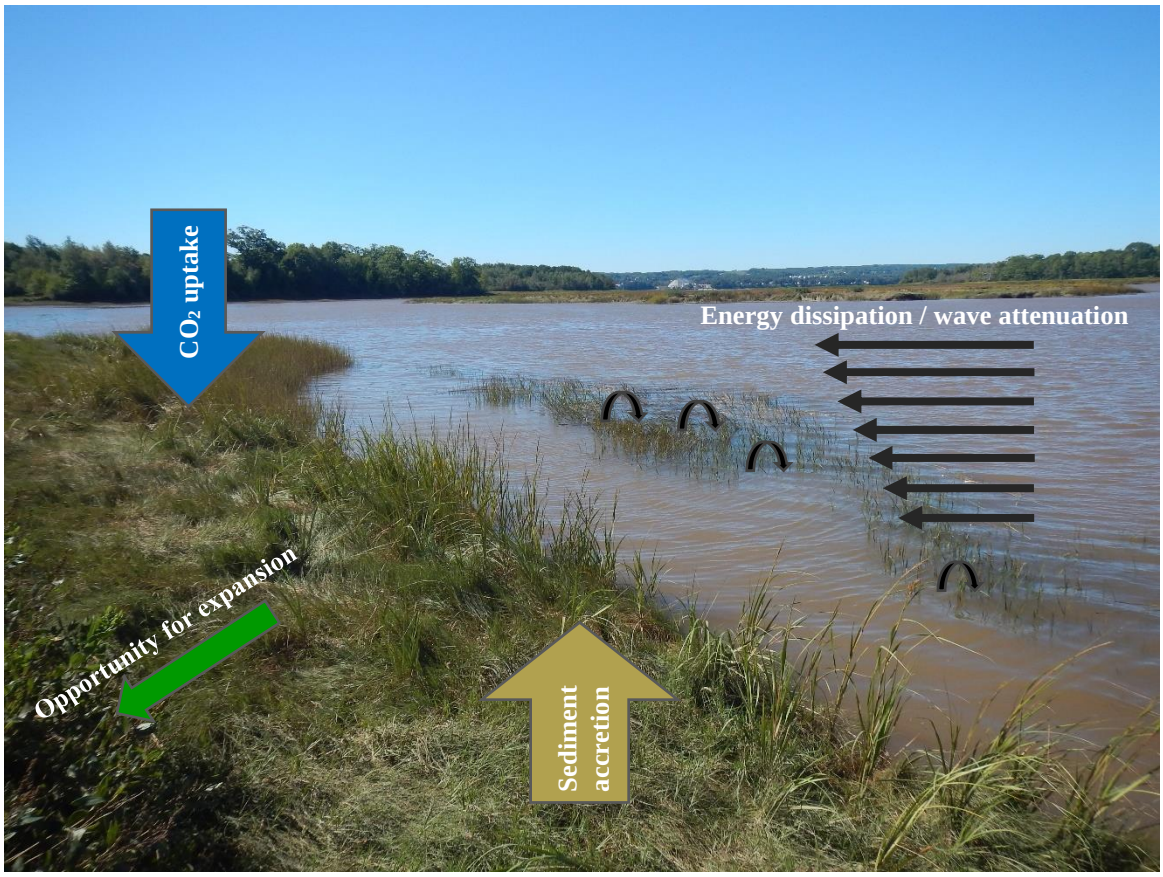

Figure 1.1: Services and natural functions provided by salt marshes to promote coastal resilience against the impacts of climate change (modified after Duarte et al., 2013) (Background Photo: Cogmagun site; Credits: Sweeney, L., 2018)

As discussed earlier, salt marshes are saline environments of the intertidal zones and are inhabited mainly by halophytic plant species (salt-tolerant plants). The saltwater inundation frequency and duration are the main drivers of patterns of salt marsh vegetation distributions. There are two main zones of differentiating salt marsh vegetation; the low marsh species formed by frequent and relatively long inundation times, and the high marsh species beginning just above the mean high water line characterized by less frequent flooding. The detailed marsh species composition within

each of the before named zones can vary depending on climate, soil, slope, sediment supply and many other factors (Tiner, 2013). In Nova Scotia, the low marsh zone is mainly dominated by *Spartina alterniflora* and the high marsh zone by *Spartina patens* (Porter et al., 2015).

Different physical and chemical drivers are essential for the structure and function of salt marshes in general. These variables include not only tidal flooding, frequency and duration but also soil salinity and permeability. Salt marshes can be found in tidal environments with sediment accumulation rates equal to or higher than land subsidence rates and appropriate coastal protection against erosion (Mitsch & Gosselink, 2015). Suspended sediment concentrations are critical factors for salt marshes to be resilient against rising sea-levels and restoration success (Singh et al., 2007). Large areas of early salt marsh colonizers developed on accreting intertidal flats through sufficient supply of these inorganic materials providing a high restoration potential in the Bay of Fundy (Bowron et al., 2012).

In the Maritime provinces of Atlantic Canada, salt marsh restoration is still in its infancy and has been focused mainly on sites with the most significant historical loss of salt marsh habitat – the Bay of Fundy. In Canada, there is still no provincially or federally specified guideline to plan, conduct and monitor salt marsh restoration projects. Before 2005, salt marsh habitat restoration activities were rather unanticipated consequences of other development projects in Nova Scotia, such as the construction of a causeway leading to new establishment or redistribution of tidal marshes, and only some of them were monitored long-term and in a systematic manner (van Proosdij et al., 2009; Bowron et al., 2012). Later, restoration efforts were conducted with the primary goal of recreating

salt marsh habitats, with extensive and ongoing monitoring efforts (Bowron et al., 2012). Today, the total area of restored tidal wetland habitats in the province of Nova Scotia has reached about 320 hectares (D. van Proosdij, personal communication, Dec. 2020).

There are three different methods of salt marsh habitat restoration that occur in the Bay of Fundy: a) passive restoration when a dyke is breached by natural causes and no human interference, b) active restoration through either a management decision to suspend the maintenance of a dyke, and c) planned removal or change of coastal barriers by modifying the site hydrology. Most of the active tidal salt marsh restoration projects in Nova Scotia principally build upon natural processes when they, for one, partially or wholly removed tidal gates, water control structures, or dykes; for another, installed culverts or bridges to re-introduce tidal flow to a marshland system successfully. Furthermore, some of the sites required more advanced restoration plans such as the creation of tidal channel networks and ponds to account for the heavily modified land morphology due to their agricultural use (Bowron et al., 2012).

Managed Realignment

Managed realignment, also known as a managed retreat or set back, is a relatively new approach in coastal management to protect against the impacts of wave energy and rising sea-levels (French, 2006). This approach follows the simple principle of returning land to the sea and with that allow the development of new salt marsh and intertidal mudflats behind the former barrier. For about the last two decades, coastal engineers and restoration practitioners have chosen this new soft engineering approach and relocated the land-sea line of defence landward due to landward movement of the mean low water mark caused by rising sea-levels and coastal squeeze. The most apparent benefits of this

technique come from wave attenuation and a decrease in the impacts of local sea-level rise, while they provide a valuable carbon sink for carbon dioxide from the atmosphere (Figure 1.1). Another, more common point, however, is the economic factor of choosing this type of nature-based approaches. Managed realignment often creates a more cost-efficient alternative for coastal protection than compared to the more common choice of maintaining and strengthening existing sea defences (ibid).

Fundamentally, the scientific technique of managed realignment builds upon the adaptation of intertidal environments to sea-level rise, which would eventually occur under natural conditions (Figure 1.2). However, by artificially creating this landward retreat, the salt marsh habitats are not allowed gradually to spread landward and upward following a natural profile along the coast. Rather, it introduces tidal waters into formerly protected lands in a very sudden movement. In most cases, the land to be restored had subsided over time and is at the time of the realignment not at the surface elevation as it would be under natural site conditions (French, 2006).

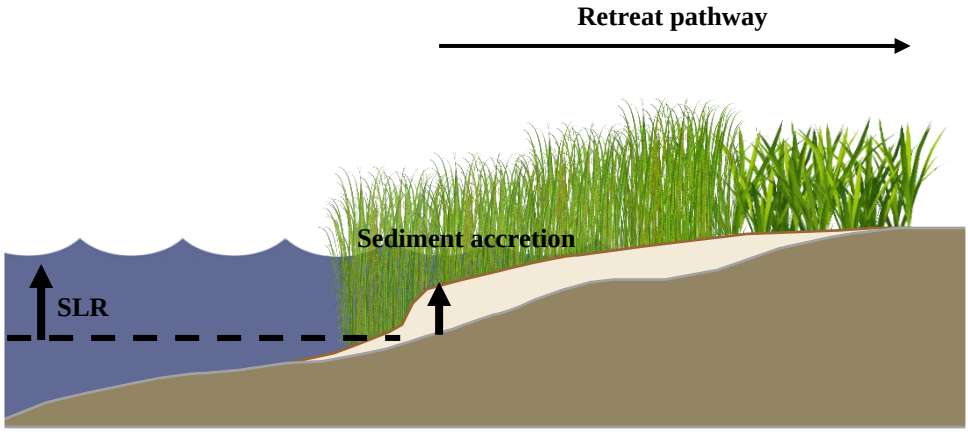

Figure 1.2: Natural adaptation of coastal marshes in response to sea-level rise is realized through vertical growth and retreat (modified after Mitchell & Bilkovic, 2019).

The complex nature of salt marsh reestablishment following managed realignment is evident by the several other examples from Europe and North America (French et al., 2000; Klötzli & Grootjans, 2001). The establishment of a reliable and efficient monitoring framework for managed realignment projects can provide more knowledge about constraining elements that may or may not influence a successful restoration outcome (Bowron et al., 2012). Advances in remote sensing and monitoring technologies present an opportunity to track the restoration trajectory of evolving tidal wetland landscapes in an innovative way.

1.3 Remote Sensing in Wetland Assessment

This study and its implementation rely on the discipline of remote sensing, which is adequately summarized and defined as: "*Remote sensing is the science (…) of acquiring information about the Earth's surface without actually being in contact with it. This is done by sensing and recording reflected or emitted energy and processing, analyzing, and applying that information*." (Canada Centre for Remote Sensing, 2015, pp. Fundamentals of Remote Sensing - Introduction). In remote sensing (RS), there are some critical technical terms, which need closer attention and clarification with regards to the "resolution" of any given image. The spatial detail of any image depends on the *spatial resolution* of the sensor and describes "*the size of the smallest possible feature that can be detected*" (Canada Centre for Remote Sensing, 2015, pp. Satellites and Sensors: Spatial Resolution, Pixel Size, and Scale). The spatial resolution is directly connected to an optical sensor's 'Instantaneous Field of View' (IFOV), which is an angular cone of visibility captured by the sensor of the Earth's surface at a given altitude and particular moment at a time. The actual area of the ground captured can then be calculated by

multiplying the IFOV by the distance from the surface to the sensor. The *spectral resolution* of any given image is the indicator of the width of each band of the sensor, showing the ability of a sensor to detect more or less reflectance values within each respective band (Canada Centre for Remote Sensing, 2015). With the spectral resolution, the importance of the *radiometric resolution* also comes into play. The radiometric resolution of an image describes the range in brightness levels on a grayscale. The finer the *radiometric resolution*, the higher the sensitivity of the sensor to record small variations in reflected or emitted energy. The associated brightness levels are recorded in binary numbers, which control the degree of detail each pixel can contain. With that, the maximum range of gray values in an image is dependent on the number of bits used to store the *radiometric information*. (Lavender & Lavender, 2016) (Figure 1.3).

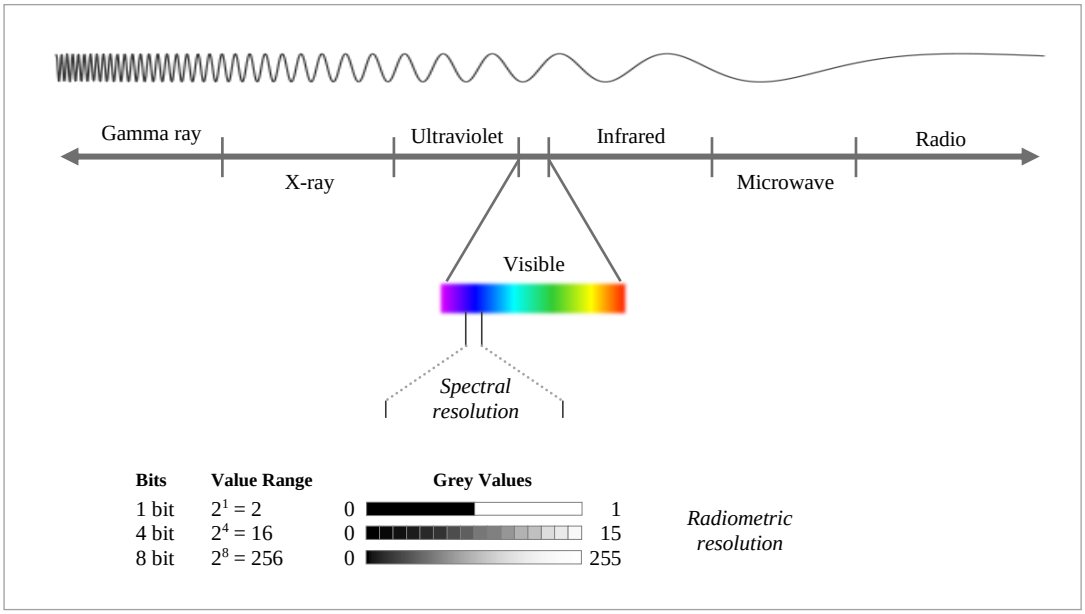

Figure 1.3: Electromagnetic spectrum outlining specifications of spectral resolution and radiometric resolution (modified after (NASA, 2013))

Already in the early years of satellite Remote sensing, the technology has been used in many studies to support wetland research. Several studies have previously used remote sensing and image analysis to identify and monitor salt marshes using different platforms and sensors. First, aerial photography was the primary source of synoptic information gathering when mapping coastal wetlands. Colour infrared photographs in particular were used in many studies to support the mapping and quantification of coastal wetland plant communities (Hardisky et al., 1986).

The launch of the first LANDSAT Earth observation satellite in 1972 provided highly valuable technological advancements in environmental sciences. Its multi-spectral scanner instrument helped to obtain synoptic remotely sensed data at regular time intervals to obtain useful information about objects or areas of the Earth's surface (Alföldi, 1975; Munday Jr. & Alföldi, 1979). The use of sensors to measure electromagnetic radiation beyond the visible part of the spectrum supports the acquisition of information about environmental processes and helps to increase our understanding of complex dynamics on earth and monitor natural reserves worldwide (de Jong & van der Meer, 2004). Satellite remote sensing offers the user multispectral data in a wider variety of spectral wavebands, which gave scientists access to already digitally available radiance. In 1976 and 1979, Bartlett used spectral information of plant canopies to determine correlations between green biomass, percent live biomass, total biomass, canopy height, and *Spartina alterniflora* and *Distichlis spicata – Spartina patens* mixture. He further concluded that the red and near-infrared band combination delivered the most useful results for this type of analysis. Confirmed by other studies in those early years, the most significant changes in the spectral signatures of coastal wetlands can be observed in a decrease in red and in an increase of near-infrared due to absorption by chlorophyll and

leaf scattering respectively (Hardisky et al., 1986). In another example, satellite imagery was combined with aerial imagery to classify wetlands by making use of the higher spatial and temporal resolution of the latter (Guo et al., 2017). Amani et al. (2018) published a paper on spectral separability of five different wetland classes in Newfoundland and Labrador, Canada, and proved high classification accuracies by using various spectral indices, textural, and ratio features based on optical satellite imagery. The results of this study showed as well that the near-infrared band delivers the best results, followed by the red-edge band.

Belluco et al. (2006) incorporated datasets obtained from different satellite and airborne platforms with a wide range of spatial and spectral resolutions to set a quantitative context for vegetation mapping in intertidal environments using the example of different examples of marshes in the Venice Lagoon in Italy. Their initial classification results showed that intertidal species could be discriminated most easily at their full development stage. One significant outcome of this study also proved that spatial resolution has a higher impact on classification accuracy than spectral resolution. The authors concluded that remote sensing is a useful tool for salt marsh vegetation mapping and their spatial distribution and recommend image classification to be considered as the technique of choice for salt marsh monitoring.

The use of remote sensing to monitor natural and man-induced coastal ecosystem changes are getting more reliable and gaining popularity due to advances in sensor developments and data analysis techniques (Klemas, 2011). This is mainly represented in the use of hyperspectral imagery and their benefits in species mapping in coastal salt marshes (Silvestri et al., 2002; Schmidt & Skidmore, 2003; Belluco et al., 2006).

The field of *active* remote sensing has been rising in popularity in recent times also attracted the attention of wetland researchers (Zhao et al., 2018). Scientists have published a successful study on the use of TerraSAR-X imagery, a high-resolution space-borne Synthetic Aperture Radar (SAR) platform, to map salt marsh habitats and tidal flats near the estuaries of the Hang-gang in South Korea (Yoon-Kyung et al., 2012). Van Beijma et al. (2014) applied a combination of optical remotely sensed imagery and airborne SAR imagery to map coastal salt marsh habitats on a site at the Gower Peninsula in Wales, UK. The combined application of different remotely sensed imagery is a popular approach in wetlands mapping. Jahncke et al. (2018) classified wetlands in Nova Scotia by using RADARSAT-2 Polarimetric SAR, optical satellite imagery (QuickBird), as well as LiDAR datasets. LiDAR (Light Detection and Ranging) systems provide a valuable source for generating high-resolution Digital Terrain Models (DTM) and Digital Surface Models (DSM) of intertidal landscapes. Collin and collaborators (2010) conducted an airborne LiDAR survey to detect intertidal vegetation, assess the salt-marsh zonation, and to map intertidal habitats and their adjacent coastal areas in the Gulf of St. Lawrence in Canada. High-resolution LiDAR datasets are also a useful tool to assess salt marsh restoration site suitability (Millard et al., 2013).

Mapping and monitoring wetlands with the help of remote sensing techniques generally provide high potential for evaluating the effectiveness of the restoration processes. They are a valuable tool for scientists due to the possibility of frequent site assessment capabilities and the provision of timely information from often inaccessible places. While in-situ measurements of coastal marsh environments are highly informative in regards to changes in wetland functioning, environmental drivers and their consequences for changes on the site. However, these assessments carried out by field

visitation are also very laborious and time-intensive. Although remote sensing is more cost-efficient when compared to field-based inventories, the classification of wetlands by way of remotely sensed image analysis also contains challenges due to similarities in their spectral properties (Gallant, 2015; Amani et al., 2017; Mahdavi et al., 2017). The low spectral contrast present in intertidal salt marsh components depends on various factors, such as species composition on-site (Artigas & Yang, 2006; Sadro et al., 2007), plant health (Tilley et al., 2007), and observation time (Gao & Zhang, 2006). In various studies, scientists have always tried to develop advanced methodologies and techniques to reduce the pervasive challenge of similarities within spectral characteristics between different wetland types and land cover classes (Belluco et al., 2006; Moffett & Gorelick, 2013; Amani et al., 2018). Salt marshes demonstrate a particular challenging case in wetland mapping based on remote sensing methodologies (Moffett & Gorelick, 2013).

Spectral differences in vegetation can be adequately captured by considering integration of the vegetation phenology and seasonality in the analysis (Bartlett & Klemas, 1980). This is very useful for identifying individual species for habitat mapping since the spectral signature of a plant varies throughout the season when growth impacts ratios of plant pigments, leaf water contents, plant height, canopy effects, leaf angle distribution and other structural characteristics of saltmarsh species (Ozesmi & Bauer, 2002; Gilmore et al., 2008). One way of overcoming some of the named challenges is the use of newer approaches such as the Object-based Image Analysis, which will be further discussed in a later section.

The spectral information content of RS images is influenced by several factors and processes. The position of a sensor and the orientation from which angle or direction an object of interest on the earth's surface is illuminated, control how an object is perceived

on an image. The natural light in the atmosphere is affected by diffusion, direction, reflection and absorption. It shows high variations dependent on season, time of the day, latitude, altitude, cloud coverage, and humidity. The light can be differentiated in hard quality during the clear sky and mid-day hours, and soft quality light observed under cloudy conditions earlier or later in the day. When collecting imagery for analysis, full illumination and top-lighting of landscapes are preferred during mid-day to assure the highest lighting conditions and the least possible amount of shadows on site. Vegetation has one of the most complex reflectance characteristics; one part of the sunlight may partially reflect from the top canopy and some from the surface below by penetrating the canopy through the plant to the ground. Another portion of the light is scattered in different directions by parts of the plant structure, where further scattering, transmission or absorption processes may apply (Aber et al., 2010).

1.3.1 Remotely Piloted Aircraft Systems and Sensors

The Unmanned Aerial System, short UAS, is a term involving an unmanned aircraft (UA), a ground control station (GCS), and a data link to communicate with the UA for command and control (C2) from the control station. With increasing popularity, UAS became known under a wide range of names and acronyms, such as aerial robots, drones, or in the scientific community, the more popular term of Unmanned Aerial Vehicle (UAV). Whereas, the latter term only refers to the UA itself and does not include the system with command and control. In 2011, the new name Remotely Piloted Aircraft (RPA) or Remotely-Piloted Aircraft System (RPAS) respectively was introduced by the International Civil Aviation Organization and is now the official term inaugurated in the Canadian Aviation Regulations since the last update of June 2019 (ICAO, 2011;

Colomina & Molina, 2014). This study will be referring to the terminology of RPAS and RPA respectively in the following chapters of this work.

For several decades, RPAS have been known to be successfully used in aerial photography acquisition for many different environmental applications having its roots in military activities (Klemas, 2015; Green et al., 2019). There has been a wide range of remotely controlled airborne platforms in the past with variations in size, type, and design, such as airfoils, kites, balloons, and blimps (Green et al., 2019). However, today, there are two main types of RPAs to be differentiated – the fixed-wing and rotary-wing RPA (Klemas, 2015).

Technological advancements in the flight control systems of RPAS promoted the use of these instruments as a tool for scientific research and application (Hugenholtz et al., 2012). Significant upgrades and developments of functionalities and designs of hyperspectral imagers, LiDAR sensors, synthetic aperture radar, thermal imager, and others, have further amplified their integration in scientific applications (Klemas, 2015). Another significant advantage over satellite imagery or aerial photography from piloted aircraft is the high spatial and temporal resolution of RPAS imagery, which is controlled by a ground-based operator (Pande-Chhetri et al., 2017). In recent years, the application of Remotely Piloted Aircrafts has increased rapidly through sensor capability advancements, availability of software to process RPAS imagery, hardware affordability, and improvements in sensor technology in general. Moreover, the application of RPAs is a time and cost-efficient alternative to support the multi-temporal assessment of changing environments at a very high resolution. Their practicality for repeated monitoring and surveying, in particular, has contributed to their rising popularity among scientists in coastal environment applications (Klemas, 2015; Green et al., 2019). G. F. Tomlins

(1983) had applied such platforms already in the early 1980s for wildlife habitat assessment, site mapping, shoreline mapping, and coastal studies in general (Green et al., 2019). The very high-resolution imagery (<10cm) and Digital Elevation Models (DEMs) retrieved from a RPAS surveys provide valuable sources of information for coastal management applications. Examples include, quantification of morphodynamic and sedimentary changes of the coastal fringe, monitoring cross- and long-shore sediment transport, providing input for hydrodynamic numerical modelling, and even allow the observation of coastal change and quantification of the motion of local features (Delacourt et al., 2009; Klemas, 2015).

1.3.2 Object-based Image Analysis

Object-based Image Analysis (OBIA), also referred to as Geographic Object-based Image Analysis (GEOBIA) or Object-oriented Image Analysis (OOIA), is an advanced image analysis technique providing an efficient way of data retrieval and analysis by bridging remote sensing and geoinformatics. With the ever-improving technology and demands in geoinformatics sciences, this new approach offers adequate and automated ways of handling very high spatial resolution imagery (Blaschke et al., 2014). Image analysis based on objects do not only considering spectral information, but more importantly, it allows the analyst to add spatial, textural, and topological components (Lang, 2008). This approach also shows high potential by facilitating the transformation of complex data from image scenes into ready-to-use GIS information (Lang, 2008). In particular, within the sector of natural resource management where there is a rapidly rising number of implementations of very hyper-spatial imagery captured by small RPAS (Watts et al., 2008).

Initially, digital remote sensing image classification was based on individual pixels as the basic unit for each analysis. With the application of supervised, unsupervised, or hybrid image classification techniques, each pixel is assigned to a single land use or land cover class. More traditional remote sensing sources come with coarser spatial resolutions and may contain multiple classes within a single pixel. More complex and advanced image classification techniques, such as the fuzzy classification and spectral mixture analysis, were later introduced to overcome the problem with mixed pixels. Before the end of the past century, and with the availability of very high-resolution imagery, the opposite problem was observed; higher spatial resolutions resulted in higher within-class variation captured by neighbouring images. With the new classification technique of object-based image analysis, an image object became the base of the analysis contrary to the conventional methods, where an individual pixel builds the base (Li et al., 2014). Image objects are clusters of pixels created by segmenting a whole image scene based on statistical measures of similarity (Stuckens et al., 2000). Each image object forms a new entity summarizing the information of every pixel contained in that respective object cluster and now provides spectral, topologic, and geometric information for classification (Hassan et al., 2014). Other studies have been published on successfully delineating wetlands using high-resolution satellite imagery and object-based image analysis with high accuracies (Hassan et al., 2014; Mui et al., 2015).

Object-based image analysis is relatively new within the remote sensing community of environmental applications. A workshop on Remote Sensing and GIS – new sensors, innovative methods in 2001 introduced a paradigm shift from the conventional remote sensing approach to the object-based image analysis with the synergy of computer technology, earth observation sensors, and geographical information

sciences. The number of papers applying object-based image analysis published from mainly young scientists increased rapidly in the years after – especially the publications in grey literature, though some of them were controversial regarding their scientific nature (Lang et al., 2006).

As one of the first, Burnett and Blaschke published in a journal about the OBIA application in 2003, where they argue that the conventional per-pixel classification method does not consider the spatial concepts of neighbourhood, proximity, or homogeneity sufficiently. They demonstrated an alternative image processing method to overcome the so-called pixel-centred view. Later, Benz and her collaborators published a paper in 2004, describing a detailed workflow of OBIA. In Benz's publication, they introduce, among others, the possibility of a multi-scale analysis in the *eCognition* software environment. Hierarchical networks of image objects allow image information to be represented simultaneously at different scales (Benz et al., 2004). This paper serves as an accessible guideline among researchers and is generally referred to as the 'eCognition paper' (Lang et al., 2006).

Previously conducted studies using OBIA in wetland research reported a significant increase in classification accuracy compared to conventional remote sensing methods, especially when working with very high-resolution imagery exhibiting large amounts of shadow and low spectral information as it is often observed in off-the-shelf sensors mounted on RPAs (Hodgson et al., 2003; Harken & Sugumaran, 2005; Yu et al., 2006; Laba et al., 2010; Kim et al., 2011). Pande-Chhetri et al. (2017) collected RPAS imagery at a study site in South Florida to classify wetland vegetation using both methods, pixel-based and object-based, to draw a comparison between both approaches and concluded that OBIA outperformed the conventional analysis method. Similar

conclusions resulted in a study conducted on a site at the Yangtze River Estuary in China, where the scientists evaluated the classification performances of pixel-based and object-based analysis to map salt marsh species using very high-resolution satellite imagery (Ouyang et al., 2011).

Rokitnicki-Wojcik et al. (2011) showed that OBIA rule sets based on high-resolution satellite imagery can successfully be transferred to other regions with similar spectral, spatial, and textural properties to classify coastal high marsh in Georgian Bay, Canada, and demonstrated with that the opportunity for standardization in wetland mapping using OBIA.

After reviewing available literature and publications related to mapping salt marshes using OBIA, there has been a noticeable trend of fairly inconsistent choices of spectral and spatial resolutions, parameter settings, or even classification algorithms throughout. This observation is supported by an extensive review by Moffett and Gorelick (2013), stating the difficulty of generalizing useful approaches from past wetland OBIA studies from the literature. This stresses the importance of creating an OBIA framework to classify intertidal wetlands that employ RPAS imagery, which will provide a monitoring base to improve mapping quality for restoration trajectories.

This thesis research focuses on the development of a systematized classification framework for tidal wetland restoration projects based on multispectral RPAS imagery using the methodology of object-based image analysis. With OBIA, ecologically meaningful information on spatial context and neighbourhood relationships can be taken into consideration when it comes to the identification of heterogeneous landscapes (Dronova, 2015).

1.4 Research Question and Objectives

The process of image interpretation and classification of remotely sensed imagery with high temporal frequencies allows unique opportunities in deriving information from the natural environment (Li et al., 2014). The purpose of this research is to establish a classification framework for using multi-spectral RPA imagery as a tool to efficiently monitor the changing intertidal system after managed realignment. The overall goal is the development of semi-automated classification guidelines to improve the acquisition and monitoring approaches to understand primary processes and relationships between a restoration site morphology, inundation frequency, and evolution of a tidal environment.

Other studies monitoring and quantifying restoration progress in highly turbid and macro-tidal systems with high suspended sediment concentrations, such as it is present in the Upper Bay of Fundy, are limited. In particular, monitoring at a high spatial and temporal resolution in a semi-automatic way has not been applied before in these environments. Conventional methods of coastal marsh restoration monitoring in Nova Scotia are constrained to yearly field deployments, focusing on a range of physical and biological components, such as hydrology, soils and sediments, vegetation, nekton and benthic invertebrates (Bowron et al., 2013); which, while successful, do not provide a basis to understand why or how these changes may have taken place. The outcome of this research builds upon the work processes of CBWES Inc. and offers a more cost and time-efficient alternative by automating the creation of habitat maps, extracting geospatial attributes using image analysis and understanding factors driving restoration trajectories.

This research uses the managed realignment project of the *Making Room for Wetlands Project* in Converse, Nova Scotia, as a case study to illustrate the use of Remotely Piloted Aircraft Systems and OBIA as an alternative method of data acquisition

and image analysis to improve our understanding of a tidal wetland restoration trajectory. The integration of machine learning algorithms will further help to improve image classification results and support the automation of the classification process.

The overall goal is the development of semi-automated classification guidelines to improve the acquisition and monitoring approaches to understand primary processes and relationships between a restoration site morphology, inundation frequency, and evolution of a tidal environment. The individual objectives for this study are:

1. Increase accuracies by establishing a semi-automated classification framework using multispectral RPAS imagery and Object-based Image Analysis.
2. Improve classification outcomes by implementing machine learning algorithms into the analysis of hyperspatial imagery.
3. Identify restoration progress by quantifying land-cover classes of multitemporal imagery.

The outcomes can be used as general guidelines by scientists and analysts on how to use multispectral RPAS imagery to identify dominant drivers of a restoring system and understand the process of a changing landscape in a macro-tidal marsh environment by applying object-based image analysis and machine learning algorithms.

Wetland researchers and conservation managers can refer to the results and conclusions to support coastal salt marsh restoration assessment and monitoring. The outcomes of this work are designed to be incorporated in monitoring protocols of intertidal wetland restoration activities using hyperspatial RPAS imagery and Object-based Image Analysis.

Chapter 2: Study Site

This study was conducted within the Converse Marsh restoration site in the upper Bay of Fundy in Nova Scotia, Canada. The site belongs to the larger Tantramar Marsh system and is located at the head of the Cumberland Basin, the north-east extension of Chignecto Bay. The record-breaking tides in the upper Bay of Fundy are caused by the unique confluence of local geology, seabed morphology, geography, and oceanographic factors (Desplanque & Mossman, 2004). The tidal range in this region is at times greater than 16 metres and falls under the classification of a hyper-tidal environment (Tibbetts & van Proosdij, 2013). The Higher High Water Large Tide (HHWLT) in the area of the Cumberland Basin is predicted to be 6.10 metres (CGVD13 vertical datum), or 13.4 metres (Chart Datum) predicted from the station at Joggins #215 (Webster et al., 2011). In Atlantic Canada, there are usually two unequal high waters and two unequal low waters during one day, which is known as semidiurnal tides (Desplanque & Mossman, 2004).

Suspended sediments in the tidal waters are locally still very abundant due to the dominance of Carboniferous, Permian, and Triassic sandstones and siltstones forming the relatively weak bedrock of the Cumberland Basin. The eroded material from the seabed help to build the salt marshes and mudflats in the region by providing extensive deposits of fine sediments (Simmons et al., 1984; Ollerhead et al., 2005). As a reference, it is estimated that historically about 25 metres of sediment was deposited over a period of 3,000 to 5,000 years in the Aulac marsh in close proximity to Converse on the New Brunswick (NB) side of the Missaguash River (Simmons et al., 1984).

2.1 Physical Description and Characterization

Converse Marsh belongs to the broader Tantramar Marsh System and is situated along the eastern shore of the Missaguash River, which forms the natural border between the two Atlantic Canada provinces New Brunswick and Nova Scotia (Figure 2.1). In the upper Bay of Fundy, suspended sediment concentrations vary seasonally due to higher wave energies and turbulences during the winter season, leading to greater rates of sediment resuspension (Poirier et al., 2017). In general, sediment deposition depends on the depth of the water covering the marsh surfaces during high tide and the velocities with which the water leaves again on the falling tide, which controls varying amounts of fine silts and clays resuspension.

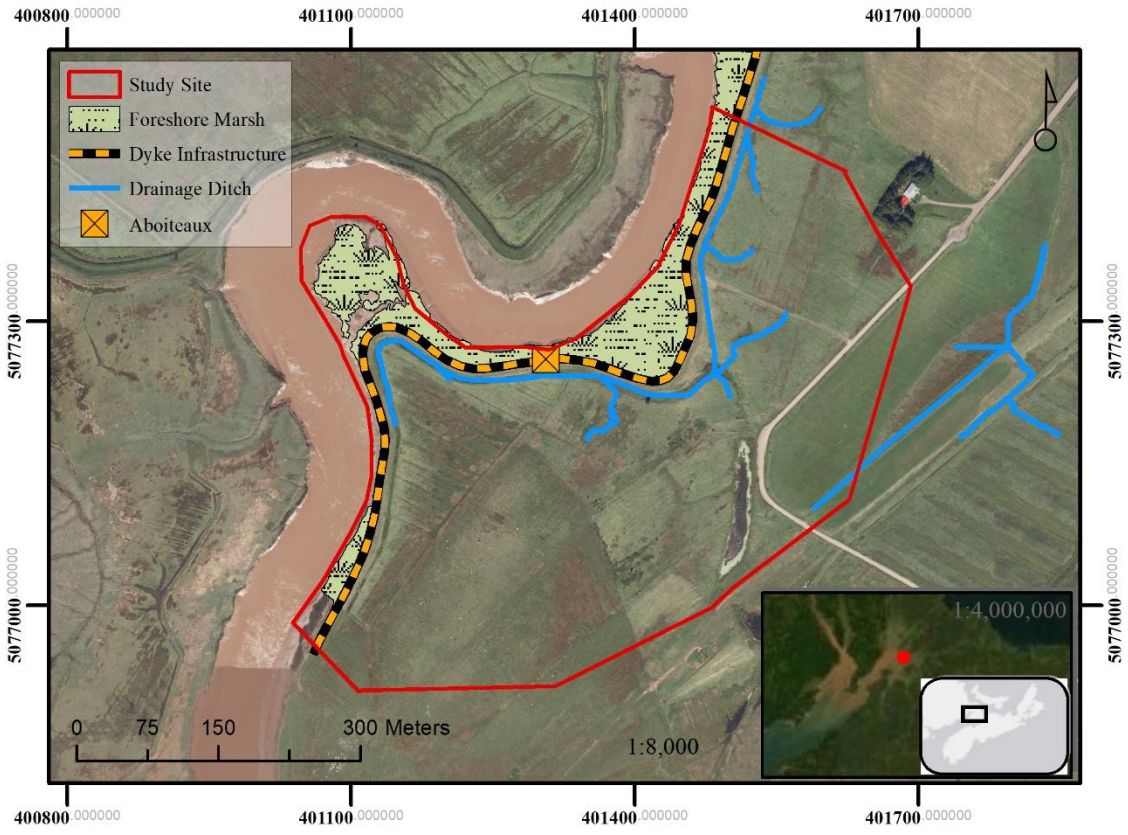

Figure 2.1: Overview of Converse Marsh restoration site prior to restoration. Background image is the Nova Scotia Provincial Orthomosaic of 2012 (Source: DDST, 2020).

The most common plant species in the brackish and salt marsh found in this area are *Spartina alterniflora*, *Spartina patens*, *Spartina pectinata*, rushes, sedges, and other halophytes such as *Suaeda*, *Salicornia*, and *Plantago* (Simmons et al., 1984). The vegetation at the site to be restored was dominated by old-field graminoids and forb species across the fallow agricultural land, whereas the primary drainage ditches were overgrown freshwater plants such as *Typa latifolia*, *Scirpus cyperinius* and *Alopecurus geniculatus* (Bowron et al., 2019). The average daily temperature ranges from -7.7 ℃ in January up to 18.5 ℃ in July, with the lowest averaged amounts of precipitation occurring in August and the highest in November ranging from 74.4 mm to 110.8 mm (Figure 2.2) (Environment and Natural Resources Canada, 2019).

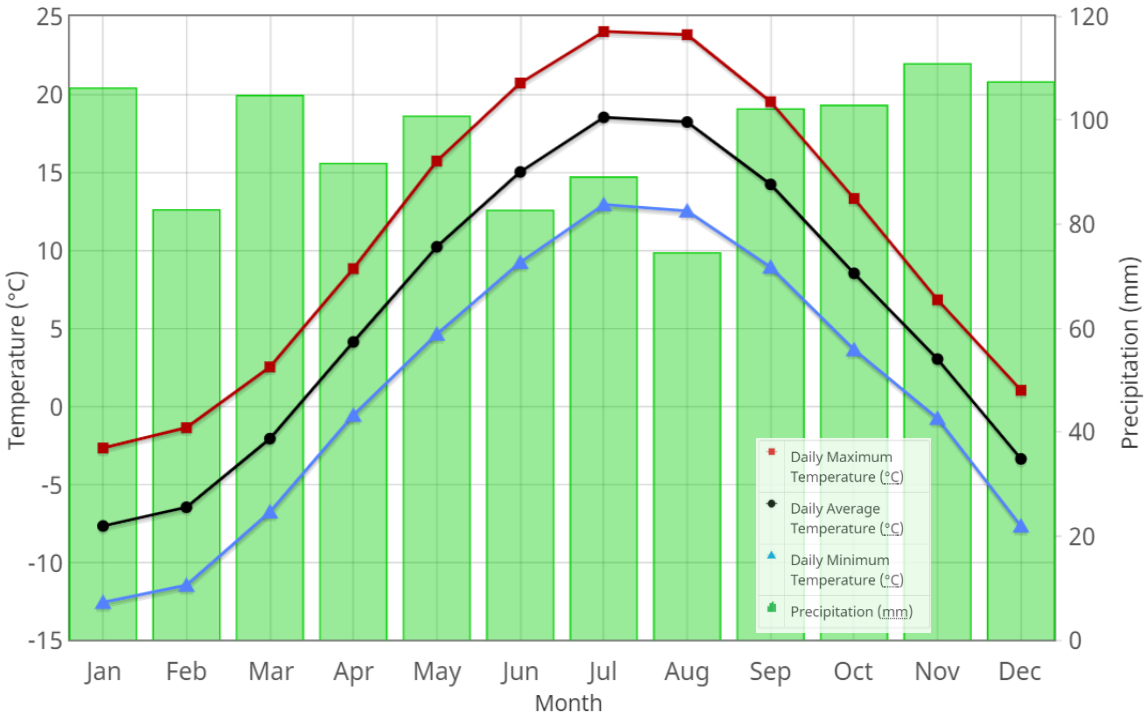

Figure 2.2: Temperature and precipitation graph for 1981 to 2010 Canadian Climate Normals – Station: Nappan CDA (Environment and Natural Resources Canada, 2019)

2.2 Dyke Managed Realignment Project

The Converse Marsh is a demonstration site for managed realignment and restoration of tidal wetland habitat within the *Making Room for Wetlands* project. While the primary goal is to restore habitat, the project also seeks to identify issues, challenges, and considerations beyond the ecological and engineering aspects of managed realignment to help inform future tidal wetland restoration projects involving dyke systems in this region (Bowron et al., 2019). This site was first identified following the outcomes of the AgriRisk project (van Proosdij et al., 2018; https://nsfa-fane.ca/projects/agririsk/). This project builds a vital foundation to inform and assist decision-makers in the process of strengthening the adaptive capacity of coastal communities in Nova Scotia by assigning vulnerabilities to the dykes in the province. Vulnerability was calculated as a function of historical and contemporary rates of lateral change in foreshore marsh as well as the likelihood of dykes overtopping under a range of present and future climate scenarios. The Converse Marsh was assigned with a high vulnerability (van Proosdij et al., 2018) due to significant loss of foreshore marsh and erosion of the dyke infrastructure.

Maintaining and topping up the dyke in its current location was deemed to be unfeasible, and the risk of dyke failure was too high which would have resulted in the flooding of the protected land behind the dyke, sections of the access road to the ship railway property further south (Fort Lawrence Road), and some areas of Parks Canada property further north of the site (Figure 2.1). The Nova Scotia Department of Agriculture (NSDA) assessed the site in partnership with CB Wetlands and Environmental Specialists (CBWES) and developed a realignment and salt marsh restoration plan for sections of the land on the Converse Marsh. Later, following several months of meetings and

consultations with local stakeholders and rights-holders, and also after satisfying the regulations stated in the Nova Scotia Special Places Act, the restoration project at the Converse site was officially approved by all involved parties and selected as the test site in the frame of this research (Bowron et al., 2019).

CBWES Inc. and engineers within Nova Scotia Department of Agriculture, Land Protection Section, in consultation with other experts at Saint Mary's University, designed a realignment plan that would provide effective protection of dykeland infrastructure while providing conditions that would facilitate restoration of tidal wetland vegetation. Figure 2.3 shows the construction details of the project proposal for the restoration at the Converse Marsh site.

Figure 2.3: Official managed realignment design plan drawn by engineers at the Nova Scotia Department of Agriculture (Dec. 6, 2018; Source: CBWES Inc.).
Note: Colour signatures are explained in the text.

The blue section of the dyke starting on the south-eastern end was levelled to the elevation of the foreshore fringe marsh. The breaching of the dyke was implemented by removing the aboiteau construction and widening the opening by five metres in both directions from the centre of the aboiteau on December 12, 2018. The third and last section of the former dyke was levelled to the elevation of the foreshore marsh, and the material was used to build the new dyke, running perpendicular to it. The two red polygons on the bare areas mark the borrow pit, where most of the material for the new dyke construction was obtained. The yellow section of the dyke remained unchanged, serving a protective function to divert the incoming water and potentially decrease wave activity at high tide which might erode the newly constructed dyke inland. Further changes were implemented by moving the low lying section of Fort Lawrence Road further to the upland and building at a higher elevation. Lastly, the culvert on the path connecting the old dyke with the road was removed, and the ditch parallel to the river was carved out to allow a wider channel for the incoming tides. Figures 2.4 to 2.6 outlines the development stages of the restoration activities on the site with Figure 2.4 showing the site at its original stage, Figure 2.5 the site with most of the construction finished, but previous to the breach, and Figure 2.6 the site a couple of months after the dyke has been breached (mid-December 2018) and tidal waters have been reintroduced. The imagery in Figure 2.5 and 2.6 were collected as part of this thesis research for monitoring purposes and served as the input for the pre- and post-breach classifications.

Figure 2.4: RPAS orthomosaic of Converse collected on November 17, 2017 (RPA model: DJI Phantom 3). The survey took place as part of the feasibility and design baseline ecological monitoring by CBWES Inc. (Credit: Bowron, T., CBWES Inc.)

Figure 2.5: RPAS orthomosaic of Converse collected on September 24, 2018 (RPA model: DJI Phantom 3 Professional; flight altitude: 90 m). The construction on the new dyke and the road are finished by using material from the borrow pits. The survey took place for the pre-breach classification analysis. (Credit: Akyol, R., Saint Mary's University)

Figure 2.6: RPAS orthomosaic of Converse collected on May 5, 2019 (RPA model: DJI Phantom 3 Professional; flight altitude: 90 m). The breach location (BL) is visible and the levelled sections of the dyke in the south-eastern and most northern end. Former drainage ditches (DD) were also widened, and the culvert (C) was removed. More details on restoration activities are detailed in text. The survey took place for the post-breach classification analysis. (Credit: Akyol, R., Saint Mary's University)

Chapter 3: Research Methodology

This research involves several stages that build upon each other, incorporating both field data acquisition and image processing. This work is divided into three phases. Phase I describes the steps of preparations for the fieldwork component and their realization. Phase II illustrates the specifics of the actual image analysis within the software *eCognition* (Trimble Developer, Version 9) detailing the use of selected rulesets to apply the machine learning algorithms. Phase III quantifies the classification results and interprets the results to real-world phenomena. Phase II and Phase III further reflect on the wider usage of selected methods and incorporates also literature review sections by presenting alternative methods applied in other studies to better comprehend and justify the chosen approaches. The overall workflow is represented in a flowchart in Figure 3.1.

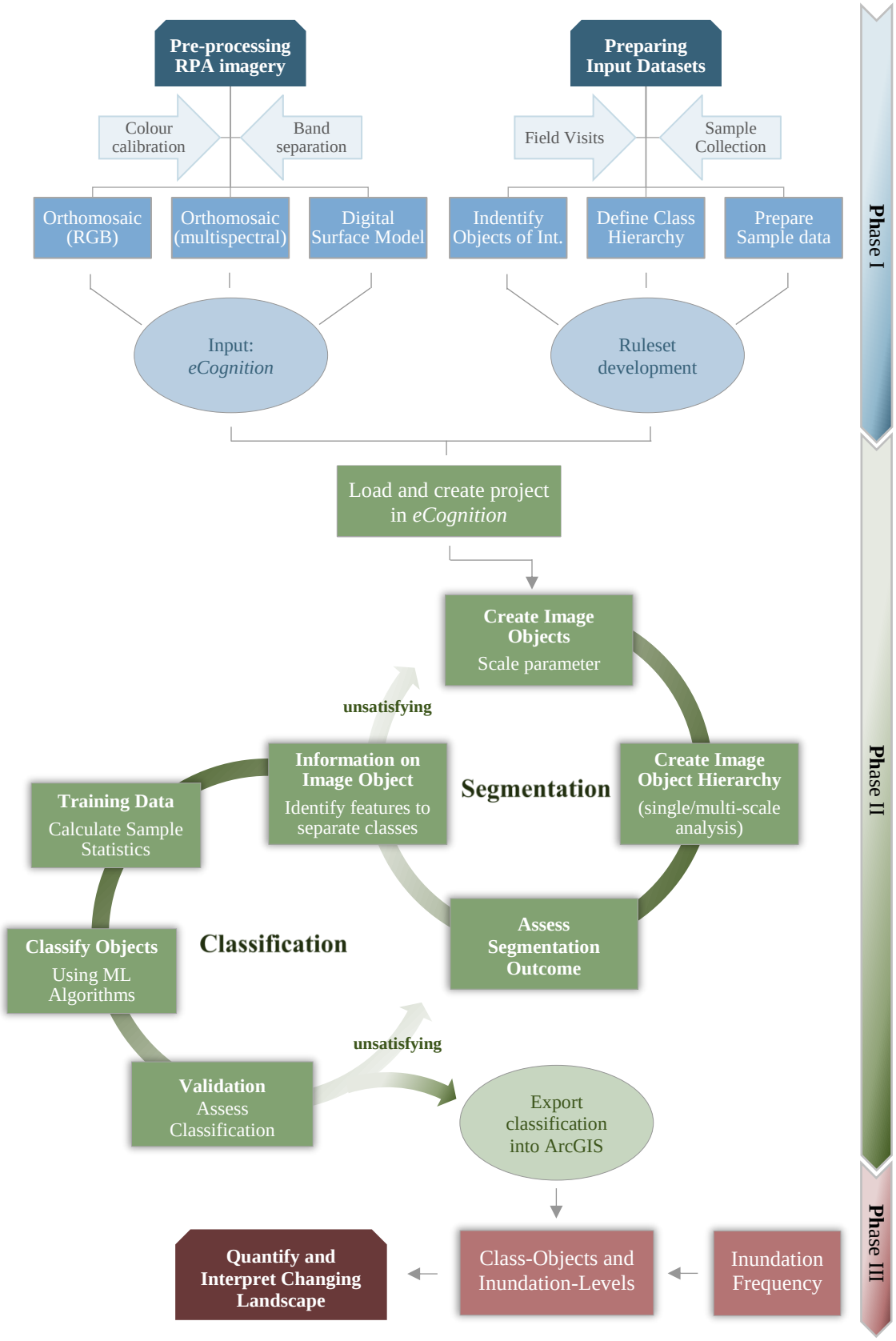

Figure 3.1: Flowchart of the three project phases with respective research workflow outlined in greater detail.

3.1 Phase I – Data Collection and Preparation

Within their regulatory constraints by Transport Canada, RPAS (Remotely-Piloted Aerial Systems) provide a cost-effective and time-efficient survey tool for mapping and measuring coastal changes. Sites that are not easily accessible are especially well fitted to be surveyed or remotely assessed and monitored by the use of RPAS. This technology also opens up opportunities for data collection on sites with very constrained time windows due to changing water levels as it is the case within intertidal wetlands.

This study deployed a small quadcopter RPA without an 'on-board' high accuracy GPS and required, therefore, a high-precision RTK-GNSS survey instrument (Leica® Viva GS14) to record accurately control monuments on the ground for proper image post-processing. The utilization of RPAS for hyperspatial image collection ensures correct geolocation and high data integrity.

Together the remotely piloted aircraft and high-precision RTK-GNSS survey unit (Leica® Viva GS14) made the data acquisition for this study feasible. However, RPAS also has to be operated legally, safely and needs to meet certain conditions and measurements for the data to be as accurate as possible. Details pertaining to fieldwork planning, preparation, and execution are presented below and outlined (Figure 3.1). Furthermore, the individual tasks executed during and after the data collection are itemized in subsequent sections.

3.1.1 Field Work Planning and Execution

This study deployed a DJI Phantom 3 Professional (quadcopter) with the complimentary RGB stock-camera (FC300X) and an additional sensor from Sentera attached on the side of the RPA (Figure 3.2). The DJI Phantom 3 Professional has a

camera lens with a horizontal Field of View (FoV) of 81° and a vertical FoV of 66° and captures images with in JPEG format measuring 4000x3000 pixels in size (DJI, n.d.). The Sentera sensor is a high precision NDVI Single sensor and captures light in the red band between 575 to 675 nm wavelength and the near-infrared (NIR) band within the 800 to 875 nm range of the spectrum. The NDVI Single sensor has a horizontal FOV of 60° and a vertical FOV of 47° with a single image counting 1248x950 pixels in size (Sentera, n.d.). In this study, the RPA flights were conducted at an altitude of 90 metres above ground level (AGL), which resulted in a spatial resolution of about 4 cm for the RGB imagery and 8 cm for the Sentera imagery.

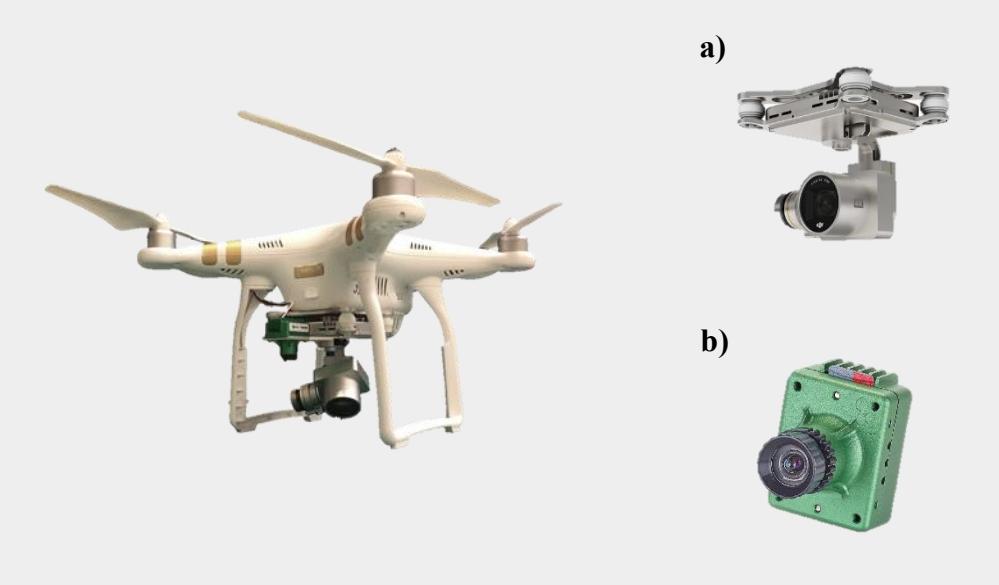

Figure 3.2: Illustration of the RPA model DJI Phantom 3 Professional with its sensor payload components, a) the RGB sensor (FC300X) and b) Sentera NDVI Single sensor in close-up view. (Source: a) store.dji.com; b) Sentera.com)

In order to obtain the necessary information for image classification, it is essential to have a good understanding of the technical specifications and the capabilities of the

equipment, legal restrictions regarding its operation in the field, as well as the environmental considerations prevalent on the restoration site.

3.1.1.1 Technical and Legal Considerations and Recommendations

The settings of the camera sensors

The Sentera NIR single sensor has a narrower field of view when compared to the FC300X camera of DJI Phantom 3 Pro leading to a smaller coverage of the ground per image. Images were acquired in blocks of multiple flight lines with enough overlap between each image to ensure full stereoscopic coverage. The desired minimum of forward-overlap is 60%, while the sidelap should not be less than 20-30% (Aber et al., 2010); however, the default settings are usually set to an overlap of 80%.

Since the Sentera sensor captures images with a smaller FoV, the speed of the RPAS was set to 3 metres per second at an altitude of 90 metres to assure gapless stereoscopic coverage of the NIR imagery. This ultimately resulted in a substantial overlap of RGB imagery captured by the DJI Phantom 3 Pro stock-camera with a larger FoV and resulted in an image forward overlap 90%.

Furthermore, the image exposure settings of the FC300X sensor needed to be considered carefully in order to prevent individual images with different exposure values. If the sky is only partially clouded and variations of the lighting conditions are expected on that day, it is recommended to set the mode to manual. The manual mode requires the user to customize the exposure value according to specific lighting occurring on a day in the field. Exposure values set too low or too high will result in overly dark or bright images and should be adjusted before each flight.

Another adjustment on the camera sensor to make before any flight is the setting on the white balance. In an automatic mode, the camera adds different colour temperatures with changing light conditions, which often occurs on days with partial cloud coverage. On one occasion, purple-white spots across the orthoimage were observed, which was likely caused by the automatic white balancing during the flight. For this reason, the white balancing was disabled during survey flights in this study.

Battery life and flight planning

Other technical considerations while planning field deployment were regarding the battery lifespan of the RPAS. The flight grids planned and executed for this study were first drawn in *ArcGIS Desktop* (ESRI; Version 10.5). The life span of a single battery lasts about 15 minutes, covering an area of approximately 500 by 550 metres in length and width at a flight altitude of 90 metres above the ground. The battery duration applies only under favourable weather conditions. The battery capacities are highly sensitive to temperatures, close to the upper and lower limitations (0℃ - 40℃), and to strong winds (max. wind speeds limit of 35-45 km/h). The flight grids for this study were drawn in a more rectangular shape to cover a narrower path with a larger edge parallel to flight lines, by taking account not to exceed the maximum range of radio communication between the RPA and the controller. The pilot and the observer needed to be able to have visual line-of-sight (VLOS) with the RPA at all times to be able to perform the detect and avoid function with respect to other aircraft (Canadian Aviation Regulations). After the grids were drawn across the test site, ensuring an image coverage of the area of interest (AOI), the constructed grid structures were then uploaded into *Pix4Dcapture* prior to the field deployments (Figure 3.3). *Pix4Dcapture,* installed on an android tablet, was used to manage and execute every flight mission with the DJI Phantom 3 Pro. Subsequent flight

missions were executed using pre-constructed flight plans already uploaded on the application.

Figure 3.3: RPAS mission plan display, with flight grids superimposed over software basemap of the Converse study area. Display view provides information about flight altitude, ground sample distance, selected grid size with approximate flight time, relative speed and overlap settings (Source: Converse Project in Pix4Dcapture).

Legal Requirements when piloting RPAs

Transport Canada obliges every pilot of an RPAS to follow the rules outlined in the Canadian Aviation Regulations (CARs). Article 901.24 of CARs stipulates all pilots to be familiar with available information relevant to the intended flight. This includes the completion of a survey of the area, where a flight is planned to be conducted; i.e. boundaries of the study site need to be clearly defined, site suitability for take-off and landing needs to be determined, understanding of the airspace. The proximity to

aerodromes is another crucial point. The Converse restoration site lies just at the edge of a radius of 1 nautical mile (1.9 km) horizontal distance to a heliport in the town of Amherst, Nova Scotia.

When the flights were conducted in September 2018, and later in May 2019, the regulations of Transport Canada enacted pilots of small RPAS to contact the heliport operators and inform them about their intentions prior to a flight mission. The new regulations, effective since June 1st of 2019, stipulate advanced flight certification or Special Flight Operation Certificates (SFOCs). These and further information can be obtained by consulting the Canada Flight Supplement (for aerodrome directories, information for flight planning) and the Designated Airspace Handbook (DAH) published by NAV CANADA.

3.1.1.2 Environmental and Operational Considerations

Water Levels and Tides

After covering the technical and legal aspects, the site and day-specific factors needed to be determined. Predominant weather and environmental conditions can be hard limiting factors for a flight mission and its successful execution. Scheduling of was primarily based on the time of optimal tides. Therefore, the tide tables published annually by the Canadian Hydrographic Service (CHS) for the geographically closest tide station of Pecks Point (Tide Station No.190) were consulted. The indicated tide elevations and times in the respective tide tables are predicted tides based on calculations of the principal hydrographic station in Saint John, New Brunswick (Desplanque & Mossman, 2004).

At Converse, pre-restoration flights were conducted during a period of neap tides, whereas the post-restoration flights were conducted close to spring tides (Table 1.1). The

exact day for the flights was decided on the optimal times of high and low tides by considering daylight time. Additional time needed to be scheduled to place and recollect ground control targets before and after flights safely and avoid the risk of being trapped by tides. Finally, optimal conditions are given when RPAS imagery is collected during the lowest tide levels possible in order to cover as much of the intertidal landscapes morphology as possible.

In order to have a better understanding of the physical extent of the tide water levels in the field when navigating through the site, flood layers were modelled for each field trip. The flood maps were modelled based on the site elevation data, extracted from the most recent provincial LiDAR (Light Detection and Ranging) datasets, and predicted tide levels from the Canadian Hydrographic Services (CHS). Both datasets, the LiDAR images and the tide level information, were using different vertical datums and needed to be transformed first before modelling the flood extent.

Table 1.1: Times and heights for high and low tides at the closest tide station to Converse in Pecks Point (#190, CHS) predicted in Chart Datum on the left column and transformed to CGVD13 Datum on the right column using the offset value of -6.69 m based on tide level recordings (TLR).

Pre-Breach Flight:	**24/25 Sept. 2018**	
	predicted	
Time ADT	**Height** (m in Chart Datum)	**Height** (m in CGVD13)
06:29	2.4	-4.29
12:25	10.9	4.21
18:46	2.3	-4.39
00:41	11.2	4.51
Post-Breach Flight:	**05/06 May 2019**	
	predicted	
Time ADT	**Height** (m in Chart Datum)	**Height** (m in CGVD13)
07:15	1.6	-5.09
13:12	11.8	5.11
19:31	1.7	-4.99
01:28	12.2	5.51

The vertical datum of the predicted tides indicated in Table 1.1 is referenced to Chart Datum. All tidal measurements and predictions published by the Canadian Hydrographic Services (CHS) refer to the local Chart Datum (CD), which stands for the Lower Low Water Large Tide (LLWLT). This measure is an average of the lowest low waters of 19 years of predictions and describes an elevation so low, that the tide level at the respective location rarely falls below it (Desplanque & Mossman, 2004); whereas the LiDAR dataset of the province is referenced to the current Canadian Geodetic Vertical Datum – CGVD 2013. After contacting the Canadian Hydrographic Services, we obtained

the offset value of -7.35 m for the tide station Pecks Point, the geographically closest station to our test site, to transform from one datum to another.

The following (Figure 3.4 & Figure 3.5) is an example of a flood model at Converse to visualize differences in datum and to highlight the importance of other site-specific conditions, which play a role in data analysis.

A field deployment was conducted over three days at Converse, primarily to measure suspended sediment concentration, water turbidity and velocities from 21st December to the 23rd December 2018. The secondary goal was a site visitation and monitoring how the highest tides of 2018 entered the site the first time after the dyke was breached during neap tides on 12th December 2018. It was not possible to deploy the RPAS on either of the three days in the field due to low cloud base on Day 1, heavy precipitation on Day 2, and below zero degrees Celsius temperatures on Day 3. With the RTK-GNSS on site it was possible to survey the farthest extent of the high water line on Day 1 (see Figure 3.4; purple line). Figure 3.4 shows the modelled high water extent calculated for the afternoon of Dec. 21, 2018 (Day 1), as well as the surveyed high water extent (purple line).

The high water level for that afternoon was predicted to be 12.3 m (Chart Datum) by CHS. With the given offset value of -7.35 m, the high water level was calculated to be at an elevation of 4.95 m in CGVD13 (Figure 3.4).

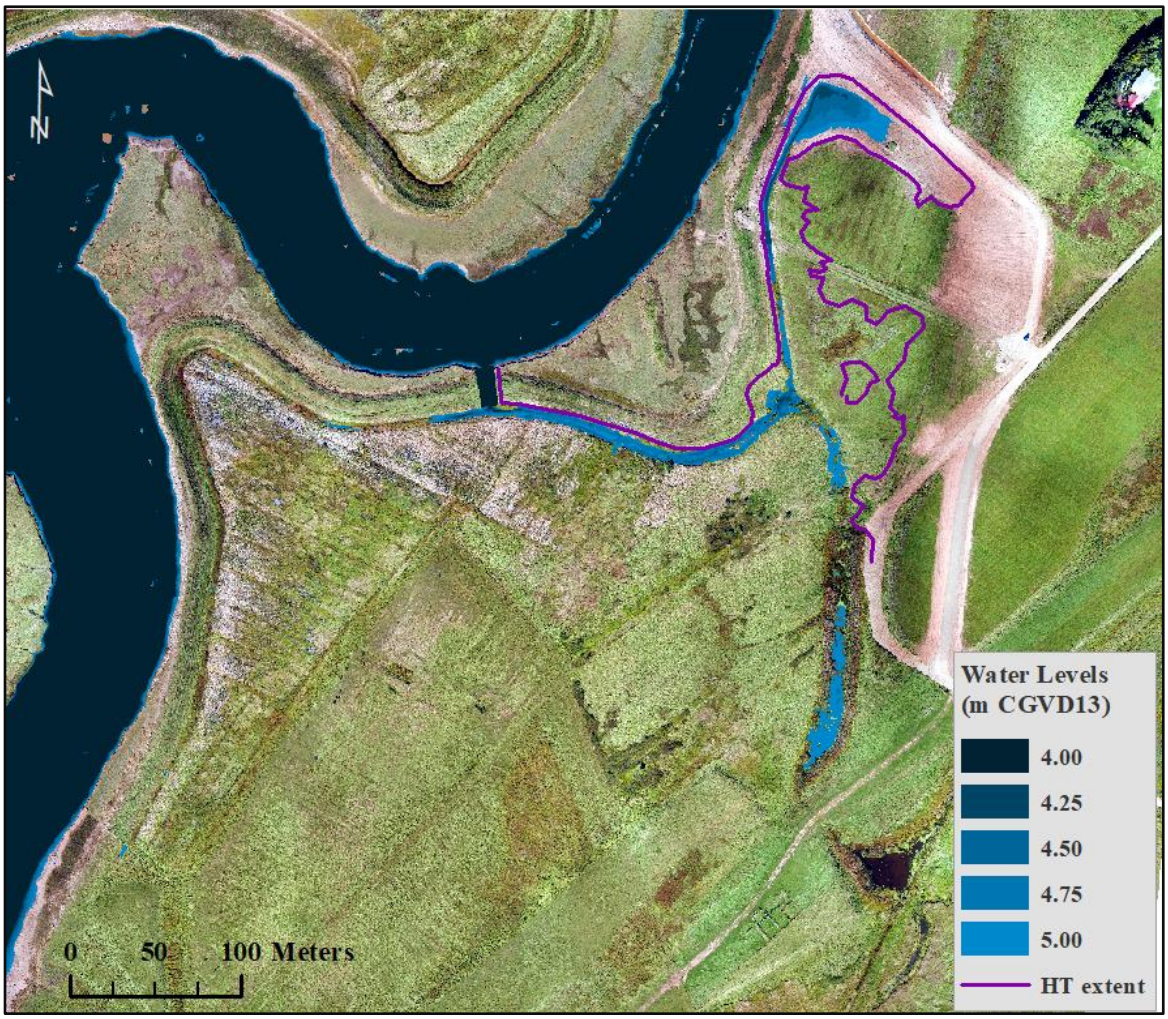

Figure 3.4: Modelled water extent based on the predicted tide of 4.95 m (12.3 m CD) for the Converse study site, using the offset value of CHS (-7.35) to convert from CD to CGVD13. The surveyed high tide extent is also indicated on the map. (Credit: Akyol, R.)

When comparing the modelled water extent and the surveyed high water line of Day 1 in Converse, it is evident that there is a high discrepancy between modelled water extent and measured water line. There can be several reasons for this observation:

a) Considerable differences in spatial distance impact between station and site affecting the extent of tide levels predicted for the station at Pecks Point and the tide levels on our site at Converse; b) Inaccuracies with the CHS offset value assigned to the station; c)

Inaccuracies in LiDAR dataset; d) Site-specific characteristics affecting the expansion of tidal inundation.

In the fall of 2017, a separate deployment was conducted by CBWES Inc. at the Converse study site, where actual tide levels were recorded for the duration of 33 days (Sept. 9 – Oct. 12, 2017) with a Tide Level Recorder (TLR) installed on site. With the use of this recording, it was possible to calculate a site-specific datum offset value of -6.39 m for a transformation from Chart Datum (Station: Joggins #215) to CGVD13 at Converse. The flood extent modelling was repeated using the predicted high water level of Pecks Point, but this time, with the datum offset value of CBWES. This resulted in a corrected high water level of 5.91 m in CGVD13 for Dec. 21st, 2018 (Figure 3.5).

With the new offset value, the modelled water extent was in accordance with the surveyed high water line, which further amplifies the need for improved and permanent long-term tide level recordings.

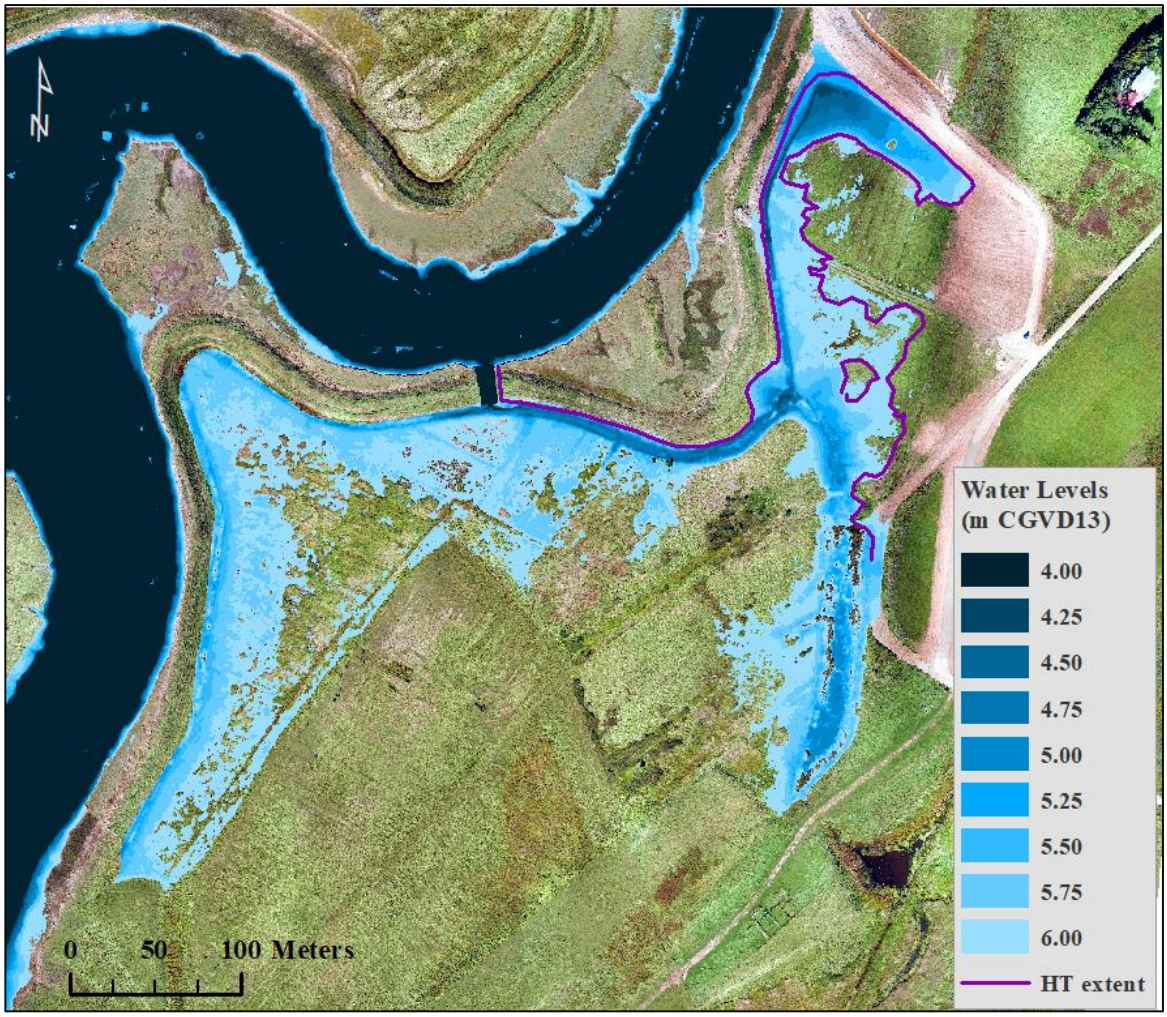

Figure 3.5: Modelled water extent based on the predicted tide of 5.91 m (12.3 m CD) for the Converse study site, using the offset value of CBWES (-6.39) to convert from CD to CGVD13. The surveyed high tide extent is also indicated on the map. (Credit: Akyol, R.)

After having clarified the tide water levels on site, the optimal days to conduct the pre-restoration flights could be identified. In the next step, the weather on a targeted day needed to fulfil mandatory criteria as detailed in the following section.

Weather Limitations

Other than temperature and wind thresholds (40-45 km/h), as mentioned earlier, gusts can be very unexpected and strong in Nova Scotia, especially at Converse, requiring RPAS pilots to be particularly cautious. Furthermore, the DJI Phantom 3 Pro cannot

tolerate any precipitation, thereby requiring immediate abortion of the flight mission under those conditions. Finally, the cloud base is another crucial factor. Weather prediction models for forecasts are usually not reliable sources to indicate the cloud base. Therefore, the next closest aerodrome was consulted to get actual information on the cloud base. The Greater Moncton Roméo LeBlanc International Airport in Moncton, New Brunswick, measures the cloud base with radar (Radio Detection and Ranging) and was contacted on field days with low lying clouds at Converse. Flight missions were not performed when the base of the clouds was lower than 500 metres above ground for flight safety reasons.

Cloud coverage, however, does not restrict the operation. It is more so relevant for the quality of the imagery for later analysis. Changing lighting conditions during RPAS surveys affects the reflectance values on the ground. Either a clear sky or complete overcast is the most preferred conditions during a flight mission. Even though the mid-day and clear sky conditions in regards to image data acquisition are the most preferred conditions due to optimal lighting conditions and minimal shadow casting, there is a problem with over-exposure on a specific spot on the ground in the imagery referred to as hot-spot in the literature. The exact position, where the hot-spot is visible on imagery, is the location on the ground directly aligned with sun and sensor with congruent angles (Figure 3.6) (Aber et al., 2010).

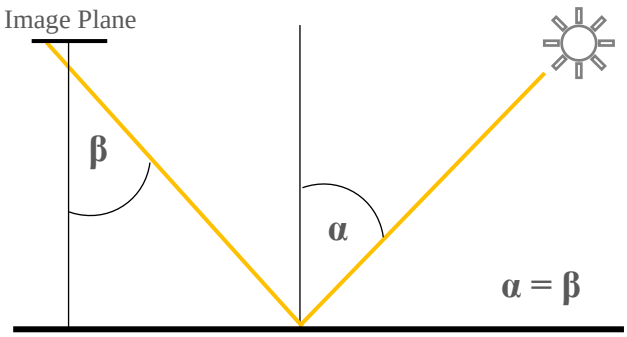

Figure 3.6: Geometric visualization to explain the presence of hot-spots in vertical images (modified after Aber et al., 2010, p.43).

The hot-spot is also known as the opposition effect and was being accounted for in this study by considering the flight date and time schedule provided by Greg Baker, the Research Instrument Technician at the Maritime Provinces Spatial Analysis Research Centre (MP_SpARC) at Saint Mary's University. This schedule highlights the hours of each day throughout the field seasons of a year in Nova Scotia using the known astronomical information of solar zenith angle at specified time and date and under consideration of the horizontal and vertical field of view angle of the camera sensor. The weather forecast was consulted and monitored carefully on a regular basis 24 hours prior to the flight.

Ground Truthing

After the flight grids were finalized, RPAS settings were modified, and the tide tables and weather forecasts consulted, the field-day with all favourable conditions overlapping was chosen. The next step was to prepare the Ground Control Points Network. A Ground Control network is necessary for georeferencing and geometrically correcting the imagery taken after a survey flight. It consists of individual Ground Control Points (GCPs) laid out in a uniform distribution across the test site. A single GCP can be

any type of target that can be easily identified in the imagery (Aber et al., 2010). For this study, a slim wooden board was chosen that measures about 40 by 40 cm in dimension and has a small hole in the center to fix the GCP target into the ground with a long nail. These boards were painted in a chessboard pattern in black and white squares (Figure 3.7). The high contrast between both colours showed an overexposure of the white parts on the board when trying to identify the center of the GCP later on the screen and did not prove as the best practice. A new design with modified colours (light-grey instead of white) and an alternative pattern (black triangular shapes on opposite edges) has proven to be more successful (Figure 3.8).

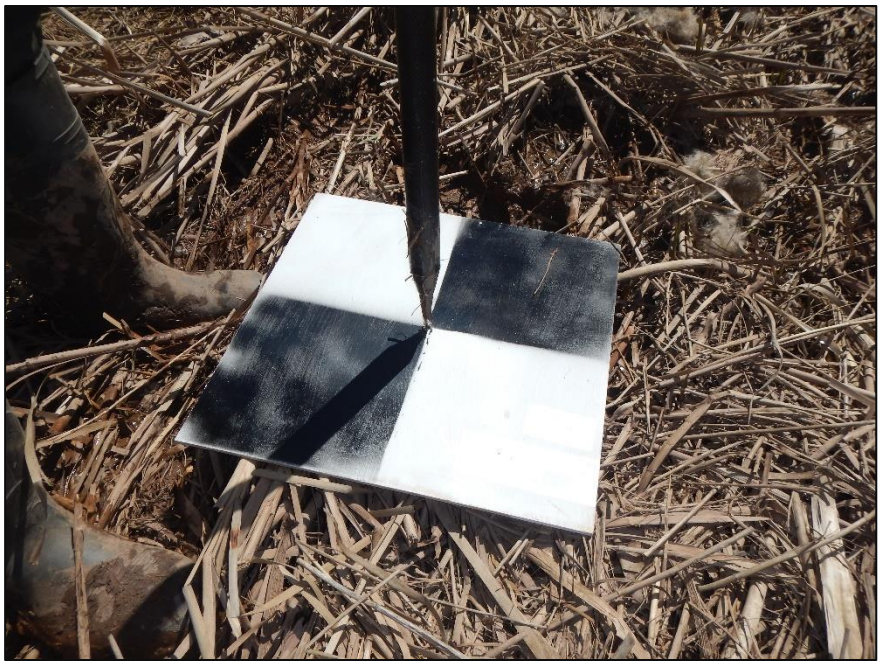

Figure 3.7: Ground Control Target in chessboard pattern measuring 40 by 40 cm (designed by CBWES) (Photo Credit: Field Team).

Figure 3.8: Recommendation for an alternative Ground Control Target design with lighter colour contrast and triangular pattern (Credit: CBWES Inc.)

Once a flight plan was created, and the RPAS mission grids were delineated, the establishment of a GCP network for the Converse restoration site could be started. In theory, an image can be georeferenced correctly with the installation of a minimum of three GCPs on the site. However, in most cases, more GCPs are necessary to account for the differences in elevation across the site and to guarantee that enough GCPs can be located on most of the overlapping images (Aber et al., 2010). Moreover, additional targets have to be installed and surveyed as Check Points (or Validation Points – VP) for accuracy assessment of the later processed orthomosaic and digital surface model.

In Converse, eight Ground Control Points and four Check Points were deployed by following the tried and tested guidelines established by MP_SpARC at Saint Mary's University (Figure 3.9). GCP target placement on the outer extent of footage may not be farther apart from one another than 1.5 times the short edge of image size, and the distance from one GCP to another in the interior of the whole imaging extent may not exceed 5 x short edge of a single image. When applying this rule of thumb, it is important to consider the changing length of the short edge by changing flight altitude. In order to

determine the number and necessary distribution of Check Points, the following rule proved itself in practice as a working measure: Number of GCPs times 0.5 and positioned in empty spots between GCPs inside the test site.

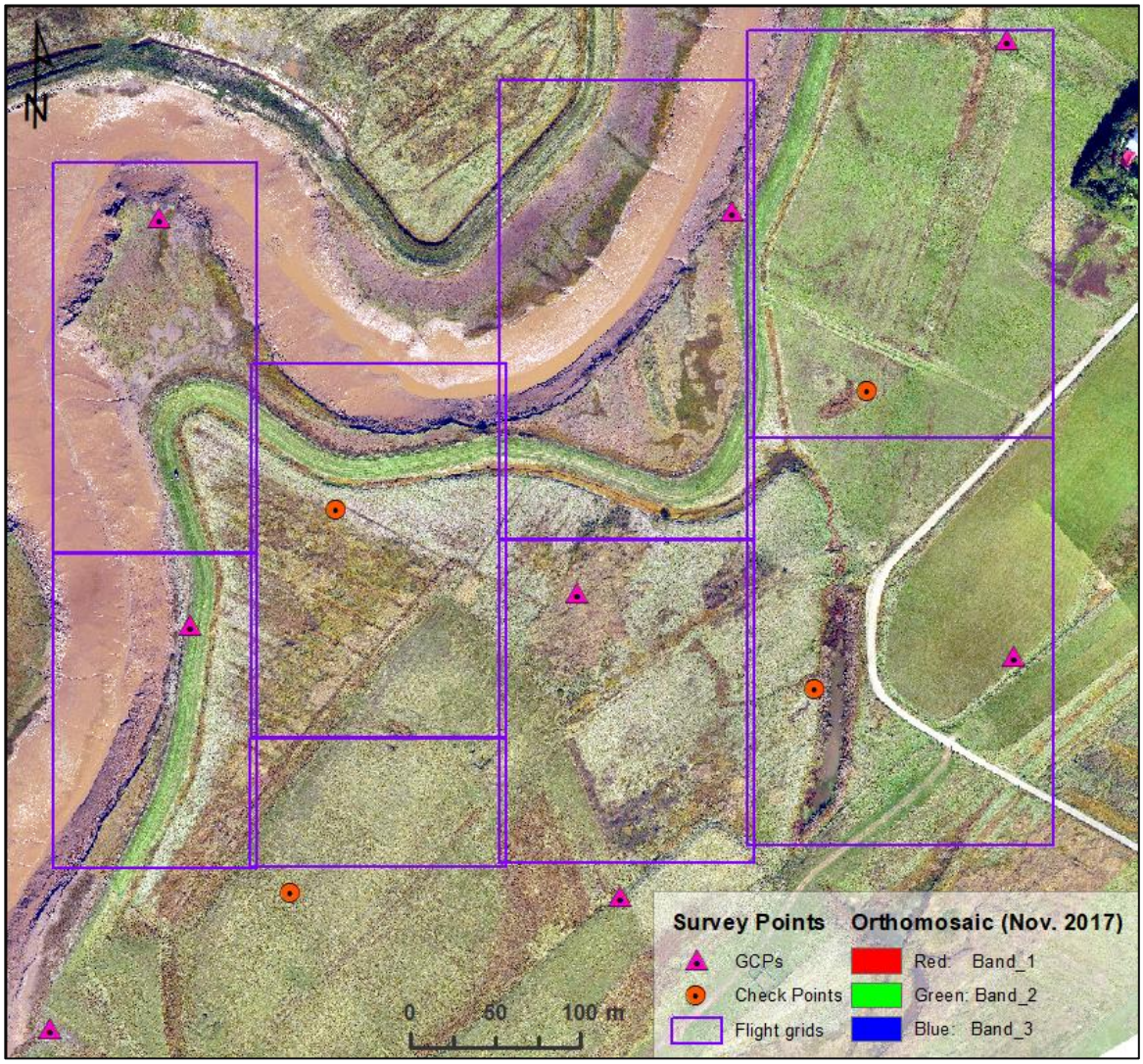

Figure 3.9: Image map of the Converse study site indicating the location of the GCP network and flight grids. Field Plan for September 24, 2018. (Source background image: RPAS orthomosaic from November 2017 by CBWES Inc.)

After placing each GCP at their planned location, the center point of each target was surveyed by positioning the RTK-GNSS instrument on top of the nail on the ground

to determine the geographic coordinates. The geometric accuracy of the images, processed after the flights, strongly depends on the accuracy and precision of the surveying technique and quality of the GCPs in the field and is very critical, especially when working with hyper-spatial imagery (Aber et al., 2010). For this reason, the use of differential GPS technology for field surveys was crucial. GNSS stands for the Global Navigation Satellite System and refers to a compilation of positioning and timing signals transmitted from a variety of satellite systems worldwide. It can provide wide-ranging coverage worldwide with the combined use of the three central systems NAVSTAR Global Positioning System (GPS) by the USA, Europe's Galileo, the Global'naya Navigatsionnaya Sputnikovaya Sistema (GLONASS) from Russia. The performance of this system can be further improved in accuracy and reliability by correcting errors from signal measurements and enhancing satellite constellation information through different augmentation systems (European Global Navigation Satellite Systems Agency, 2019).

In Differential GNSS, a network of ground-based reference stations broadcasts differential information for signal enhancement directly to the rover used in the field. The RTK technique is widely used for GNSS signal enhancement and was applied in this study. RTK uses codes for carrier measurement and data transfer corrections from so-called base stations. The communication of the rover with the known location of RTK reference base stations yielded in global positioning accuracies of a few centimetres for our data collection on-site. However, this required a base station to be not farther situated then 10 to 20 km from our rover. The problem with the relative vicinity of the rover and base station could be overcome with network RTK using a network connection for signal transmission to areas outside the reach of base stations (GMV, 2011).

3.1.1.3 Thematic Data Preparations

Preparations for Thematic Data Collection in the Field

After the general plan for field survey is completed, the second part of the data acquisition on-site needs to be established. The collection of thematic data is, in fact, the most critical step in projects building upon remotely sensed imagery as this field data would define the end-quality of the results. The image analyst has to have adequately measured information on observed features of interest. To determine which method to use or what data to collect is a challenging process. As it is prevalent in most other projects, the "validity of measurements is usually a function of the objectives of the project and the user of the end product." (McCoy, 2005, p. 59).

At the beginning of each remote sensing project and before collecting actual measurements in the field, at first, project objectives have to be clearly defined to determine the extent and level of detail which will be applicable for the field measurements, secondly, a classification scheme with anticipated land-cover class categories organized in a hierarchical structure has to be established.

Within the scope of the overall research objectives of this study, the following goals for field data collection was identified after consultation with supervisory committee members and experts of the restoration project:

- Classification of broad land-cover classes has to be identified first: vegetation, soil, rocks and water.
- Vegetation is differentiated on the general community level without detailed species composition.
- No detailed differentiation of plant communities on dominant species for the fallow agriculturally used land in the upland area.

Within the scope of this study, changes of a system in its entirety are assessed and therefore need a larger mapping scale to gain an overall understanding of the response of fallow agricultural land to the introduction of tidal flow. For the classification of a restoration site with an area of about 18 hectares, a minimum mapping unit (MMU) of 16 m^2 was defined for a map with a scale of 1:3,000. Since the classification is also based on objects and not pixels, a large survey plot was chosen to be the appropriate measure to collect the data in the field. For this purpose, a durable survey plot was designed and constructed measuring an area of approximately 4 m^2 (6 x 6 feet) split into four contiguous square parcels (Figure 3.10). The plot consists of a sturdy metal grid in the inside and is assembled with resilient PVC pipes for the framing. The end parts of the PVC pipes are held together by copper connectors. The survey plot was constructed to be robust enough for field deployment in wet and muddy terrain and also to resist transportation and usage in a salt marsh environment.

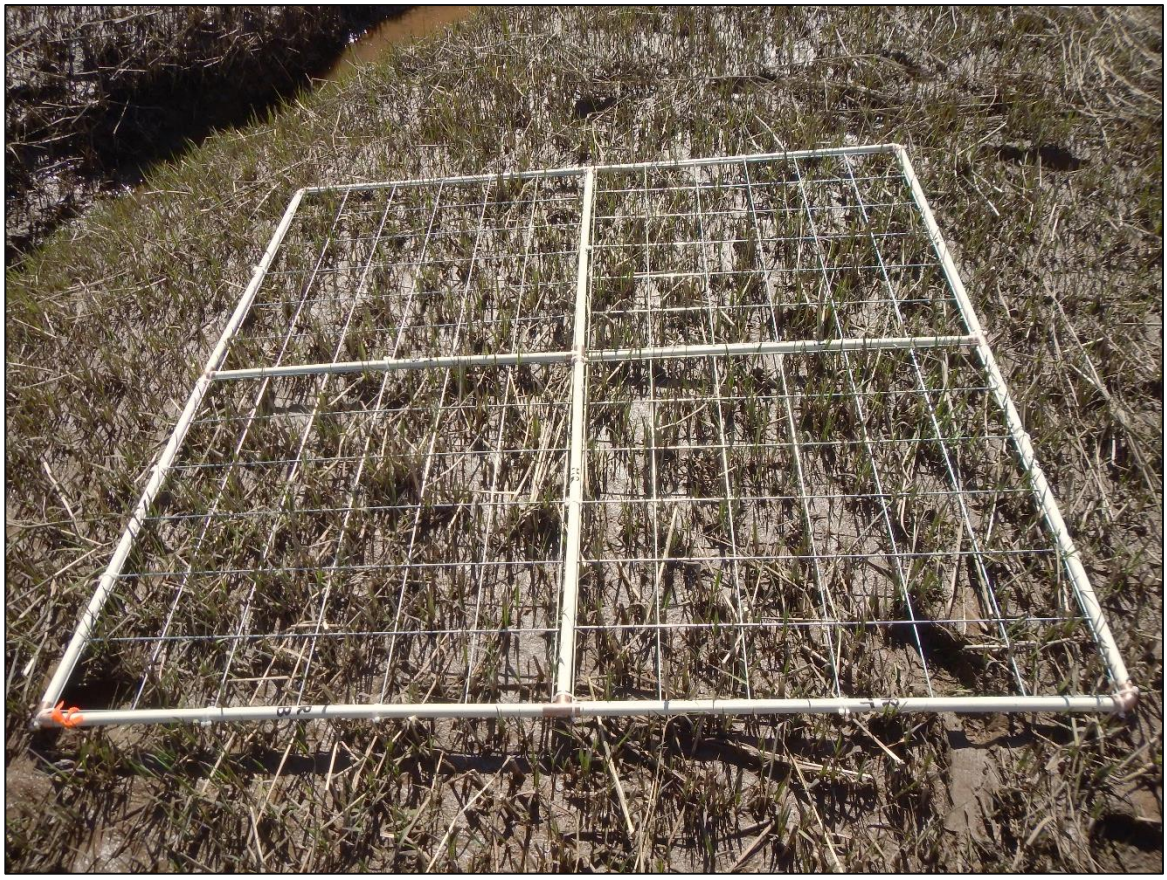

Figure 3.10: Land-cover class survey plot (4m^2) for field sampling deployed in the pre-breach survey on September 24, 2018 (Credit Photo: Akyol, R.)

The next step involved the establishment of a proper classification scheme by performing a thorough investigation and collection of ancillary data and other reference information about the site. A vegetation survey conducted at Converse in November 2017 by CBWES served as the first source of information gathering about the site (Figure 3.11).

Figure 3.11: Location map of vegetation survey transects for the Converse study site conducted in November 2017 by CBWES, indicating the differentiated vegetation communities.

Based on the information available from the vegetation survey of November 2017 and the knowledge gained by visiting established restoration sites with already matured salt marsh ecosystem during summer 2018, the following class hierarchy for the pre-breach classification was established:

Table 3.1: The Classification scheme for the pre-breach analysis of Converse (24 Sept. 2018)

Class	Sub-class 1	Sub-class 2
Bare Areas	Bare Ground	
	Borrow Pit	
	Mud	
Marsh	**High Marsh**	*Spartina patens*
		Juncus gerardii
		Spartina pectinata
	Low Marsh	*Suaeda maritima*
		Spartina alterniflora
Fallow Land	*Alopecurus pratensis*	
	Calamagrostis canadensis	
	Old Field	
	Old Field low	
	Low Health	
	Tall Species	
	Shrub	
	Pasture	Pasture Grass
		Pasture Grass (mowed)
	Ditch	*Agrostis stolonifera*
		Wet Meadow
Infrastructure	new Dyke	
	Road	
Water Body	River	
	Pond	
Rocking		
Shadow		

The pre-breach flights were conducted in late September, which is why a fair amount of shadow was expected on the imagery due to the relatively low angle of the sun at that time of the year. For that reason, a shadow class was added to the hierarchy. A vegetation glossary was created as a reference for the field plant species identification listing the most commonly occurring plants at the Converse site.

The field day for post-breach flights and surveys took place on May 5th, 2019, about five months after tidal water were re-introduced into the managed realignment site in Converse. It was the first week of spring tide after the last snow event of the year, and the temperatures were just warm enough to conduct flights. The benefit of completing flights as early in the spring season as possible is the low canopy height of vegetation, allowing the most optimal physical conditions of the site to calculate a digital elevation model using structure from motion. Details on the pre-processing of different products form the RPAS flights are discussed in Chapter 3.1.2.

Once 5th of May 2019 was identified as having favourable tide levels and weather conditions, a new classification scheme for the post-breach survey at Converse needed to be developed. Since the site was now under the influence of tidal inundation for several months, many of the land-cover classes changed. The restored area was mainly shaped by wet and muddy vegetation, a considerable amount of dead vegetative communities, ponding, and at some locations, sediment deposition. Every system behaves in a unique manner and adapts to new environmental influences at its own pace when being restored. This often leads to difficulties when a class hierarchy has to be established before the field day. After we arrived at the site and had the opportunity to assess the conditions on the ground, we were able to define the following classification scheme for the post-breach imagery:

Table 3.2: The Classification scheme for the post-breach analysis of Converse (05 May 2019)

Class	Sub-class 1
Bare Areas	Bare Ground
	Mud
	dry Mud
Marsh	High Marsh
	Low Marsh
Restoring Areas	muddy Vegetation
	tall Vegetation
	sediment Trap
	old Field (green)
	fresh Gras
	wet Vegetation
	dead Vegetation
	Shrub
Infrastructure	new Dyke
	Road
Water Body	Pond
	freshwater Pond
	River
Rocking	

Many of the different species of high and low marsh are not listed in the class hierarchy anymore. This is because most of the plants die-off during the winter under the impact of ice and snow and slowly grow after several weeks into the spring season. It is also important to note that individual species of marsh develop at different times with some of the low marsh species blooming in certain months and others shoot forth the earliest in the season. These phenological stadia need to be incorporated in future analysis when new flight plans are being scheduled to monitor restoration progress. Detecting change in vegetation on restoration sites makes sense when images are collected around the same time of the year. However, analysis to differentiate growing plants should be taken with more frequent flights throughout one season and incorporated in a single study.

Collecting Sample Data in the Field

One set of sample data is needed for the classification of the RPAS imagery to train the machine learning algorithm, and the second set of validation data to assess the accuracy of the classification results. The vegetation sampling plot described in the previous section was used to identify discrete sampling locations for the classification of the pre-breach imagery (24 September 2018). On three separate field days (4 July, 2 Aug., 15 Oct. 2018), random spots of vegetation were chosen based on the representativeness for either class. The corners of the survey plot were surveyed with differential GPS to register their exact geographic location. The observed species within the discrete borders of the survey plot were identified and recorded on a survey form (Figure 3.12, Appendix I). The information was then transferred into a GIS-compatible format (*ArcGIS Desktop* ESRI; Version 10.7.1) to train the classifier in *eCognition* (Trimble Developer; Version 9). This step is discussed further in section 3.1.3.

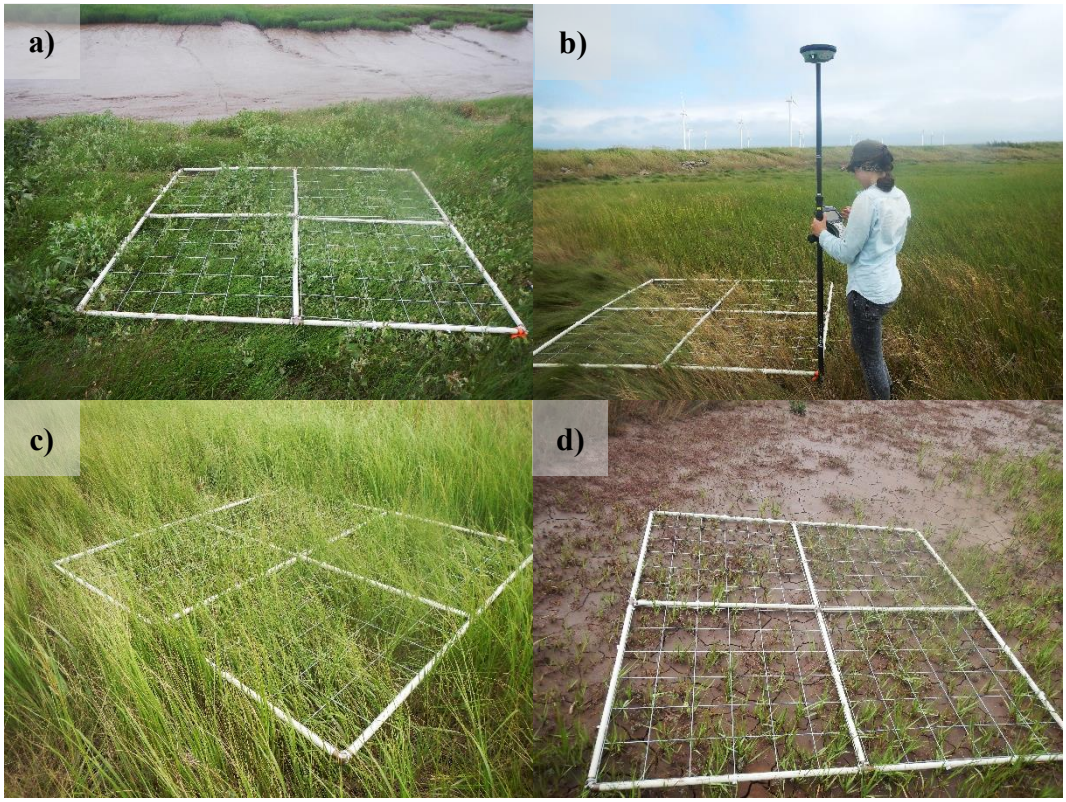

Figure 3.12: Sampling plot placed on different locations in Converse on Sept. 24, 2019, and surveyed at the corners; a) Juncus gerardii with seaside lavender and distichilis spicata, b) spartina patens, c) spartina alterniflora, d) young spartina alterniflora with suaeda maritima (Credit Photos: Sweeney, L., Akyol, R.).

Collecting samples with the vegetation plot was relatively time consuming and required extra hands in the field to carry the plot, take pictures, identify underlying features and record them in the survey form. In order to speed up the process, only two diagonal corners of the sampling plot were surveyed during the first two days in the field. This was the case in 23 out of 40 survey locations. In order to calculate the two unrecorded corner coordinates, trigonometric functions were applied (Appendix III; Credits: Graeme Matheson).

After having used sample polygons to train the classifier of the pre-breach imagery as detailed above, particular complications were identified regarding the nature of the underlying dataset and the total number of samples. Based on objects, the imagery was segmented into many image objects of different forms and sizes. Using training polygons to identify overlapping objects and assign them the respective class information led to inaccurate training of the objects. The polygonal nature of the sampling method applied does not allow the number of training samples to be controlled for each given class (Figure 3.13). Moreover, the time necessary to survey the location in the field using the plot resulted in an insufficient number of samples to train machine learning algorithms properly. Therefore, for the pre-breach classification random points were created across the image scene for training and validation purposes. Points created within the surveyed vegetation plots in the field were used for validation (160 pts.) and all other location points to train (302) the classifier (Fig. 3.14 & 3.15). For the post-breach classification, a different sampling methodology was used to collect the samples.

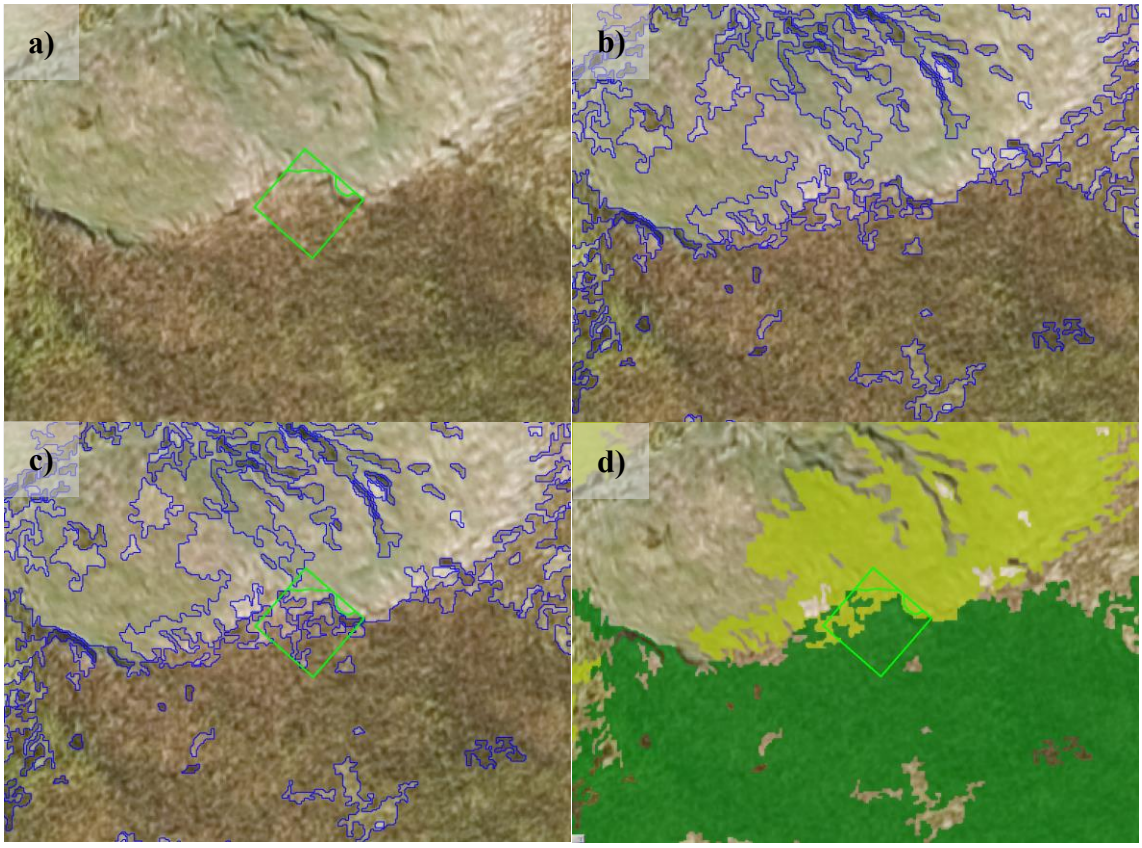

Figure 3.13: Difficulties to create correct training objects in eCognition using polygon samples to differentiate high marsh (bright green) from low marsh (dark green); a) sample polygon with divided classes, b) image objects created with segmentation, c) overlay of sample polygon and image objects, d) class assignment based on overlap between polygon and object.

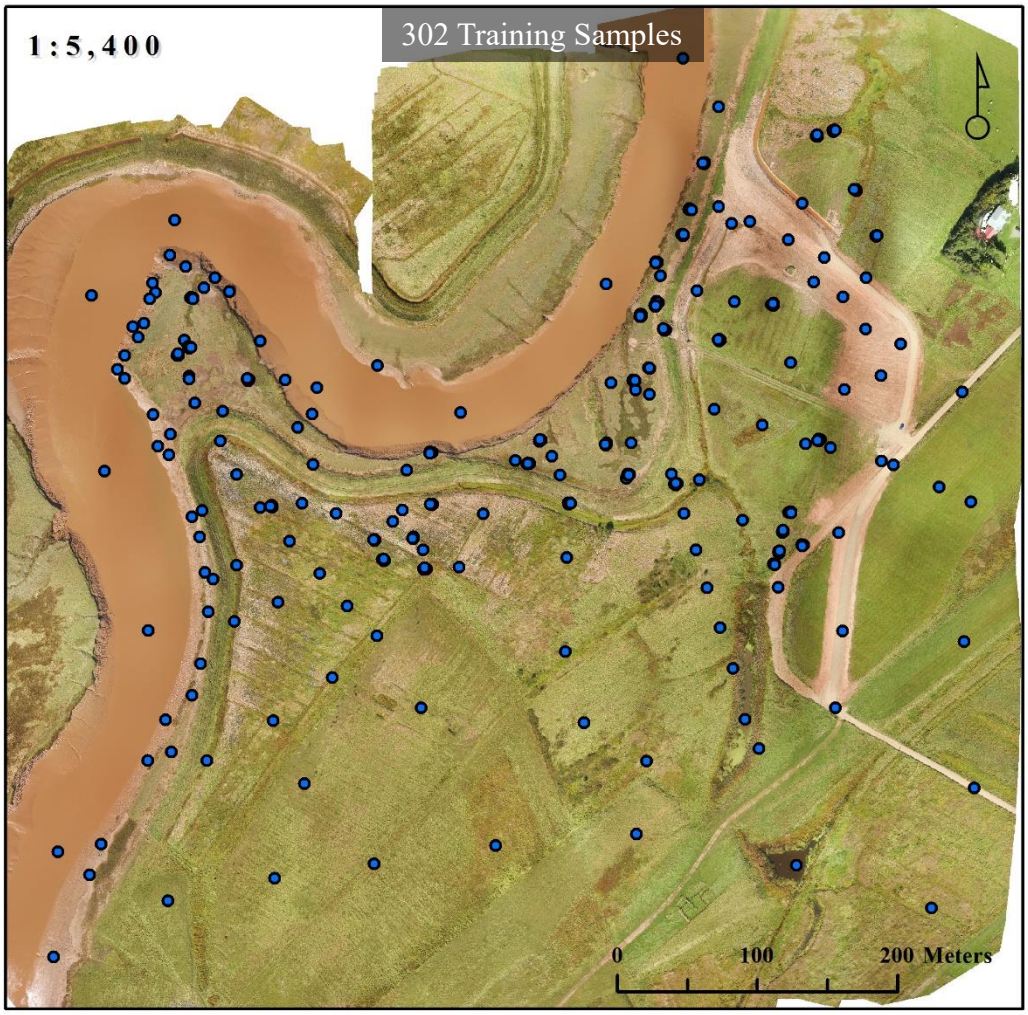

Figure 3.14: Number and distribution of training sample dataset for pre-breach classification. Sampling method: Random Points.

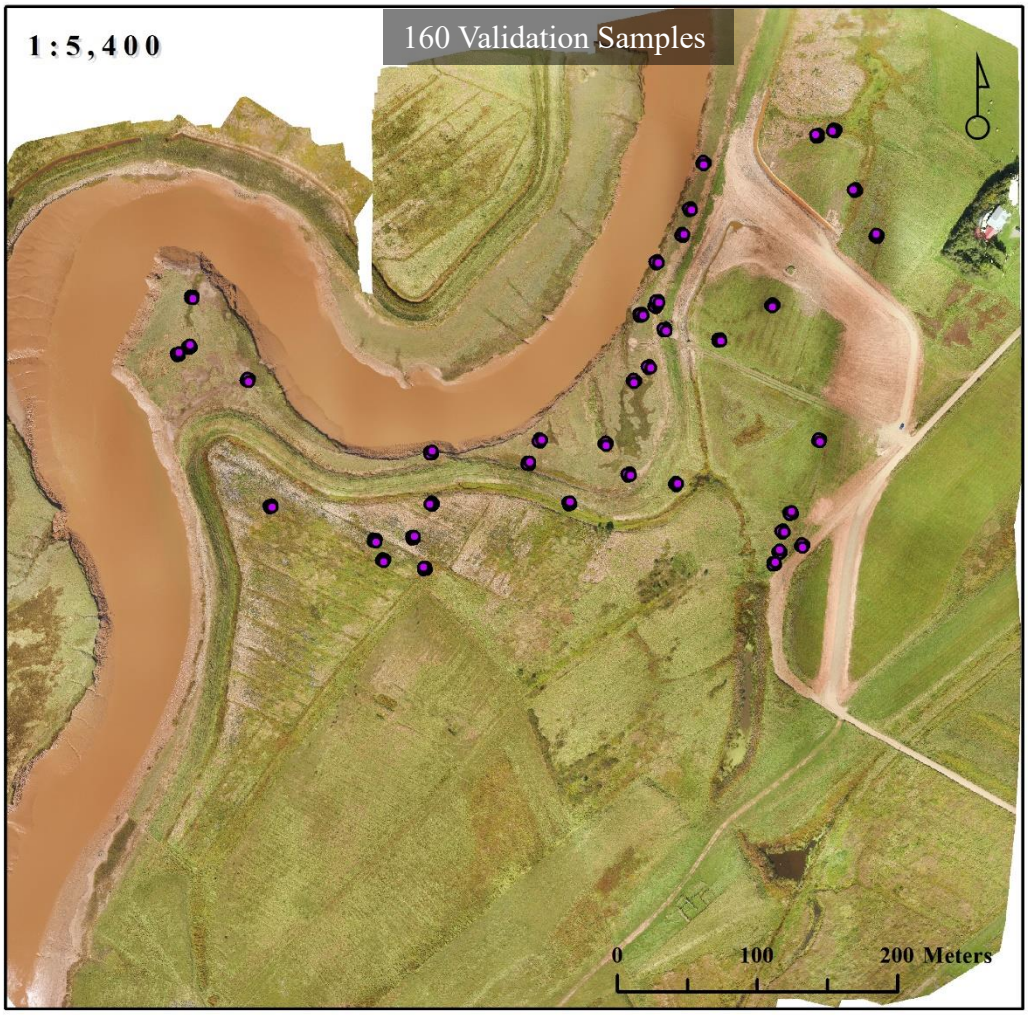

Figure 3.15: Number and distribution of validation sample dataset for pre-breach classification. Sampling method: Random Points within surveyed vegetation plots.

Due to the difficulties related to the sampling approach based on polygons (area) for the pre-breach imagery, a point-based approach was chosen for the post-breach sampling. The RTK-GNSS was used to collect point locations of significant classes in the field. The RTK from Leica has the option to create a code-list in the attributes of each job, which allowed a fast surveying method by measuring a point at any desired location and assign the respective class code to each recorded point. Each point location needed to be

chosen within a distinct patch clearly distinguishable from other land-cover classes around that particular patch to avoid mis-assignment of training data.

The sampling method for the post-breach classification was stratified random. A total of 125 sample points was collected and surveyed for the post-breach image analysis in the field on 5 May 2019 - the same day, the flights were conducted. Additional points were created digitally for training (245 pts.) and validation (120 pts.), following a stratified random sampling approach (Fig. 3.16 & 3.17).

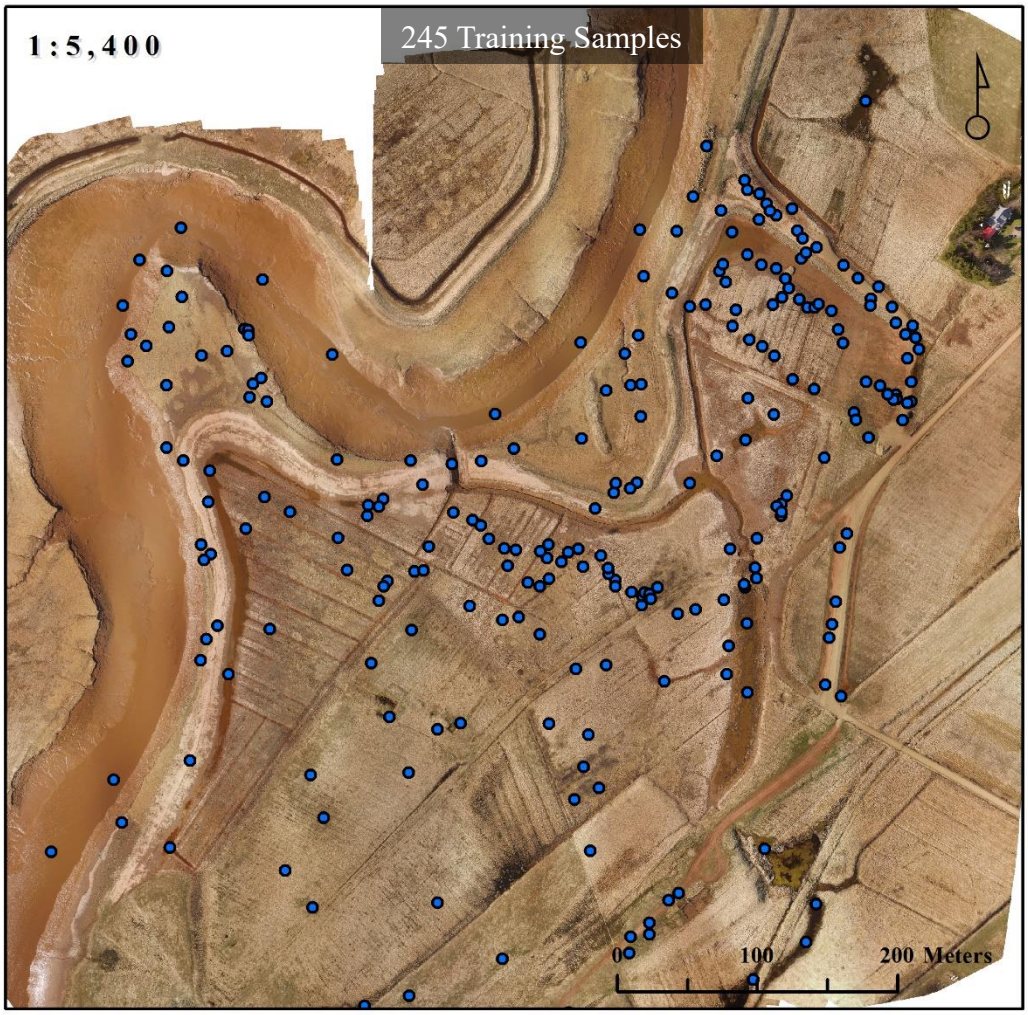

Figure 3.16: Number and distribution of training sample dataset for post-breach classification. Sampling method: Stratified Random Points from field survey complemented with digitally created points.

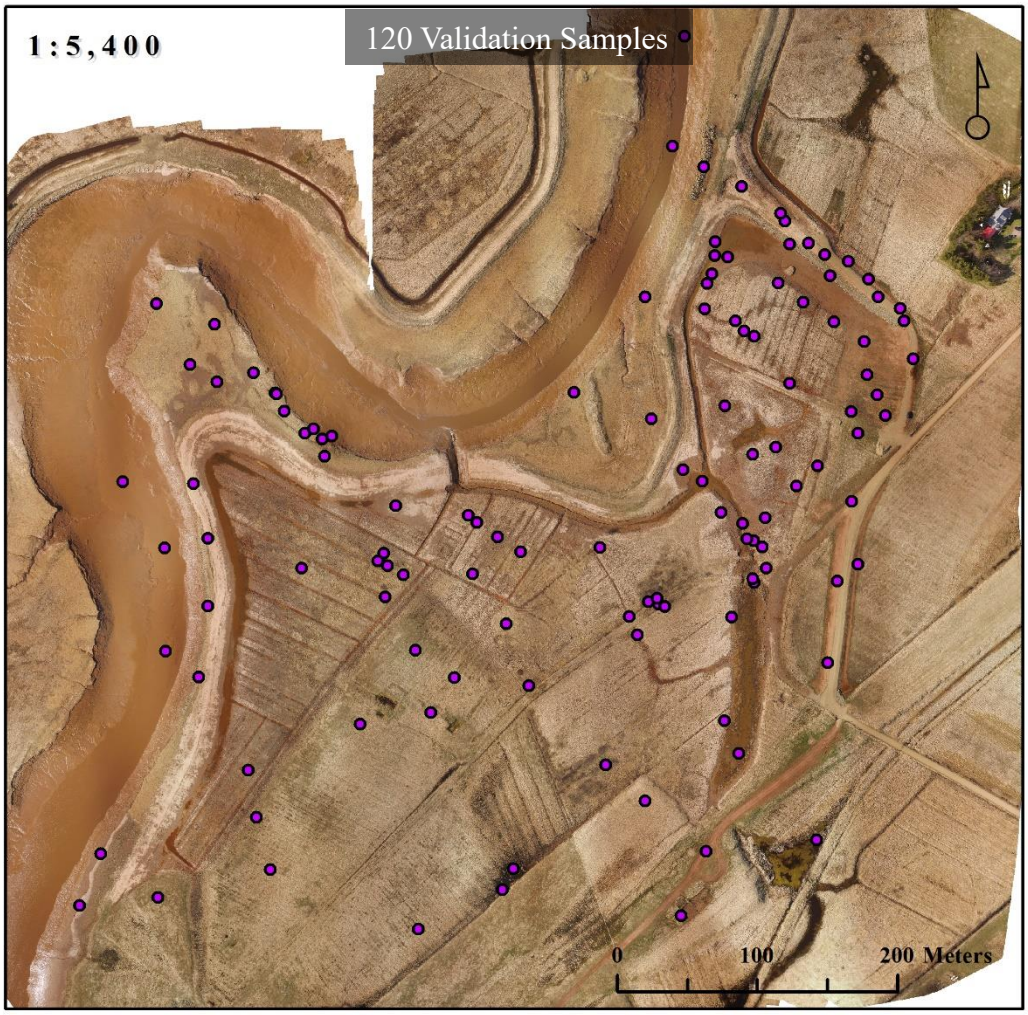

Figure 3.17: Number and distribution of validation sample dataset for post-breach classification. Sampling method: Stratified Random Points from field survey complemented with digitally created points.

3.1.2 Pre-Processing of RPAS Imagery

The RPAS imagery collected from Converse first needed to be prepared for the analysis in Phase II of the project. The photogrammetry software *Pix4Ddiscovery* (Pix4D; Version 4.2) was used to create an orthomosaic and a digital surface model (DSM) with structure from motion (SfM) for each flight mission, pre- and post-breach, as well as for both camera sensors, RGB and multispectral imagery.

3.1.2.1 Processing RGB Imagery

Pix4Ddiscovery (Pix4D; Version 4.2) is an image processing software programmed to automatically find thousands of common points between images, described as keypoints. Each group of correctly matched keypoints from at least two different images creates a point with three-dimensional information. The more significant the overlap between neighbouring images is, the more keypoints can be generated; hence, the accuracy of the orthomosaic and the DSM increases (Pix4D, 2017).

For each image, taken with the FC300X and Sentera's Single NIR camera sensor, one JPEG image file is saved with the values for each band. In addition to that, an EXIF meta data file is saved accordingly with each image containing further details such as the date and time the picture was taken, exposure time, camera name, sensor model, and GPS coordinates. Once the images were uploaded into *Pix4Ddiscovery* (Pix4D; Version 4.2) and a project was created, the first initial processing was executed with the use of the EXIF file information (Figure 3.18).

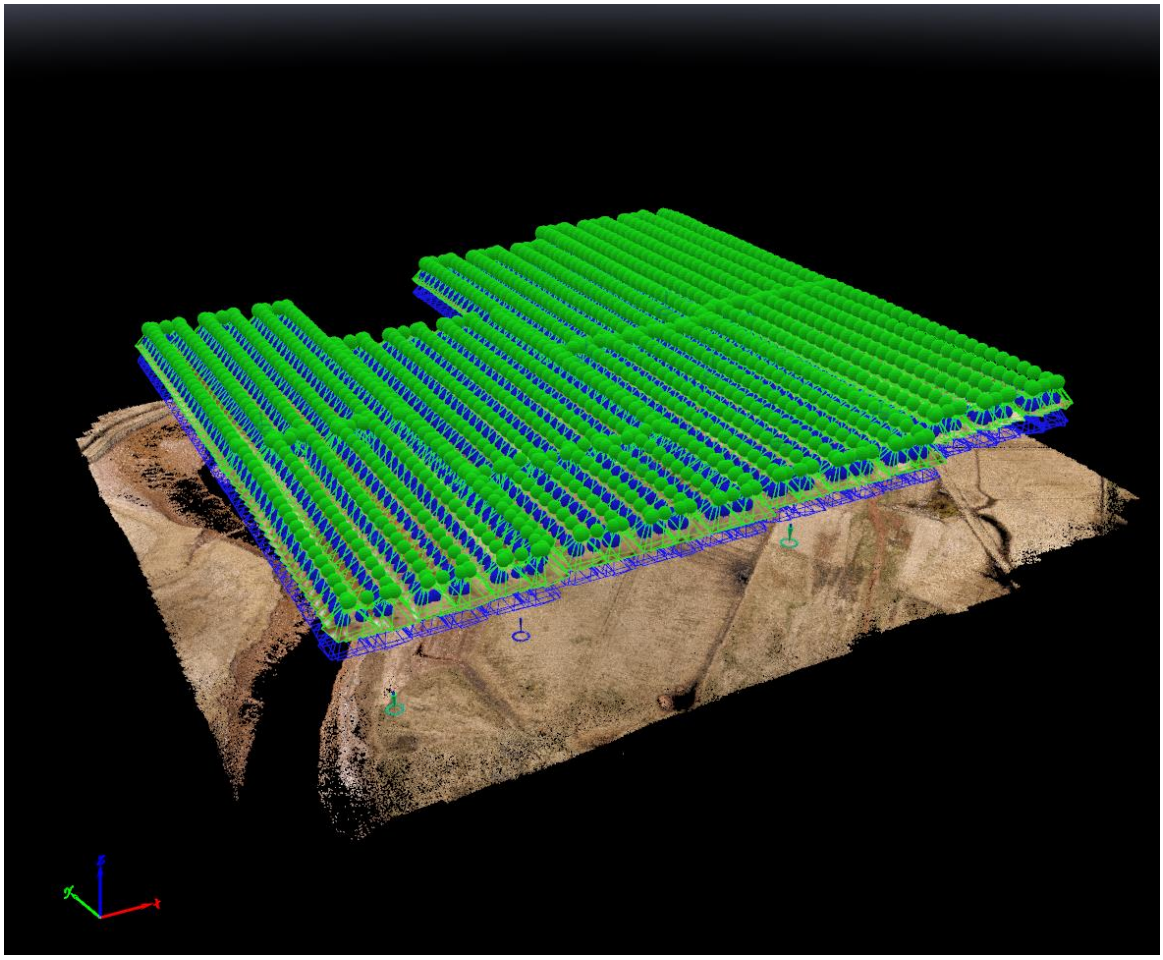

Figure 3.18: Schematic representation of individual and gridded RPA imagery for the Converse study site after initial processing in Pix4Ddiscovery. Each green point stands for one image picture taken at that location during the flight. Green lines forming squares underneath the green points show camera tilt and orientation at the moment of capture. The eight different flight grids can be visually distinguished, as well as the exact flight paths within each grid (Source: Pix4Ddiscovery).

The position of image capture with the information about camera tilting and orientation was extracted by *Pix4Ddiscovery* (Pix4D; Version 4.2) from the EXIF file. Since the GPS coordinates recorded during the flight have accuracies up to a couple of metres in horizontal and several more in vertical positioning, the reference information from the GCP network deployed and surveyed in the field was uploaded and used to improve the accuracy of the geographic location up to a couple of centimetres. Therefore,

the individual GCP targets needed to be identified in images and their known surveyed coordinates assigned to their central position within *Pix4Ddiscovery* (Pix4D; Version 4.2) (Figure 3.19).

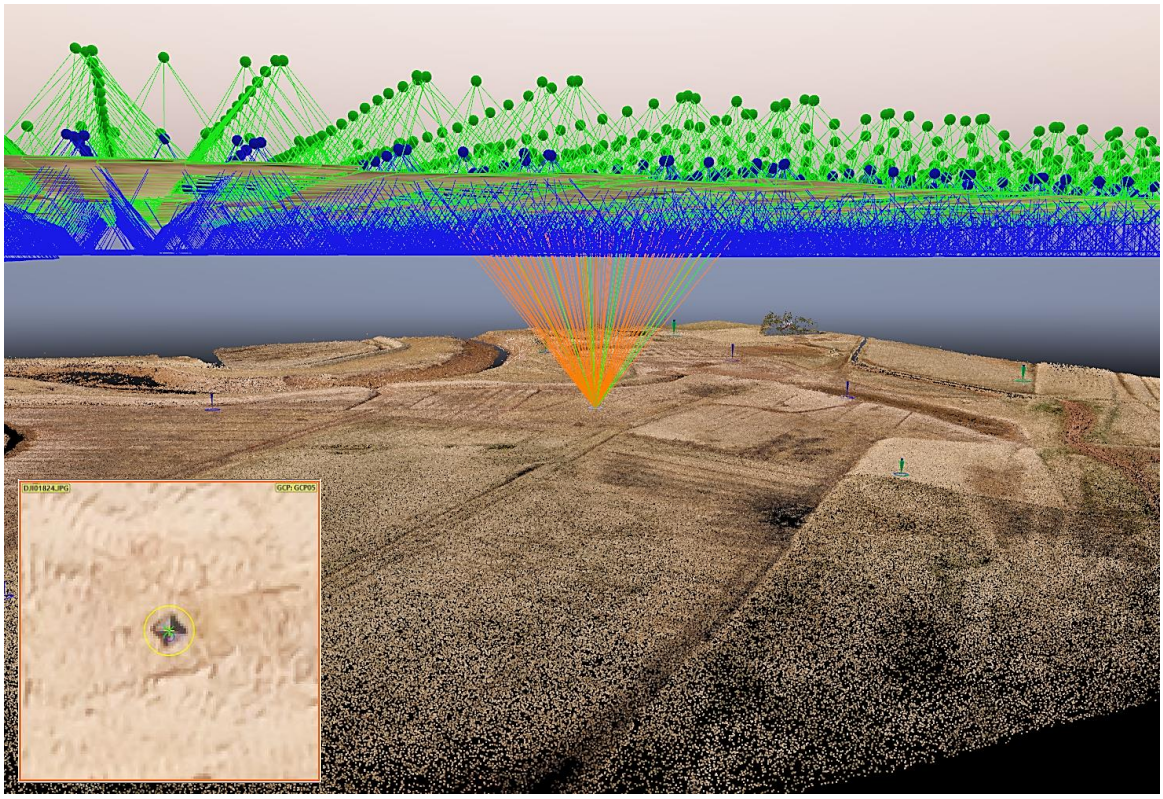

Figure 3.19: Overview of GCP location and the assignment of coordinates to captured images. Index box (bottom left) shows an example of the RayCloud view in Pix4D to check the center point of a GCP target (Source: Pix4Ddiscovery).

Once the GCP coordinates were uploaded and the targets identified on individual images, the re-optimization in *Pix4Ddiscovery* (Pix4D; Version 4.2) could be executed. Finally, the processing of Steps 2 and 3 could then be started to calculate the orthomosaic and DSM from the imagery. The resulting orthomosaic contained values of red, green, and blue in digital numbers but no reflectance values due to missing sensitivity values of the camera sensor of each band for the electromagnetic spectrum.

3.1.2.2 Processing Multispectral Imagery

The processing of the multispectral imagery revealed unexpected challenges. Before the orthomosaic with multispectral information could be processed in *Pix4Ddiscovery* (Pix4D; Version 4.2) following the steps as outlined before, the images of Sentera's camera needed to be prepared first. The Single NIR sensor has a problem with overlapping spectral responses in band 1 and band 3 (Figure 3.20).

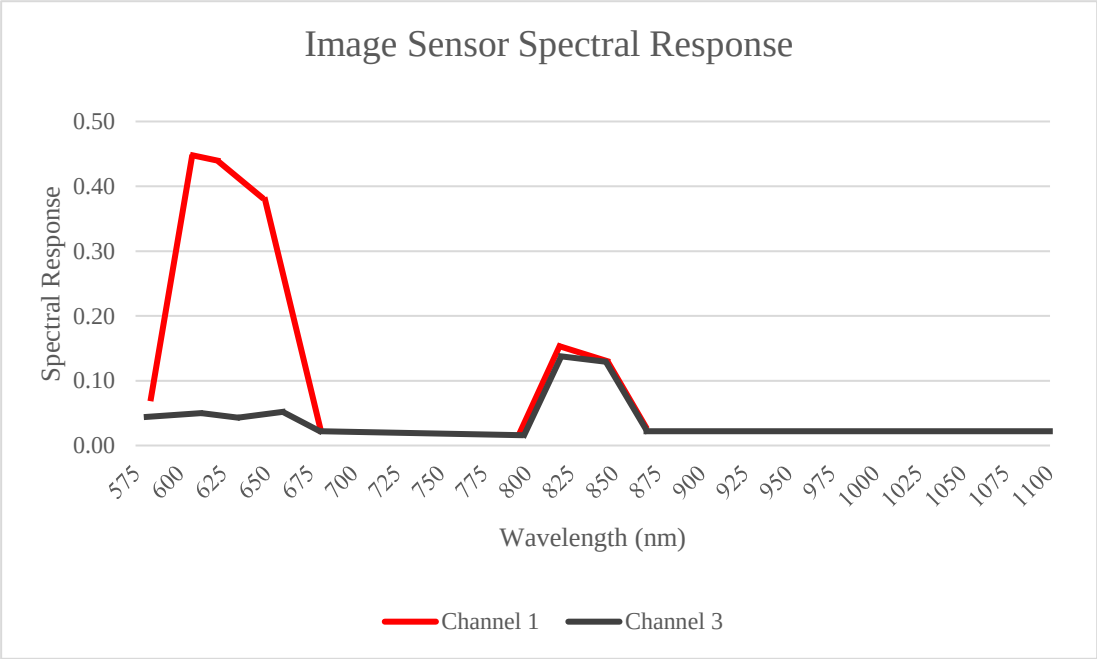

Figure 3.20: Approximate trend of the spectral response of Sentera Single NIR sensor (modified after Sentera, 2017)

Within the band 1, the portion of red light and also a portion of the near-infrared (NIR) is contained. Band 2 is indicated as unused by Sentera, even though it includes some unknown information. Band 3 of the sensor comprises the light in the NIR portion and is almost precisely aligned with band 1 in the 800 to 875 range.

In order to extract useful information on the additional information captured in the near-infrared area, the electromagnetic light recorded in both bands needed to be separated properly. The band isolation equations published by Sentera account for the difference in sensitivity for both bands (Sentera, 2017):

$$RED = 1.0 \times DN_{band1} - 1.012 \times DN_{band3}$$

$$NIR = 6.403 \times DN_{band3} - 0.412 \times DN_{band1}$$

Furthermore, there was a need to account for the unequal light irradiance coming from the sun and sky, impacting the values measured on the earth's surface for band 1 and band 3. After the published technical document by Sentera (2017), the irradiance of red light varies between 1.3 to 1.7 times the irradiance of NIR. By taking an average of 1.5, the values recorded in the NIR band could then be normalized to the power of the red light using the following equations:

$$NIR = 1.5 \times (6.403 \times DN_{band3} - 0.412 \times DN_{band1})$$

$$NIR = 9.605 \times DN_{band3} - 0.618 \times DN_{band1}$$

After having applied these equations with batch processing in *ArcGIS Desktop* (ESRI; Version 10.7.1), the imagery could not be used within the software *Pix4Ddiscovery* (Pix4D; Version 4.2) for further processing. Any calculations on RPAS images in the GIS environment lead to the loss of the EXIF file information of the imagery, which made all images useless for any further analysis.

For this reason, a customized Python script was developed to isolate the red and NIR light information by taking account of light irradiance and maintaining the EXIF file information (Appendix II). In the first version of this python script, band 1 contained the values for the red light, band 2 was left untouched, and band 3 contained the values for the NIR light only. However, this caused problems later when trying to process the orthomosaic. *Pix4Ddiscovery* (Pix4D; Version 4.2) seemed to have problems with the calculated values in the bands. After several trials of different versions of the python script, we concluded that *Pix4Ddiscovery* (Pix4D; Version 4.2) does not accept values in only two of the three bands when trying to create the orthomosaic. In the end, the final version of the script with band 1 and band 2 both containing the new corrected red values, and band 3 the corrected NIR values did allow the process to continue without any further error messages in *Pix4Ddiscovery* (Pix4D; Version 4.2).

However, the band separation led to a reduction of the image quality and a slight corruption of the actual values through the lossy compression associated with JPEG file formats (Figure 3.21).

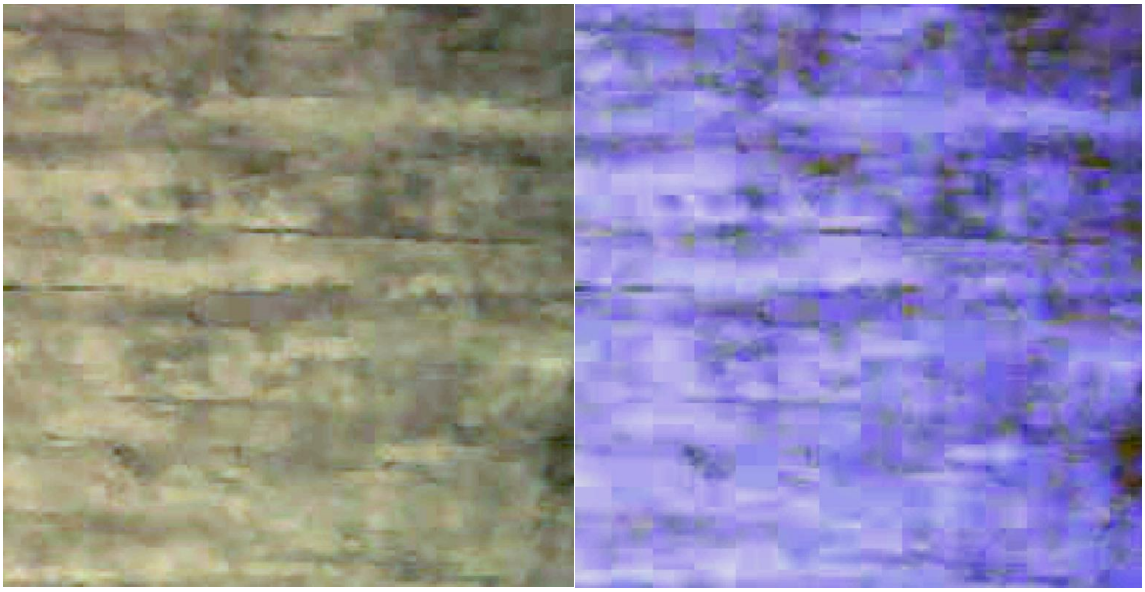

Figure 3.21: Close-up view of a single image in two different versions taken with the Sentera Single NIR sensor on 5 May 2019 in Converse. The left image is the original version with light signs of lossy compression; the right image is band separated version modified with a python script showing strong signs of lossy compression (Source: ArcGIS Desktop v. 10.7.1).

The lossy compression creating these block formations in the images and the abundance of the colour blue after the band separation has been applied made it very difficult to accurately identify GCP targets for the multispectral imagery in *Pix4Ddiscovery* (Pix4D; Version 4.2) (Figure 3.22).

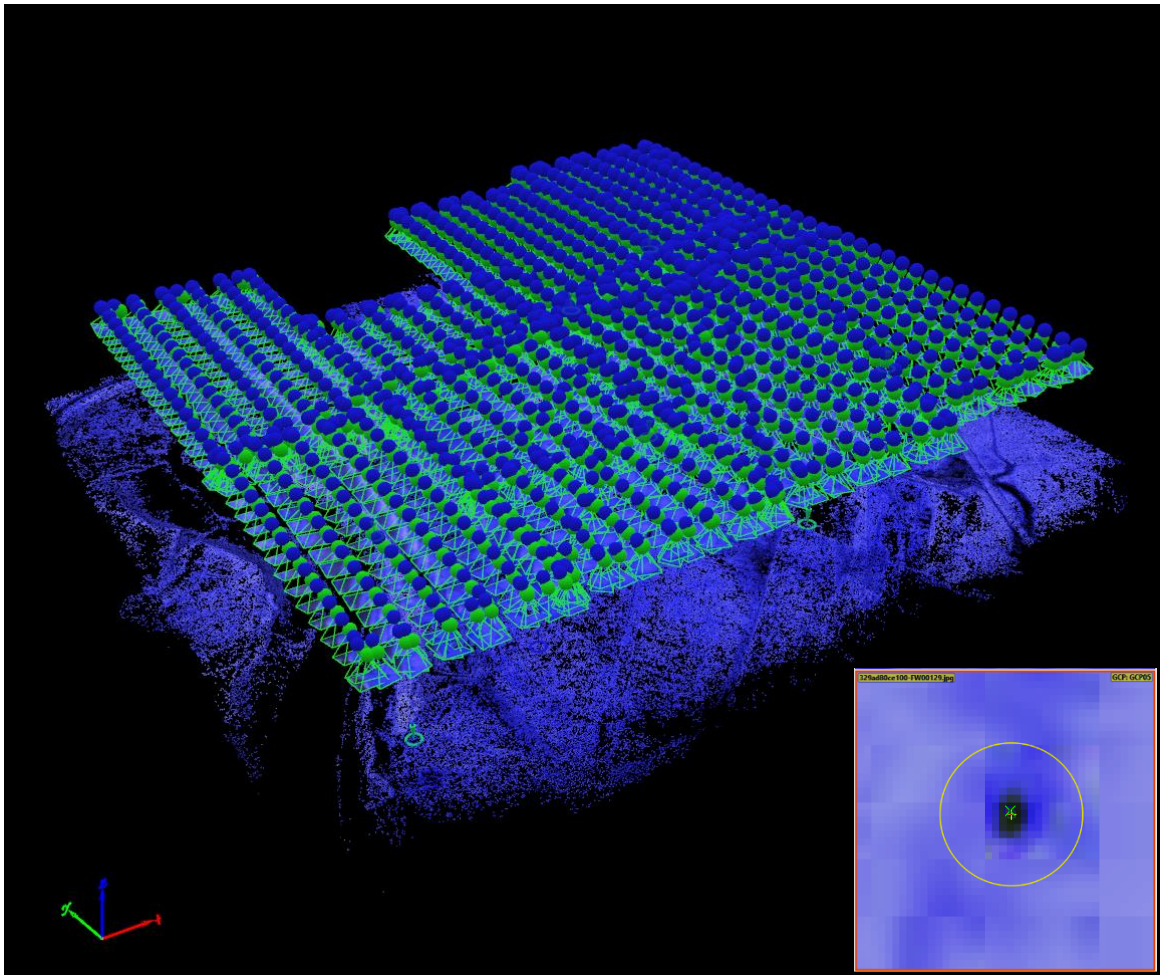

Figure 3.22: Overview of initially processed multispectral imagery in Pix4Ddiscovery; small index box in bottom right depicts the identification of a GCP target in RayCloud view (Source: Pix4Ddiscovery).

After the GCPs were selected as accurately as possible, the re-optimization step was run, and processing of the final products could be initiated. In the processing options of the last step in *Pix4Ddiscovery* (Pix4D; Version 4.2), the user can define the output file format for the orthomosaic to be created, set specific parameters to filter and smooth the point cloud for the DSM generation, and control other settings. The most important one being the setting for the radiometric calibration. Taking a picture of a radiometric calibration target in the field provides the reflectance properties of the light captured by

the camera sensor. The user can account for the illumination conditions at the day, time and location when and where the images were collected with the picture taken of the target in the field (Figure 3.2323).

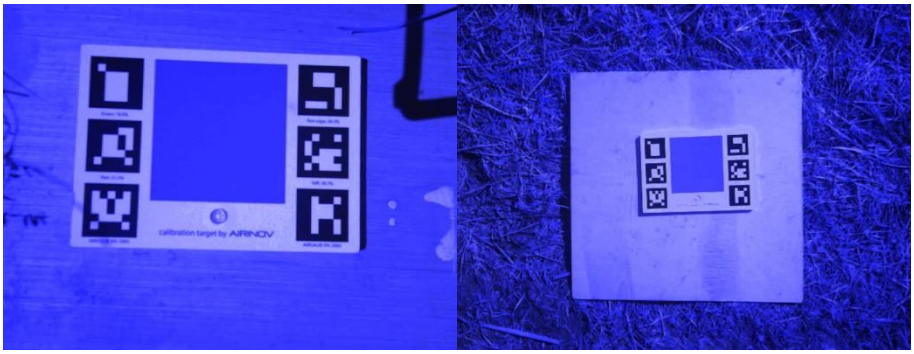

Figure 3.23: Images were taken of the calibration target in the field on 24 Sept. 2018 (left) and 5 May 2019 (right) with the Sentera Single NIR sensor (Source: ArcGIS Desktop v. 10.7.1).

On both field days, images of the calibration target were taken manually and in close proximity. The image of the calibration target on the left in Figure 3.2323 was successfully used as an input to calibrate the values of the multispectral orthomosaic from 24 September 2018; however, the image of the calibration target on the right in Figure 3.2323 brought up the following error message:

```
Error]: Unable to compute radiometric target calibration for NIR_1.2MP-
GS-0001_4.14mm-0001_0006_4.1_1248x950 (RGB) with D:/(…)/329ad80ce100-
FW00198.jpg: Too many invalid pixels (99.7004% > 5%) for band 1
```

Pix4Ddiscovery (Pix4D; Version 4.2) has trouble executing the calibration on the image if the calibration target is over-exposed. When comparing both images in Figure 3.2323, it is evident that the image on the right was not only taken from a farther distance

but also included the darker vegetation in the background surrounding the target, which likely had led to the longer exposure time on the right image from 5 May 2019. In order to overcome this issue, the exposure of the calibration target image was slightly decreased by 5 %. This avoided the error message and allowed the process to continue; however, it is critical to note at this point that the calibration does not provide absolute reflectance values anymore. This modification made it impossible to compare the data of different flights or cameras to each other. It is critical in future mission to take a close-up capture of the calibration target possibly on a bright background to avoid long exposures.

3.1.3 Preparation of Training and Validation Datasets

The sample data available for this study were gathered from various sources to increase the number of training samples necessary for machine learning classifications. The primary source was the sample data collected in the field. These were the random points created within the sampling plot locations collected for the pre-breach imagery, and the sample points collected in the field for the post-breach imagery. Both training datasets were augmented by manually selecting training points on the base of higher resolution imagery and with knowledge from the extensive field notes taken from the many visits on site. Additionally, the vegetation survey conducted by CBWES Inc. in the fall of 2017 was also added to the dataset of the pre-breach samples.

Classifications based on machine learning algorithms rely strongly on training samples. In fact, Huang et al. (2002) found that the number of training samples has a more considerable impact on classification accuracy than the algorithm used. Thus, it was

important to have training samples with an equal distribution across the site and with a proper type of sampling method.

In preparation for the classification, the sample data were transformed into the format acceptable for the *eCognition* software environment, and the class naming convention was adapted to merge all different sources of training data. In the next step, the sample points were organized and adjusted to fit a stratified random sampling method by partitioning the whole population into classes with unequal sizes according to their likelihood of occurrence. Lastly, the sample datasets were sub-divided into training samples (70 per cent) and validation samples (30 per cent) (Corcoran et al., 2015).

3.2 Phase II – Data Analysis

In Phase II of this research project, the pre-processed imagery, together with the landcover samples, were imported into the image analysis software environment *eCognition* (Trimble Developer, Version 9) for classification. The object-based classification process followed the general two-step approach of Object-based Image Analysis (OBIA). It started with the partitioning of the image scene into objects with segmentation algorithms and proceeded with the classification of the individual image objects using a machine learning algorithm. The following section details the steps of this process and outlines accuracy assessment method.

3.2.1 Segmentation

The process of object-based image analysis is, in generally, an iterative two-step approach, which starts with the initial segmentation and is followed by image classification in a second step. Segmentation means the partitioning of an image in discrete homogeneous image regions. A successful image segmentation provides

meaningful image objects matching geographical features on the earth's surface. Moreover, it provides the base for the subsequent image classification. This emphasizes the importance of proper segmentation to obtain satisfying classification results. A successful classification is directly influenced by the quality of the segmentation outcome in the first step of the object-based image analysis (Meinel & Neubert, 2004; Mesner & Ostir, 2014). There is a wide selection of segmentation algorithms for image analysis in the field of remote sensing; however, only a small selection is being made commercially available. Meinel and Neubert (2004) presented a variety of segmentation programs and evaluated different results by visual comparison. In their publication, the authors concluded to have received the best results from the software *eCognition* 2.1 resp. 3.0 (Definiens Imaging GmbH, Munich, Germany) and pointed out the high potential of it in regards to its multi-scale segmentation capabilities. The multiresolution segmentation in *eCognition* (Trimble Developer, Version 9) is one of the most popular algorithms and starts with individual pixels and grows with the bottom-up region-merging technique by grouping neighbouring pixels into image objects until it reaches the heterogeneity threshold defined by the scale parameter (Benz, et al., 2004; Drăguţ et al., 2010). The creation of homogenous image objects following the region growing algorithm can be controlled by several user-defined parameter settings, as follows.

While the scale parameter in the segmentation algorithm defines the size and number of segments to be created, *eCognition* provides the option to specify the weighting of colour, smoothness and compactness of each segment to be calculated. These three parameters alter the spatial component, whereas the coherency of image objects depends on input features, such as spectral information. The scale parameter is

one of the most critical parameters in the image segmentation process (Hay et al., 2005). Most commonly the choice of an appropriate scale parameter in relevant studies is the first challenge when using object-based image analysis (Kavzoglu et al., 2016). Since the scale parameter is not directly correlated to a specific object size, it is a new challenge to find a proper value for the parameter without some trial-and-error attempts for every new image. It is derived by multiple trial-and-error test runs, visual analysis or automated tools or algorithms to evaluate the best parameter which are still in development or their infancies in object-based image analysis. Finding an optimal scale parameter for any given image segmentation has always been a significant point of concern and scientists have since been trying to develop techniques to extract this parameter in an automized way (Flanders et al., 2003; Kim et al., 2008; Drăguţ et al., 2010).

Woodcock and Strahler proposed in 1987 a concept to measure Local Variance (LV) as the value of standard deviation (SD) in a small moving window to obtain the mean value of all the SDs measured in the entire image. The calculated mean SD value serves as an indicator for the local variability in the image and finds the appropriate pixel resolution to capture certain real-world objects. The measured SDs between the neighbouring windows are similar in case the image resolution is smaller than the real-world object. This will result in a low LV; whereas a high LV is evidence for pixel resolutions containing the real-world object (Woodcock & Strahler, 1987; Drăguţ et al., 2010).

Kim et al. (2008) took the concept of Woodcock and Strahler (1987) further and applied it to object-based image analysis. They build a relationship between the image object variance and the scale following the same principle and propose that this idea

provides the optimal scale parameter for the segmentation. The optimal scale is defined as "one that is not over-segmented, with an excessive number of segments that are on average too small, and also not under-segmented, with too few segments that are on average too large" (Kim et al., 2008, p. 293). So unlike Woodcock and Srahler (1987), who used a small moving window to obtain mean SD of the image, Kim et al. (2008) applied image objects from the segmentation step.

Both of the introduced concepts, however, focus on the extraction of that one optimal scale parameter, which is not appropriate for most of the environmental problems, requiring more than one scale parameter to cover different levels of landscape structures. Drăguţ et al. (2010) developed the ESP tool to extend this concept of Local Variance to multiscale analysis in OBIA. The ESP tool allows a fast estimation of scale parameters for multiresolution segmentation in *eCognition* (Drăguţ et al., 2010).

In this study, a hierarchical structure following the bottom-up approach was chosen within the *eCognition* (Trimble Developer, Version 9) software due to the number of samples available to train the classifier. Two different segmentation algorithms were chosen and applied to the imagery consecutively. For the initial segmentation, the *multiresolution segmentation* algorithm was used. It locally minimizes image object heterogeneity for a defined scale. This first segmentation was executed on the pixel level. The bottom-up algorithm starts with individual pixels across the image and compares its pixel values with that of pixel neighbours to merge. If the comparison between both pixels is mutually homogenous, both pixels will be combined into one image object. The procedure continues until the predefined homogeneity criteria are met (Definiens AG).

The parameters in the multiresolution segmentation algorithms were set to 0.3 for shape and 0.9 for compactness; which automatically meant that colour was weighted with 0.7 and smoothness with 0.1 respectively. The near-infrared band was doubled weighed in comparison to the remaining bands red, green, blue, and elevation. The scale parameter was set to 10 to keep the image objects created at the first level as small as possible.

The multiresolution segmentation algorithm was used to create the first level of small objects. At this point, a couple of million objects were created, who served as input for the next segmentation level. Once the level 1 objects were created, the next segmentation was continued with the *spectral difference segmentation* algorithm. The spectral difference algorithm helps to refine the existing segmentation created in the previous step by merging spectrally similar image objects adjacent to each other into a new object. The user specifies a value called *mean spectral difference* (here: 2) and defines the layer weights for the calculation (here: equal). The segmentation algorithm then merges all neighbouring image objects whose difference in mean layer intensities is below the given value by the operator. The spectral difference segmentation algorithm was executed a couple of times with varying mean spectral difference values until the image segmentation resulted in satisfying outcomes.

3.2.2 Classification

Other than the problem of finding the proper scale parameter for the best segmentation to optimize the best possible segmentation for any given image and purpose, the second biggest challenge with OBIA comes with the right choice of suitable features for the classification. Most object-based image analysis software, especially *eCognition*, offer the user a wide selection of spectral, spatial, and contextual features to

choose from. This step often requires a visual assessment of the imagery with prior expert knowledge to make a decision, which integrates a subjective component into the analysis (Laliberte & Rango, 2009). *eCognition Developer* offers a variety of algorithms and processes to classify image objects. There are basic classifications following membership values defined by the analyst. The software also offers some advanced classification techniques which implement different machine learning algorithms.

Machine learning algorithms show great potential to effectively and efficiently classify remotely sensed imagery. Their strength lies most notably in handling data with high dimensionality and in their ability to model complex class characteristics. With machine learning algorithms, it is possible to input a variety of data sources without the need to consider the source data distribution (Maxwell et al., 2018). The success of these classifiers was presented in many publications, which found higher accuracies in comparison to parametric classifiers (Hansen et al., 1996; Huang et al., 2002; Pal, 2005). Parametric classifiers, such as maximum likelihood (ML), are still the most commonly used method, although machine learning algorithms provide notably higher accuracies (Maxwell et al., 2018). This trend can, for one, be attributed to the lack of implementation of advanced algorithms into standard image-processing software packages (Yu et al., 2014), and for another, to wide-reaching uncertainties towards the effective use and implementation of machine learning techniques (Maxwell et al., 2018).

In *eCognition*, there are four different machine learning algorithms to choose between: support vector machine (SVM), decision tree (DT), random forest (RF), and k-nearest neighbour (KNN).

The Support Vector Machine algorithm aims to identify the optimal boundary within the feature space between two classes based on the position of the support vectors

(= training samples). This algorithm creates a linear class boundary, known as hyperplane, and sometimes needs to be projected to higher dimensions due to the complexity of the input data. There are many different transformations known in the literature and are referred to as kernel tricks (Maxwell et al., 2018). *eCognition* provides two different kernels, the polynomial kernel and the radial basis function (RBF) kernel, both examples of commonly used kernels within remote sensing (Huang et al., 2002). The Decision Tree algorithm is very intuitive, computationally fast, and makes no statistical assumptions. It follows a sequential approach based on a chain of simple decisions and forms a set of branches with nodes and leaves. Training data are being split into homogenous subsets based on tests applied to different feature values (Pal & Mather, 2003). Random Forest is known to result in significant improvements in classification accuracy. This classifier is an ensemble algorithm using a large number of decision trees and making a majority vote with all the trees for the most popular class (Breiman, 2001). Lastly, the k-nearest neighbour. The k-nearest neighbour classifier differs from all the other before mentioned classifiers that it does not create a model based on the training samples provided. The algorithm makes a direct comparison of each image object to the nearest known samples and assigns the class label of the most common class of the nearest neighbours in the feature space. The higher the value of k, the greater is the generalization of the classification outcome and vice versa (Maxwell et al., 2018).

The comprehensive literature review in previous sections was carried out in order to better understand the individual algorithms and their performances. It was not possible to establish a clear ranking due to a wide range of results in the broader literature. This conclusion is in alignment with the very extensive review paper of Maxwell et al. (2018) and the detailed study of Lawrence and Moran's (2015), who compared different

classification algorithms and their performances concluding that there is no single method to achieve the most accurate results in every case. The performances are more dependent on the dataset and are case-specific; and although ensemble classifiers seem to be more effective methods, the results will likely be impacted by the classes to be mapped, the training samples available, and the predictor variables (Maxwel et al., 2018). Both papers recommend analysts to experiment with multiple classifiers to determine an optimal outcome for a specific classification project.

In this study, both pre- and post-breach imagery were initially classified using the same training samples but with six different classification algorithms in *eCognition*: Decision Tree, Random Forest, Support Vector Machine with linear kernel, Support Vector Machine with RBF kernel, Bayes, and k-nearest neighbour classifier.

First, each one of these classifiers was run repeatedly with changing parameter settings. The best results were then re-assessed in the second step, by making a visual comparison of the classification results between the different algorithms. While all classifiers delivered results with varying accuracies, the k-nearest neighbor classifier did not succeed in providing an output with any validity (Appendix IV).

The outcomes of the different classifier were compared based on their most optimal ability to delineate the mud from the river class, their best performance in picking up channel features in the former agriculturally used land, and distinguishing the upland vegetation species from the high marsh species on the foreshore platform. The Random Forest classifier was identified as the best performing algorithm for the given number of training samples and data sets. The parameter settings for the Random Forest classifier are listed in Table 3.3:

Table 3.3: Parameter settings for Random Forest classifier in eCognition.

Parameter	**Setting**
Type	Random Trees
Depth	151
Min Sample Count	0
Use surrogates	No
Max categories	16
Active variables	0
Max Tree Number	500
Forest accuracy	0.01
Termination criteria type	Both

The most important parameter settings were the tree depth and the maximum tree number. Discussions with expert analysts recommended 500 for the number of the trees and an uneven number of sample counts (R. Jahncke, personal communication, January 2019).

The input data for the RF classifier were the training samples created in the previous step. The sample dataset was uploaded into *eCognition* to assign their class values to the image objects within which each of the training sample points was positioned. Once all the image objects were assigned classes associated with the training points, the sample statistics could be calculated based on the features selected, which served as input for the classifier.

The resulting classification outcome underwent minor refinements by manual modification. There are some tools available to work on some changes in the classification results within *eCognition*. The first algorithm applied was *Remove Objects* for generalization purposes and to decrease the number of image objects. First, the mode "merge by shape" was run to merge the image objects with their respective neighbouring object with which they are sharing the largest border in common. Next, the mode "merge

by colour" was run to merge the image objects with their neighbouring objects with the smallest layer value difference. Another useful tool for simplification purposes is the *Find enclosed by* tool. Here the analyst can set rules to apply for the merge of two or more objects. This helped to remove redundant or misclassified objects of small sizes across the scene, such as the shadow class. Due to the low lighting conditions prevalent at both survey dates, a large amount of shadow was cast across the image. The high resolution led to a large number of small image objects to be misclassified as such. The *Find enclosed by* tool was used to select image objects smaller than a certain threshold and with the class label "shadow" to be re-classified and merged with its surrounding class.

Lastly, the *Pixel-based object resizing* tool was run to smooth class boundaries by simplifying the image object shapes. Uneven depression can be removed by adding some pixels to the object's boundary with the function "growing"; and the same way, unevenly sharp edges can be smoothed by removing pixels with the function "shrinking". It is recommended to use those functions back to back by growing the objects first and then shrinking.

Finally, once all manual modifications and refinements were finished, the objects were exported as shapefiles into a GIS software environment for further analysis.

3.2.3 Accuracy Assessment

The accuracy of the segmentation results was assessed first and the classification outcomes later following a qualitative approach at the interim stages of this study. This section focuses on the accuracy assessment following a quantitative approach based on the final classification products and the imagery used for the classification. With the emergence of more complex satellite imagery and advanced image classification

techniques, there is growing interest to find proper measures for mapping certainty (Grenier et al., 2008). Nowadays, the validation of classification outcomes is considered to be an integral part of every remote sensing project (Mowrer & Congalton, 2000). Error estimation or accuracy assessment of classification outcomes do not only provide a quantitative evaluation and clarification about potential error, but also offer an assessment about how suitable a map is for its designated purpose (Zimmerman et al., 2013).

It is critical for any researcher or analyst working on a classification of remotely sensed data, to have a clear understanding of the appropriate techniques used for the accuracy assessment as well as a strong knowledge about the factors to be considered when using a particular assessment method (Congalton, 1991). One of the most commonly used techniques to represent the accuracy of any classification is the error matrix (Stehman & Wickham, 2011). Many scientists recommend this technique and ask it to be adopted as the standard reporting convention (Congalton, 1991), which is why the error matrix was chosen for the accuracy assessment of both classification outcomes in this study.

The error matrix expresses the number of elements classified to a particular class relative to the actual class verified on the ground. This is represented by columns, which contain the reference data, and by rows, which indicates the class information. There are three different spatial units known to be used to conduct a comparison between a map and reference data; pixels, blocks of pixels, and polygons (Stehman & Wickham, 2011). In this study, the accuracy was assessed with the use of the error matrix and was based on pixels as a spatial unit for the assessment. Furthermore, the reference sampling scheme was stratified random points based on a summary of field data, and office interpretation of remotely sensed images as reference data source, and other thematic maps (for pre-breach

only). The sample points for validation were collected the same way as the samples for training purposes and were split in a ratio of 2:1. This resulted in a total of 141 validation points for the pre-breach classification assessment and a total of 112 points for the post-breach assessment.

While the error matrix delivers a mathematically calculated reliability, it also includes indications to commission and omission errors (Congalton, 1991). The first descriptive statistic of the error matrix is the Overall Accuracy (OA). The OA is calculated by the sum of all correctly classified points, divided by the total number of validation points available for the assessment. Other descriptive statistics of the error matrix are the Producer's Accuracy (PA) and the User's Accuracy (UA). The former serves as a measure to inform the map producer (image analyst) about how well certain classes were classified on the map by providing the probability of a reference point to be correctly classified and represents the omission error of the classification. PA is calculated by dividing the sum of correctly classified points of a particular class and dividing it by the total of available reference points for that respective class. The UA represents the measure of commission errors and is calculated similarly to PA by dividing the total number of correctly classified points of a class by the total number of points that were classified as that class. This measure gives the user an indication of how representative a classified location on the map is in comparison to the actual situation on the ground (Congalton, 1991).

Another strong parameter is the Kappa coefficient. The Kappa coefficient determines if the accuracies calculated in the error matrix are significantly better or worse than a random result (Congalton, 1991). The value of the kappa coefficient ranges from 0 to 1, with 0 indicating the accuracy assessment occurred by chance, and a value of 1

indicating the lowest probability of chance agreement. In some cases, the kappa can result values as low as -1. A negative kappa coefficient indicates an agreement, which is worse than random (Sim & Wright, 2005).

Another part of the accuracy assessment involved the calculation of the positional accuracy. The geolocational accuracy of the imagery was assessed with the help of validation targets, which were placed on the field in addition to the GCP targets before the flights. Three different measurements are subject to error and were assessed in this study for both imagery; for the horizontal component, the x- and y-coordinates and for the vertical the z-coordinates.

For this purpose, the center coordinates of four different validation targets measured on the imagery were compared to the actual surveyed center points of the targets in the field. Equally, the measured elevation at the center point of the validation targets was compared to the surveyed elevation. The positional error of the imagery is expressed through the Root Mean Squared Error (RMSE) and is defined as followed:

$$RMSE = \sqrt{\frac{1}{N}\sum_{i=1}^{n}(x_i - x_c)^2}$$

While the RMSE represents the standard error of the given coordinate direction, the N stand for the sample size, x_i is the coordinate measured off of the imagery, and x_c is the actual coordinate location extracted from the validation survey points.

3.3 Phase III – Quantification and Interpretation

In Phase III of the project, the validated classification results were imported into ArcMap (ArcGIS Desktop 10.7.1) for further analysis. The main objective of this step

was to quantify the areal extents of classes and perform an analysis to correlate the class distribution with the inundation frequency on the site. Both provide essential information in understanding the changing landscape and potential drivers influencing the evolution of the salt marsh at Converse.

For this purpose, a frequency inundation map was calculated for the restoration site to understand aspects of the local hydrology and relate this information with the classes present at specific locations. A macro-enabled Microsoft Excel spreadsheet was provided by CBWES Inc., to calculate inundation statistics for Converse. The calculation required information about the tidal signal and site-specific data points in order to output the inundation frequency. The *date range* for the analysis was set from December 22, 2018, until May 5, 2019, looking at the period from the first high tides entering the site after the breach, until the day of last observation, when the survey flights were conducted. The *tide signal* input data consisted of all the predicted high and low tide levels published by the CHS, starting from the first to the last tide of the date range. These data were transformed from the chart datum into a local datum corresponding to the DSM available for the analysis before they were entered in a select format with the exact date and time. Another crucial input parameter was the *time interval* (in minutes). The analysis used a 373 minute time interval, which represents the averaged time difference between tides over the given date range.

Lastly, the hydrographic information needed to be set in relation to specific elevations at given locations on-site in order to output the statistics of inundation frequency. The specified point locations with corresponding elevation data were entered by creating random points across the site at different altitudes. The DSM, from May 5, 2019, was classified into a large number of equidistant classes starting from the lowest

point of elevation on-site up until to the highest point in 5-centimetre increments. Within each of these classes, a random point was created to extract an elevation value as input for the inundation frequency calculations. Finally, the total of all the inputs resulted in the hydrographic statistics including the inundation frequency at Converse. This included the dates and times, the heights of the tides from a specific station over a user-defined period of time, relative to a specified local datum under consideration of site elevation points.

In the last step, all the elevation-classes with the same inundation frequency were merged to represent a gradual rise in the frequency of inundation in 5 to 10% increments on a map. The finalized inundation frequency map was ultimately used to compute a geometric intersection with the classification outcomes within ArcMap in order to see the prevalent classes present within an area of specific inundation frequencies.

Chapter 4: Results and Discussion

This thesis presents semi-automated classification guidelines to improve the acquisition and monitoring approaches to understand primary processes and relationships between a salt marsh restoration site's morphology, inundation frequency, and evolution of an intertidal landscape. For this purpose, RPAS imagery were collected with multispectral information initially on September 24, 2018, before the managed realignment at the Converse Marsh and later on May 5, 2019, about five months after tidal waters were reintroduced at the site and active restoration was ongoing. For the analysis, object-based image analysis was used, and the machine learning algorithm Random Forest was implemented to improve automation and accuracies. The classification results were then used to calculate areal coverage of detected land-cover classes and correlate those with changing inundation frequencies at the Converse managed realignment site.

This chapter presents the results of the analysis and discusses their coherency and success for the overall project. First, the results of the positional accuracies of the underlying imagery are shown using the formula outlined in 3.2.3 Accuracy Assessment. The following section demonstrates the classification results with an assessment of their accuracy on the basis of an error matrix. In the last section of this chapter, the result of the inundation frequency analysis and the class intersections by area and flooding frequency is described and outlined. The chapter concludes with a discussion on the overall effectiveness of the application of the Sentera sensor and Object-based Image Analysis at a managed realignment site and provides guidelines for future efforts in semi-automated vegetation classification.

4.1 Positional Accuracy of the RPAS Imagery

In order to assess the reliability and success of the classification results, it is essential to have a clear understanding of the underlying data sources used for the analysis and their accuracy first. The positional error in any direction of the image can have a critical impact on the accuracy assessment of the classification outcome and need to be known and understood.

The statistical measure of Root Mean Square Error (RMSE) is used to indicate the positional error of the generated orthomosaics. It is derived by comparing the specific information of the elevation measured from the center point of the targets visible on the orthomosaic in relation to that surveyed center point elevations surveyed in the field (Table 4.1). The overall accuracy of the GNSS signal during the survey was less than 1 cm for both acquisition days in September 2018 and May 2019. The $RMSE_z$ for the vertical positioning is 16 cm and 13 cm for the imagery collected in September 2018 and in May 2019, respectively. The $RMSE_{x,y}$ for the horizontal positioning resulted in an error of 10 cm for both images (Table 4.2).

Table 4.1: Vertical accuracy calculation of elevation (z). Coordinates in CGVD13.

Acquisition Date	Point ID	z-coord. measured	z-coord. surveyed	diff. in z	(diff. in z)^2
Sept. 2018	VP01	5.837 m	5.903 m	-0.066	0.004356
(pre-breach)	VP02	5.612 m	5.850 m	-0.238	0.056644
	VP03	---	---	---	---
	VP04	5.921 m	5.807 m	0.114	0.012996
				Average	0.0247
				RMSE	**0.157 m**
May 2019	VP01	5.508 m	5.476 m	0.032	0.001024
(post-breach)	VP02	5.739 m	5.901 m	-0.162	0.026244
	VP03	9.024 m	8.991 m	0.033	0.001089
	VP04	5.975 m	5.785 m	0.19	0.036100
				Average	0.016
				RMSE	**0.127 m**

Table 4.2: Positional accuracy calculated for the horizontal locations (x,y). Coordinates in NAD 1983 CSRS, UTM Zone 20 North.

Date	Pt. ID	x-coord. measured	x-coord. surveyed	x-diff.	$(x\text{-diff.})^2$	y-coord. measured	y-coord. surveyed	y-diff.	$(y\text{-diff.})^2$	$(\text{diff. in x})^2 + (\text{diff. in y})^2$
Sept. 2018	VP01	401496.68	401496.76	-0.08	**0.0064**	5077130.15	5077130.17	-0.02	**0.0004**	0.0068
	VP02	401225.38	401225.35	0.03	**0.0009**	5077226.23	5077226.16	0.07	**0.0049**	0.0058
	VP03	---	---	---	---	---	---	---	---	---
	VP04	401539.37	401539.52	-0.15	**0.0225**	5077297.7	5077297.63	0.07	**0.0049**	0.0274
									Average	0.01
									RMSE	**0.10 m**
May 2019	VP01	401502.43	401502.52	-0.09	**0.0081**	5077134.65	5077134.64	0.01	**0.0001**	0.0082
	VP02	401222.76	401222.76	0.00	**0.00**	5077219.99	5077219.94	0.05	**0.0025**	0.0025
	VP03	401165.28	401165.28	0.00	**0.00**	5076972.38	5076972.49	-0.11	**0.0121**	0.0121
	VP04	401545.69	401545.82	-0.13	**0.0169**	5077297.92	5077297.89	0.03	**0.0009**	0.0178
									Average	0.01015
									RMSE	**0.10 m**

The elevation of the marsh platform and surface topography (i.e. creek networks) are critical elements for sediment availability and transport on a site, which influence the vegetative recovery of a restoring salt marsh system (Crooks et al., 2002).

The most common tool for elevation assessment on intertidal salt marshes is Light Detection and Ranging (LiDAR). The accuracies of LiDAR deployments range from 7 cm (Montané & Torres, 2006), over 15 cm (Chassereau et al., 2011), up to 30 cm in low and high marsh zones (Millard et al., 2013) depending on their point densities. Other studies have used RPAS within similar environments and reported favorable comparisons between dataset values and surveyed control points and often yielded in higher accuracies than achieved with LiDAR technology. Kalacska et al. (2017) found an averaged horizontal displacement of 1.0 to 2.9 cm and an averaged vertical elevation difference of 2.7 cm ($\pm$ 1.7 cm) calculated on three different salt marsh environments in Eastern Canada. Gonçalves and Henriques (2015) used orthomosaics and DSMs from RPAS surveys to monitor topographical changes in beaches and sand dunes reporting horizontal errors of about 3 cm and vertical errors under 5 cm. Long et al. (2016) deployed RPAS in monitoring the changing topography of tidal inlets in France and calculated RMS errors between 10 and 17 cm for the elevation accuracy. These findings are more consistent with the values report in Table 4.1. However, there are several factors that have influenced the accuracy of DSMs in this thesis.

The difference in the vertical accuracies of the orthomosaics from September 2018 and May 2019 were likely impacted by plant canopies, which were abundant in the former and at a minimum at the latter. In addition, there are several other factors that can influence the accuracy of RPAS datasets. Flight altitude, image overlap, and camera specifications can have an impact. Furthermore, the GCP configuration and number,

which is highly case sensitive, has shown to have a larger influence on the accuracy (Jeong et al., 2018). Other systematic and technical factors impacting the error values were not assessed in this research.

4.2 Classification Results and their Accuracy Assessment

Hyperspatial RGB imagery with an additional band in the near-infrared were analyzed using image objects and the random forest algorithm. This resulted in two landcover classifications of the restoration site at Converse: a pre-breach classification from September 24, 2018, and a post-breach classification from May 5, 2019.

The first classification was based on the pre-breach imagery from September 24, 2018, and shows the initial land cover classes and their conditions on-site prior to the restoration (Figure 4.1). The accuracy of the pre-breach classification was assessed by validating the outcome with an error matrix using a total of 141 validation points (Table 4.3). The overall classification accuracy was 61% with a Kappa of 0.55.

Due to the fact that there was no specific requirement in differentiating upland vegetation communities, some classes were summarized into one single category. The category Fallow Land contains the sub-classes of *Alopecurus pratensis*, *Calamagrostis canadensis*, Old field, Old field low, and Tall Species. The Pasture category contains both classes Pasture Grass and Pasture Grass mowed classes.

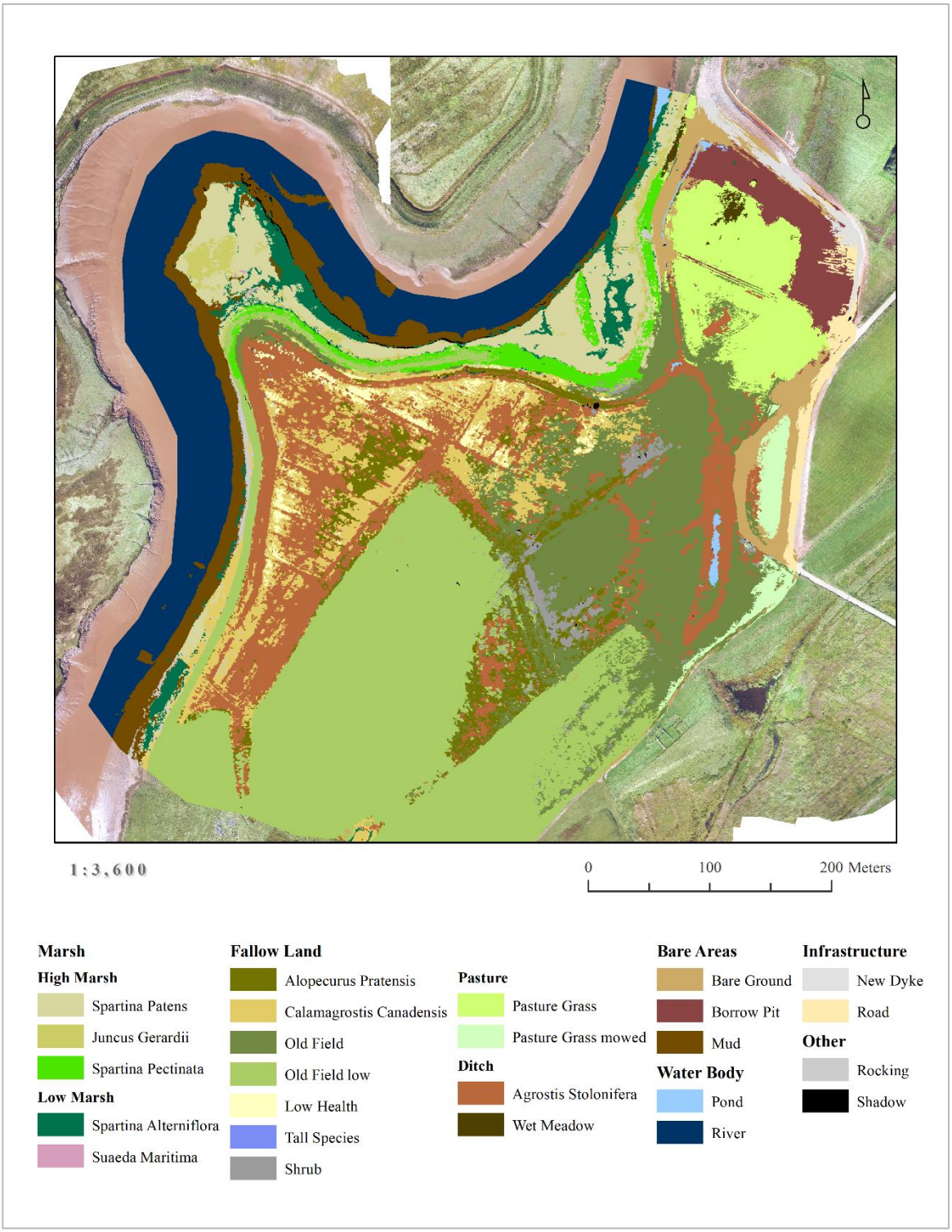

Figure 4.1: Classification result of pre-breach imagery (24 Sept. 2018) using Random Forest.

Table 4.3: Error Matrix of pre-breach classification.

Classes	Bare Ground	Mud	patens	J. gerardii	S. pect.	S. marit.	S. alt	Fallow Land	Pasture	Agr. Stol.	Wet Meadow	Rocking	Low Health	Total	User Accur.
Bare Ground	1	0	0	0	0	0	0	0	0	0	0	0	0	1	100%
Mud	0	0	1	0	0	0	0	0	0	0	0	0	0	1	0%
patens	1	0	19	7	1	0	4	2	1	0	0	0	0	35	54%
J. gerardii	0	0	1	15	0	0	0	0	0	0	0	0	0	16	94%
S. pect.	0	0	1	1	2	0	0	2	0	0	0	0	0	6	33%
S. marit.	0	0	0	0	0	0	0	0	0	0	0	0	0	0	0%
S. alt	0	0	0	0	1	1	15	0	0	0	0	0	0	17	88%
Fallow Land	1	0	0	0	0	0	0	18	8	0	0	0	3	30	60%
Pasture	0	0	0	0	0	0	0	0	8	0	0	0	0	8	100%
Agr. Stol.	2	0	0	0	0	0	0	14	0	3	1	0	0	20	15%
Wet Meadow	0	0	0	0	0	0	0	0	0	0	4	0	0	4	100%
Rocking	2	0	0	0	0	0	0	0	0	0	0	0	0	2	0%
Low Health	0	0	0	0	0	0	0	0	0	0	0	0	1	1	100%
Total	7	0	22	23	4	1	19	36	17	3	5	0	4	141	
Producer Accuracy	14%	0%	86%	65%	50%	0%	79%	50%	47%	100%	80%	0%	25%		
Overall Accuracy	61%														
Kappa Coefficient	0.55														

Reference

Classified

Different plant species were differentiated within the Fallow Land category, which was formerly used as Agricultural Land. The Sentera sensor was able to detect species with varying plant structures, chlorophyll and water content otherwise not detectable within the visible light of the electromagnetic spectrum. Similar results were observed by Hardisky et al. (1986) when they reported significant changes in the spectral response of varying plants caused by high absorption of red by chlorophyll and an increase in reflectance values within the near-infrared due to intra- and interleaf scattering.

The greater challenge came with the differentiation of the high marsh class *Spartina patens* from the upland classes, such as Old Field and *Calamagrostis canadensis*. Equally, the other high marsh species *Juncus gerardii* was also difficult to separate from species in the Low Health class or even the other high marsh species *Spartina patens* due to strong spectral and structural (textural) similarities caused by the lack of chlorophyll within those species that late in the season (Ozesmi & Bauer, 2002; Moffett & Gorelick, 2013). For this reason, the spatial component was added to the classifier in addition to the spectral features. This resulted in the successful separation of high marsh species from vegetation classes in the upland.

The most considerable misclassification occurred for *Spartina pectinata*. As observed in the field, Sp*artina pectinata* occupied a few small patches along the dyke at the back of the fringe marsh. On the classified map, however, it appears along half of the old dyke including the remnant Acadian dyke on the foreshore fringe where it was not actually present. Another point to mention here is the over-estimation of the freshwater plant species in the category ‘Ditch’. According to the classification result, *Agrostis stolonifera* grows in the immediate vicinity of ditches and water saturated ground, which

is also confirmed by field observations. However, the coverage on the classification map seems to be denser than it was actually observed on the ground and should contain a larger variety of upland classes (Figure 4.2).

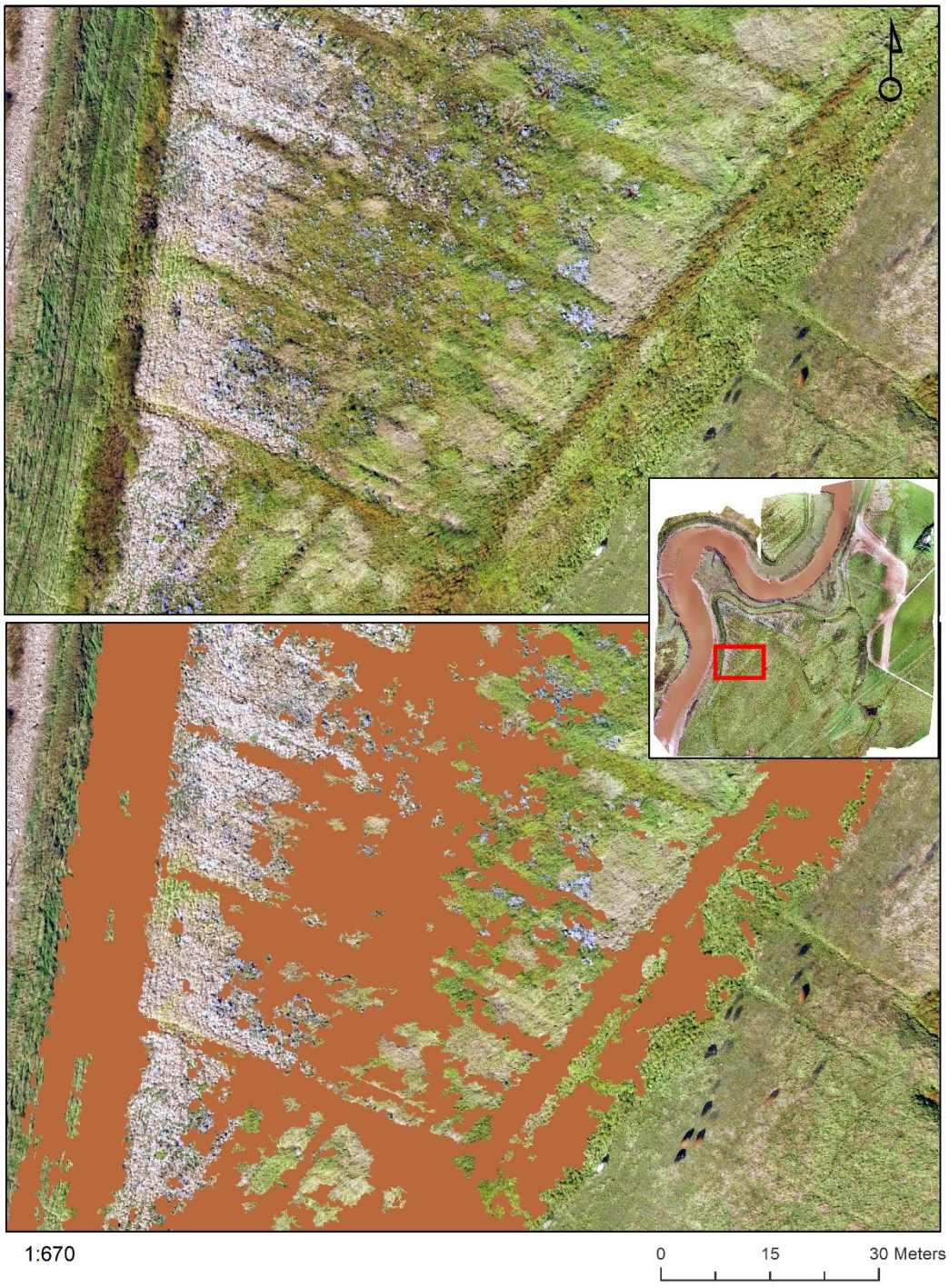

Figure 4.2: Close-up view to an area with large coverage of Agrostis stolonifera class. Top image shows RGB orthomosaic in true colour, bottom image shows an overlay of the the RGB-orthomosaic and the classification outcome with selected class.

The main ditch in particular along the dyke road is largely overestimated by including the dyke road with mixed upland class. One potential explanation could be the fact that water strongly absorbs light within the near-infrared channel. This results in measurements showing very significant differences within those plants when comparing to drier vegetation classes. Another explanation could be the adverse effects of the refinement tools applied at the end of the classification process. The "growing" function and "merge by shape" tool can cause areas to overgeneralize, while other classes experience the opposite effect (Gao & Mas, 2008). The areas classified as Old Field and Old Field low, for example, are correctly identified as such even though there is high variability within the respective classes.

Following a visual comparison of all the classification outcomes from the different machine learning algorithms, the random forest outcome performed the best in detecting the Mud class (Appendix IV). However, minor issues can still be detected within the River class. A few objects within the River were assigned to the Mud class, which is likely caused by the high sediment content in the water (> 500 mg/l) or not enough training samples to get a more explicit spectral response.

Low marsh species and high marsh species were successfully separated, except for the very small population of *Suaeda maritima,* whose occurrence is less frequent than other classes, and its existence is geographically localized to one section of the foreshore marsh. Moreover, the species transitions into the very sparse population of *Spartina alterniflora (*Figure 4.3 *&* Figure 4.4*).* When the RPAS imagery where collected for the pre-breach classification (Sept. 24, 2018) the *Suaeda maritima* species was already green

and partially even slowly dying off due to the time of the season. This situation led to similar spectral responses between the *Suaeda maritima* and the *Spartina alterniflora* classes, particularly in the transitioning zones, causing difficulties in the classification, thus, the underrepresentation of the former (Figure 4.5).

Figure 4.3: Suaeda maritima in earlier development stage (red species) with young Spartina alterniflora (green). Picture was taken on foreshore platform on July 4, 2018 (Reyhan Akyol)

Figure 4.4: Suaeda maritima in a later development stage (small green) with young Spartina alterniflora (taller green leafs). Picture was taken on foreshore platform about a month later than the previous on August 2, 2018 (Reyhan Akyol).

Figure 4.5: Close-up view to an area with Suaeda maritima. Top image shows RGB orthomosaic in true colour with locations of pictures taken indicated with blue points. Bottom image shows an overlay of the the RGB-orthomosaic and the classification outcome with selected class.

There are no validation points available for the classes Pond, River, New Dyke, Road, and Borrow Pit due to accessibility difficulties and prioritization. Out of 13 classes used in the accuracy assessment, five of the classes show a user's accuracy of 94% and 100%. The best results are in the classes Bare Ground, Pasture, Wet Meadow, and Low Health. *Juncus gerardii* has a user's accuracy of 94%. The classes with the lowest user's accuracy are Mud, *Suaeda maritima*, and Rocking. The low UA for those classes were expected due to the fact that there were no sample points provided. One sample point of *Spartina patens* got incorrectly classified as mud, and two bare ground samples were incorrectly classified as rocking, which explains the 0% accuracy in both of these classes. *Suaeda maritima* also has a UA of 0%. This is due to the fact that there was only one validation point available for this class, and that point was incorrectly classified as *Spartina alterniflora*.

The second classification provides an assessment of the restoration site in May 2019 after the snow had melted and temperatures allowed us to safely fly after the breach in December (Figure 4.6). The greatest challenge of this classification was the relatively low spectral variability across the whole scene. Almost all the vegetation on site was dead due to the winter, except for fresh grass which started growing earlier in the season and the Old Field (green) class, which includes sections of the Old Field class starting to green up.

Most of the classes were labelled with reference to the actual observations made on-site. Some of the class labels are further described for clarification in Table 4.4. The accuracy was assessed by means of an error matrix (Table 4.5) and included 112 validation sample points.

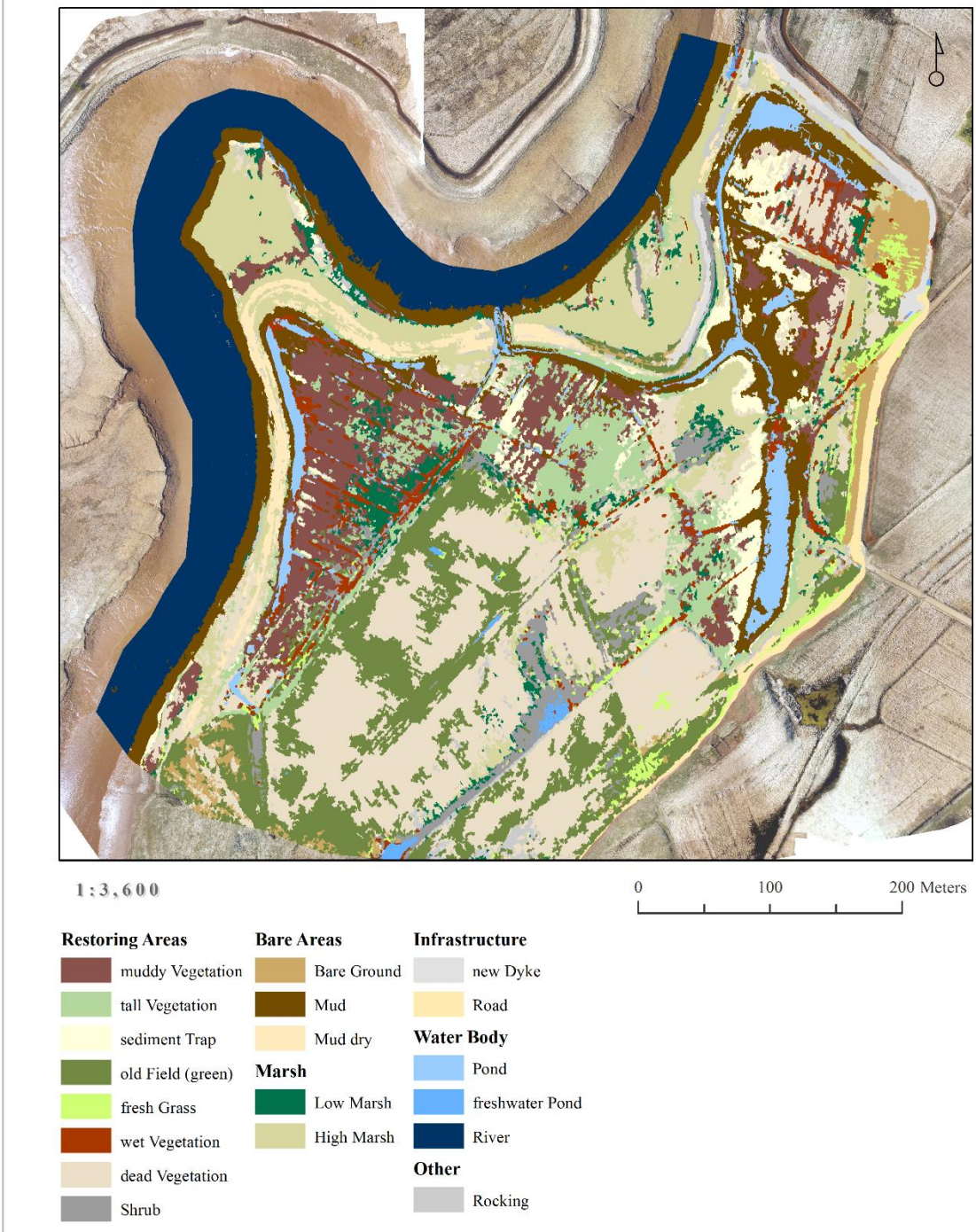

Figure 4.6: Classification result of post-breach imagery (5 May 2019) based on the Random Forest classification algorithm.

Table 4.4: Selection of post-classification class description.

Class name	Description
Pond	Ponding and stagnation of tidal water on depressions at the site
wet Vegetation	Vegetation that is not entirely submerged, but is situated in very shallow water so much that the bottom of the vegetation is not dry
muddy Vegetation	Vegetation that is still noticeable, however, covered with a significant amount of mud
sediment Trap	Vegetation that is covered with dried sediments on its leave blades and stems, which got deposited/trapped in plant structure at times of inundation.
dead Vegetation	Vegetation with very low chlorophyll content
tall Vegetation	Vegetation with very dense and long-reaching leave blades situated at a higher elevation than surrounding classes and is as such less often inundated. Does not show any signs of sediments trapped in its structure.

The accuracy assessment of the post-breach imagery resulted in higher accuracies when compared to the pre-breach imagery. With a total number of 112 validation points across 19 different landcover classes, the overall accuracy resulted in 71% with a Kappa value of 0.69 (Table 4.5).

Table 4.5: Error Matrix of post-breach classification.

Classes	Reference: Bare Ground	Mud	dry Mud	High Marsh	Low Marsh	muddy Vegetation	tall Vegetation	sediment Trap	old Field (green)	fresh Grass	wet Vegetation	dead Vegetation	Shrub	new Dyke	Road	Pond	freshwater Pond	River	Rocking	Total	User's Accuracy
Classified: Bare Ground	3	1	0	0	0	0	0	0	0	0	0	0	0	0	0	0	0	0	0	4	75%
Mud	0	7	0	0	1	3	0	0	0	0	1	0	0	0	0	1	0	0	2	15	47%
dry Mud	0	0	3	0	0	0	0	0	0	0	0	0	0	1	0	0	0	0	0	4	75%
High Marsh	0	0	0	8	0	0	0	0	0	0	0	2	0	0	0	0	0	0	1	11	73%
Low Marsh	0	0	0	0	3	0	1	0	0	0	0	0	0	0	0	0	0	0	0	4	75%
muddy Vegetation	0	0	0	0	0	5	0	0	0	0	0	1	0	0	0	0	0	0	2	8	63%
tall Vegetation	0	0	0	0	0	0	6	1	0	0	1	1	0	0	0	0	0	0	0	9	67%
sediment Trap	0	0	3	0	0	0	0	5	0	0	0	1	0	0	0	0	0	0	0	9	56%
old Field (green)	0	0	0	0	0	0	0	0	5	1	0	0	0	0	0	0	0	0	0	6	83%
fresh Grass	0	0	0	0	0	0	0	0	0	4	0	0	0	0	0	0	0	0	0	4	100%
wet Vegetation	0	0	0	0	0	0	0	0	0	0	2	0	0	0	0	1	0	0	0	3	67%
dead Vegetation	0	0	1	0	0	0	0	1	1	0	0	3	0	0	0	0	0	0	0	6	50%
Shrub	0	0	0	0	0	0	0	0	0	0	0	0	5	0	0	0	0	0	0	5	100%
new Dyke	0	0	0	0	0	0	0	0	0	0	0	0	0	6	0	0	0	0	0	6	100%
Road	1	0	0	0	0	0	0	0	0	0	0	0	0	0	0	0	0	0	0	1	0%
Pond	0	0	0	0	0	0	0	0	0	0	1	0	0	0	0	6	0	0	0	7	86%
freshwater Pond	0	0	0	0	0	0	0	0	0	0	0	0	0	0	0	0	2	0	0	2	100%
River	0	0	0	0	0	0	0	0	0	0	0	0	0	0	0	0	0	3	0	3	100%
Rocking	0	0	0	0	1	0	0	0	0	0	0	0	0	1	0	0	0	0	3	5	60%
Total	4	8	7	8	5	8	7	7	6	5	5	8	5	8	0	8	2	3	8	112	
Producer's Accuracy	75%	88%	43%	100%	60%	63%	86%	71%	83%	80%	40%	38%	100%	75%	0%	75%	100%	100%	38%		
Overall Accuracy	71%																				
Kappa Coefficient	0.69																				

The classification outcome of May 2019 already provides an initial view of the changing system by providing indications about inundation frequency and extent across the study site. The Mud class indicates areas of most frequent flooding, followed by the wet Vegetation, muddy Vegetation, and sediment Trap, forming a visible zonation between classes. The western section of the study site is widely covered with wet and muddy Vegetation, indicating that this section does not drain as fast and successfully as the north-eastern areas. This is in strong accordance with field observations (Figure 4.7).

Figure 4.7: Field pictures of examples of the muddy vegetation class (left) and the wet vegetation class (right) (NA, August 1, 2019).

The first sprouts of grass growing on the site appear on the farthest edge of the site where there has been no tidal inundation according to predictions and models. Another point to mention is the old section of the road, which is almost non distinguishable at the classification outcome and appears to be now covered by mud (Figure 4.8).

A further interesting observation is the missing low marsh class at the fringe marsh (Figure 4.9). As spectral separability between marsh species can be challenging

depending on the season. The disappearance of the class can also be an indication for the die-off of *Spartina alterniflora* during the winter or massive ice shear processes.

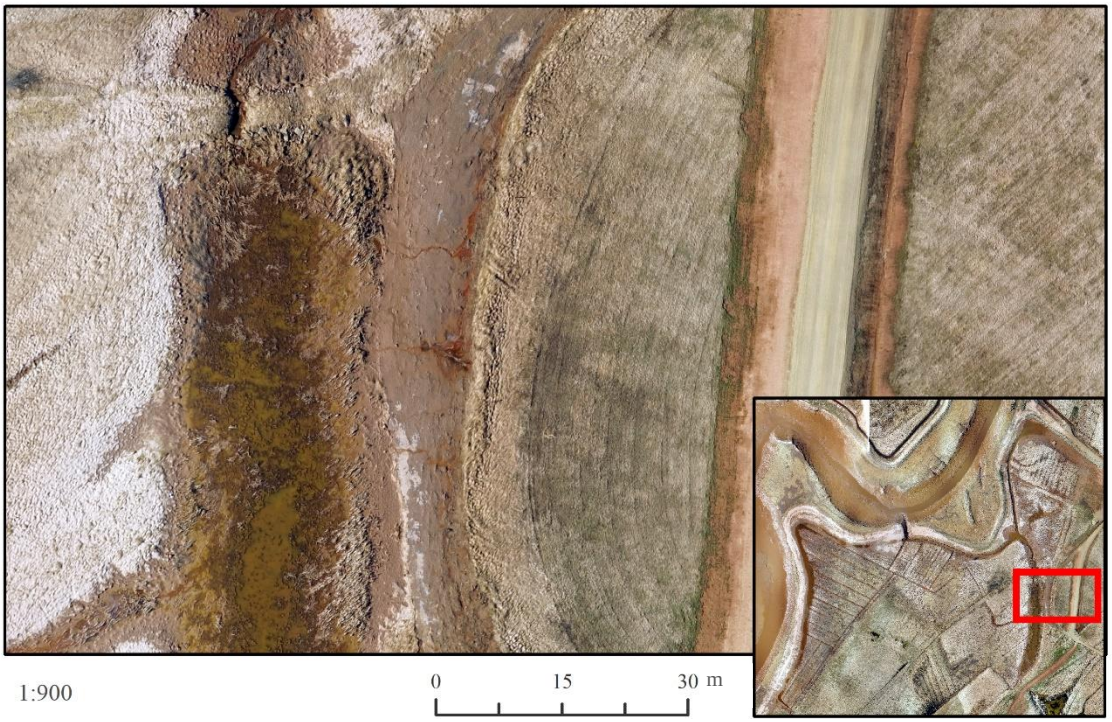

Figure 4.8: Close-up view of the old dyke road covered by mud.

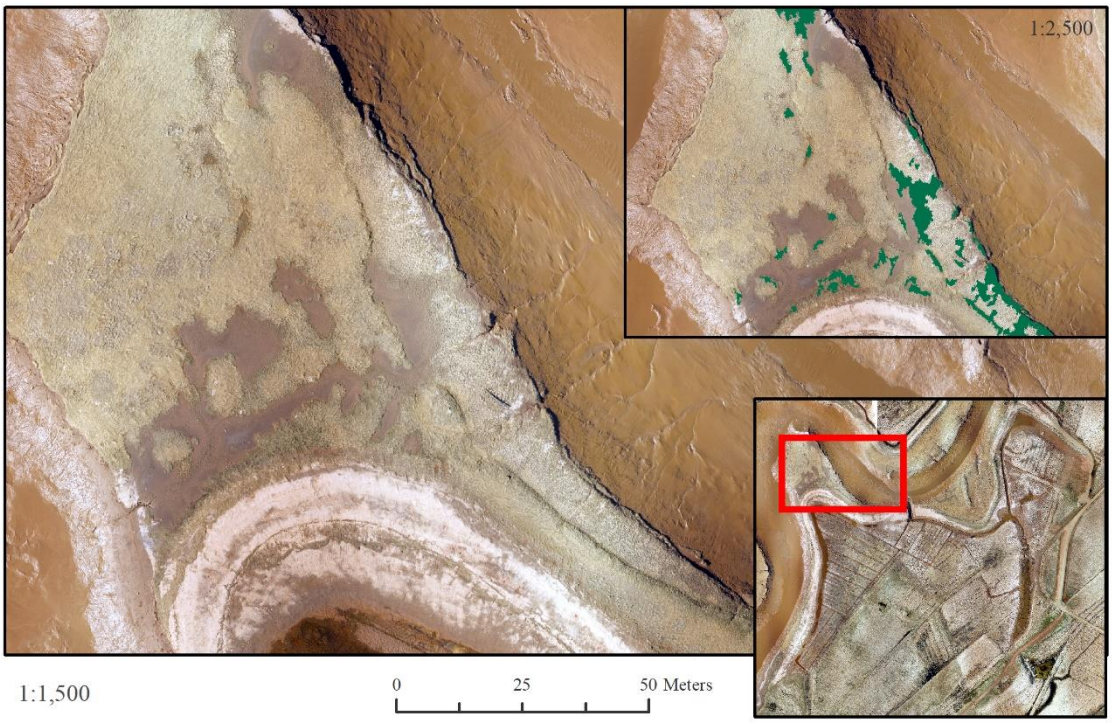

Figure 4.9: Close-up view north-western section of the foreshore marsh platform showing the difficulties of the classifier to detect Spartina alterniflora on the May 2019 imagery.

The classes fresh Grass, Shrub, New Dyke, freshwater Pond, and River have a user's accuracy of 100%. Only the Road class has a UA of 0%. The classes muddy Vegetation and wet Vegetation have UA of 63% and 67%, respectively. The Mud class has a UA of 47%, while the PA resulted in 88%. The UA is so much lower than the PA because muddy vegetation class points were incorrectly classified as Mud. Dead Vegetation has a UA of 50%, caused by falsely classified points belonging to dry Mud, sediment Trap, and Old Field (green).

There are a number of factors that can influence the accuracy of classification results. The accuracies indicated in the error matrices are presented with the knowledge that the ground truth data is correct and accurate with the use of the RTK-GNSS instrument. The impact of human error and judgment was minimized by the use of pre-determined code-lists in the RTK-GNSS instrument and the implementation of the double-check system while recording and transferring field notes (Carlotto, 2009).

There are some other factors, which can influence the accuracy of maps created by Object-based Image Analysis, which cannot be separately quantified but will be outlined to explain the accuracy assessment results of the error matrix. As discussed in earlier chapters of this work, there are many benefits of the use of RPAS imagery in tidal salt marsh restoration monitoring (Klemas, 2015; Zweig et al., 2015). However, in the process of this study, some of the disadvantages of the specific RPAS and camera sensor used in this study emerged and need more attention before future analysis (Kelcey & Lucieer, 2012). Digital cameras mounted to Remotely Piloted Aircraft offer the high spatial resolution to investigate these highly complex and diverse systems in the intertidal zones, however, missing information to transform Digital Numbers (DNs) into reflectance units by radiometric calibration limits how the data can be applied to monitoring changes and measuring development on a restoration site (Smith & Milton, 1999). In particular, the insufficient sensor quality and the missing camera specifications deployed in this project do not meet the requirements to successfully automatize a classification process. Other studies have observed similar constraints in low-cost sensors reporting low radiometric data qualities low signal-to-noise capabilities of smaller systems, which compromise data reproducibility (Anderson & Gaston, 2013; Pande-Chhetri et al., 2017). The geometric stability and vibration effects of the RPA can also have an impact on the data quality. This

is particularly relevant for the Sentera sensor which did not have a gimbal mount, therefore low data quality was suspected to be caused by unrealistic values observed during the processing and analysis stages.

One additional source of error influencing the final classification results can happen during the initial segmentation step. When image objects are being created with trial-and-error approaches, the results are highly sensitive to subjectivity and inconsistency by the hands of the analyst (Arvor et al., 2013). The over- or under-segmentation are the two types of errors that can be introduced in the segmentation step. Under-segmentation causes a large number of objects that results in very long processing times in *eCognition*. Likewise, over-segmentation introduces too large varieties within objects and do not provide image objects representative of real-world objects. Both of these errors can reduce the classification accuracy if not chosen appropriately (Liu & Xia, 2010). Another crucial point is the use and parameter settings of the algorithms used for the classification, as well as the features included in the classification process. The greater the number of the features selected for a given classification, the higher the dimensionality for the classification and, with that, the complexity of the analysis itself (Ma et al., 2017). A third factor is the sampling unit chosen to run the accuracy assessment itself. Since a per-pixel based approach as the unit of assessment for the accuracy, the sensitivity of a pixel to positional errors plays another important role (Stehman & Wickham, 2011; Ye et al., 2018). Lastly, the accuracy of the classification results can be impacted by the high sensitivity of the Random Forest classifier to training data characteristics, sample size, class proportion and spatial autocorrelation as it was demonstrated in Millard & Richardson (2015).

The effectiveness of remote sensing projects has seen considerable advancements by incorporating non-parametric statistical classifiers, such as the Random Forest. As discussed earlier, the RF algorithm is based on a defined number of decision trees and has the advantage of being able to incorporate data of multiple sources and different scales with high computational efficiencies (Timm & McGarigal, 2012). Other studies tested different scenarios of parameter settings for the RF algorithm and reported minimal to no-change in accuracy with a larger size of Random Forest of 500 trees (Timm & McGarigal, 2012; Corcoran et al., 2015). Corcoran et al. (2015) tested three different methods to train the Random Forest classifier with a) point samples with single pixel values, b) a buffer area sample using the average value of all the pixels within the window of 5x5 pixels around the reference point, and lastly, c) statistical values of image polygons intersecting with a reference points. For all those three methods sample points were collected following the stratified random principle and split into unequal parts of training data (75%) and validation data (25%). The results showed the highest overall accuracies for the classification outcome with based on objects and reported an overall accuracy of 77% (Kappa = 0.72) at one site and 93% (Kappa = 0.92) at another. These results show the high potential of using OBIA with Random Forest for wetland mapping. Correll et al. (2019) classified eight broad classes in a tidal marsh system on the east coast of the United States using three different machine learning algorithms in comparison. Their results showed that Random Forest outperformed the other classifier with an overall mapping accuracy of 90% and found mean classification accuracies of 94% for the class of high marsh and 76% for low marsh delineation. Pande-Chhetri et al. (2017) compared the performance of different machine learning algorithms by using RPAS imagery and OBIA and achieved an overall accuracy of 70.8% using Support Vector Machine.

The implementation of Random Forest to classify intertidal wetlands using complex datasets is a valid approach. However, it requires input datasets with higher quality in order to provide results with higher accuracies and reliability. The near-infrared band of the Sentera sensor did not provide the actual spectral resolution information. Moreover, the lossy-compression format contributed to the loss of important spectral information in pixel values with every pre-processing step applied.

4.3 Inundation Frequency Map and Landcover Class Distribution

The validated classification maps could now be interrelated with the inundation frequency map to identify potential correlations and find any conclusions from the results. The frequencies range from 0% up to 100% and describe how, and where, areas got inundated and how often between December 21, 2018, and May 5, 2019 (Figure 4.10).

The mudflats along the shoreline of the Missaguash River, together with the breach location, are the areas that were inundated for 100% of the defined time interval (373 minutes). The whole extent of the borrow pit was inundated with every high tide about one-third of the time. The majority of the restoration site only got inundated for 20% of the time. Whereas the areas on the western part of the site, which were identified to be wetter in both pre- and post-breach classification results, got inundated a bit more frequently, 25-30% of the time. The foreshore marsh platform was less frequently inundated, with values ranging between 10 and 15%. Most of the sections of the old dyke, which have been levelled, were never or only 5 to 10% of the time inundated.

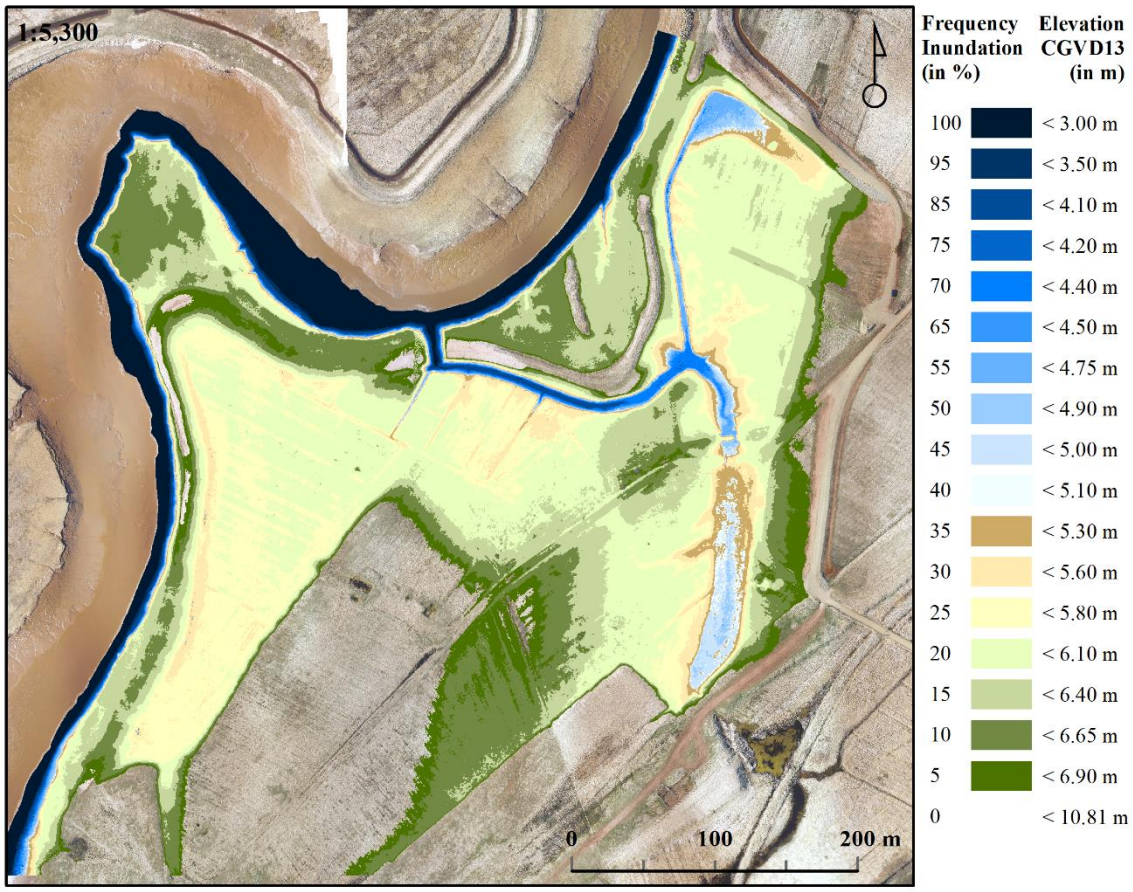

Figure 4.10: Frequency Inundation Map of Converse Marsh. Inundation frequencies in percent with respective elevations within each class indicated in metres (CGVD13). Calculations based on post-breach DSM (May 5, 2019) and high tide level predictions of CHS (Pecks Point CD to CGVD13 offset value = 6.69 m) for the time between Dec. 21, 2018, and May 5, 2019. Background image: Orthomosaic May 5, 2019 (DJI Phantom 3 Pro).

With the help of the intersect tool in ArcMap, all classes of the post-breach classification outcome that fell under the respective inundation frequency classes were quantified in a separate dataset. The datasets were then used to identify potential relationships and coherences between land cover classes and inundation frequencies (Figure 4.11).

In the case of the post-breach classification, areas with the lowest frequency of inundation contain mainly plant species from the fallow agricultural land. The high marsh species occupy almost half of the total area in the 10% inundated frequency class.

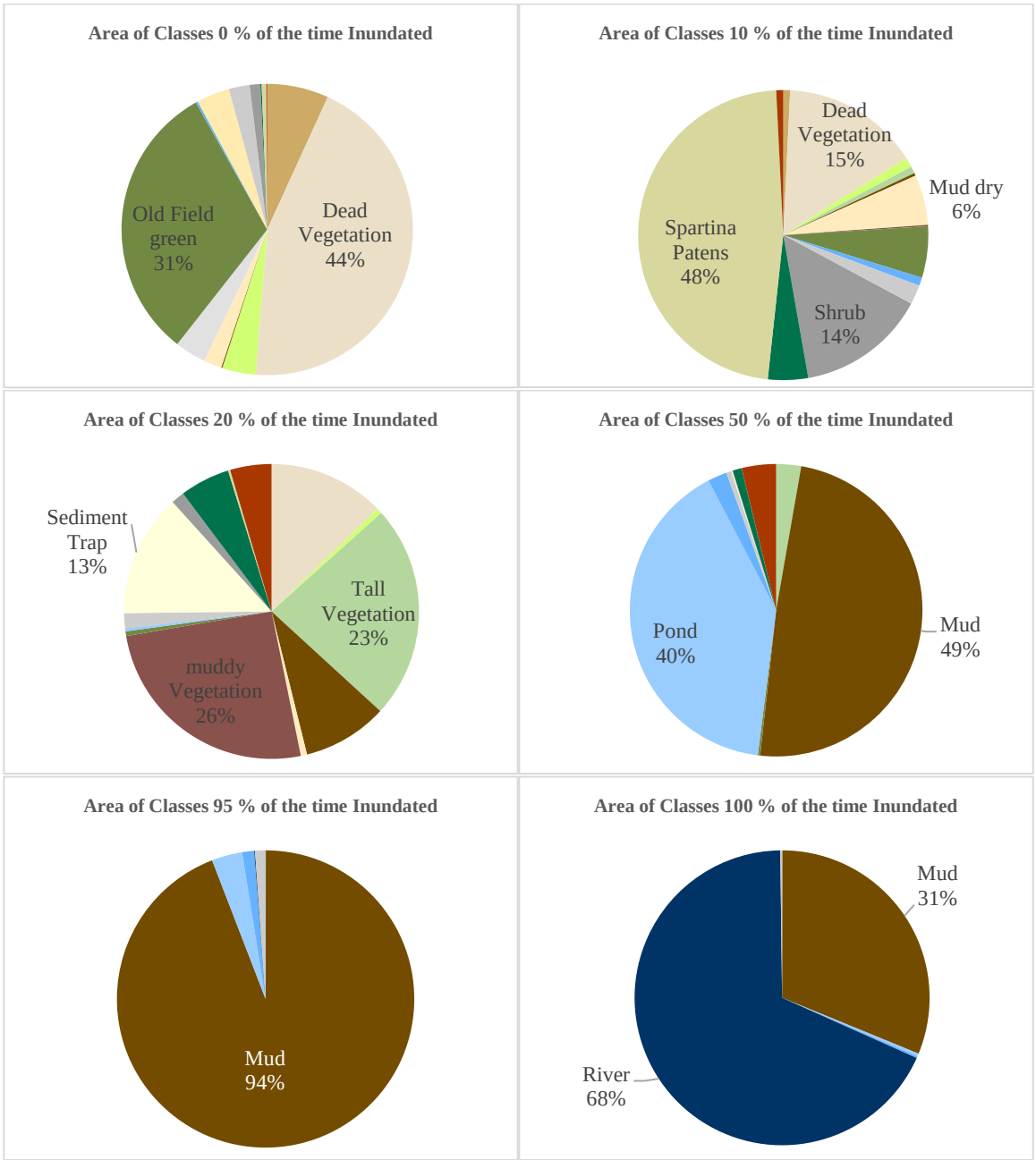

Figure 4.11: Proportion of classes present with rising inundation frequency in percentage.

As the inundation frequency continues to increase, the high marsh species and dry Mud class decrease in area, while the sediment Trap and muddy Vegetation classes take over more space. High marsh species, such as *Spartina patens* for example, are known to occupy predominantly the intermediate elevations belonging to the higher end of the tidal frame with their inability to tolerate longer inundation times (Millard et al., 2013; Porter et al., 2015). At 50% of inundation frequency, more than half of the area is classified as Mud and the other half with ponding water. The areas inundated up to 95 and 100% of the time mainly consist of Mud and River (Figure 4.11).

An overview of all classes apportioned to the area inundation frequencies is given in Figure 4.12. The largest extent of inundation on the site happened only 25% of the time between Dec. 21, 2018, and May 5, 2019, indicating that only a small area of the restoration site has been inundated frequently.

In Figure 4.13, the classes are proportional to the total of the area within each inundation frequency class plotted. The Mud class in the post-breach classification shows an unusual pattern. At 95% of inundation frequency, the Mud class takes up almost all the area and continues with a falling trend until 45% inundation frequency, with the exception at 65% inundation frequency, where it shows an increase of about 15% in area coverage. Within the area of 50% inundation frequencies, the Mud class takes up nearly half of the total area inundated. At 35% inundation frequencies, the mud coverage within that area shows a very sudden increase up to almost 90%, only to continue to decrease slowly with frequencies of less than 30%. The observed anomaly of a jump in the mud class at 65% and 35% inundation frequencies likely indicates a rapid deposition of sediments from the flooding tide at the upper edge of the creek bank and the thalweg of the creek respectively (Figure 4.14).

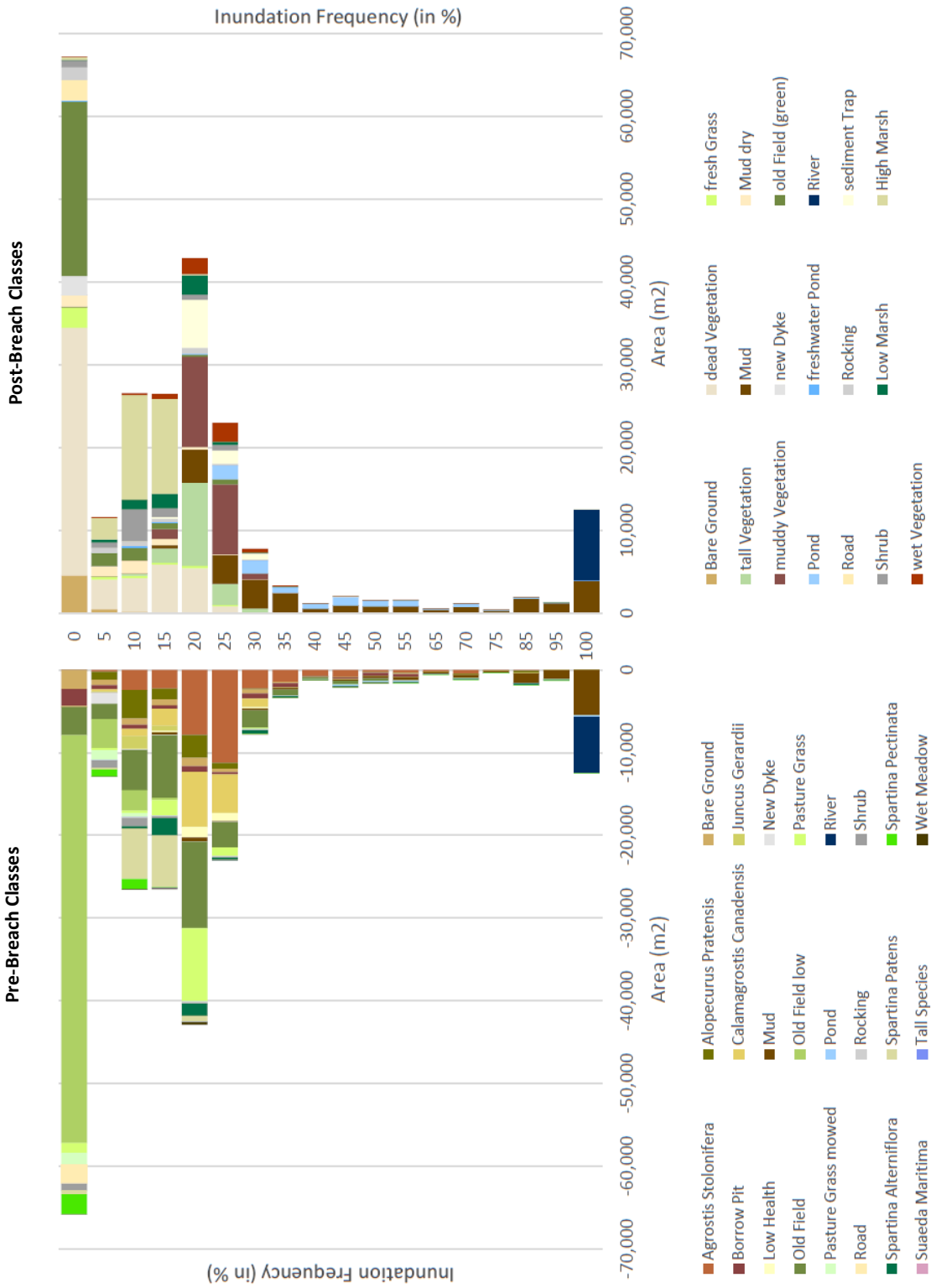

Figure 4.12: Correlating area of pre-breach classes (left) with the area of post-breach classes (right) by their occurrences in certain inundation frequency levels.

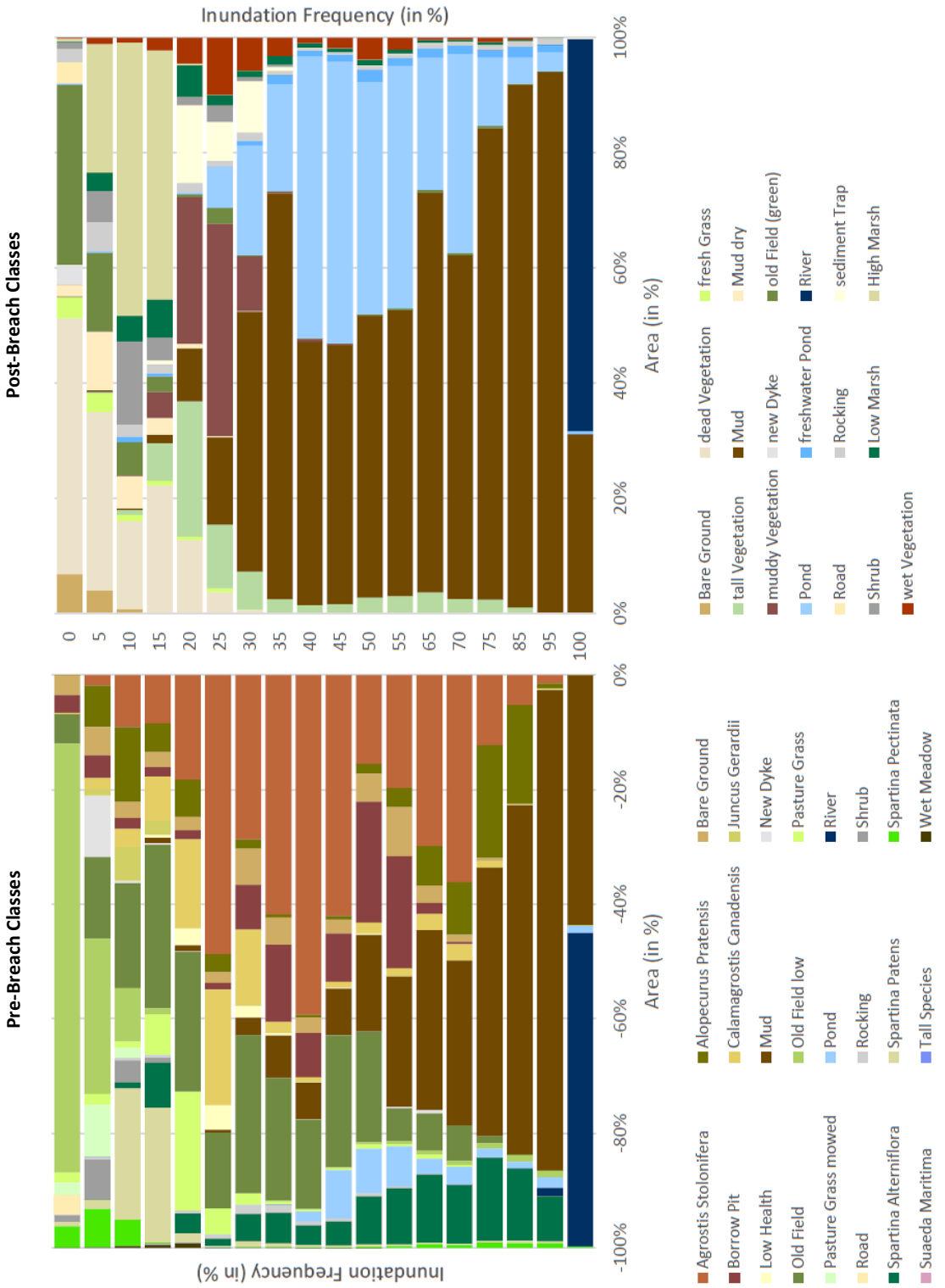

Figure 4.13: Correlating proportional area of pre-breach classes (left) with the proportional area of post-breach classes (right) by their occurrences in certain inundation frequency levels.

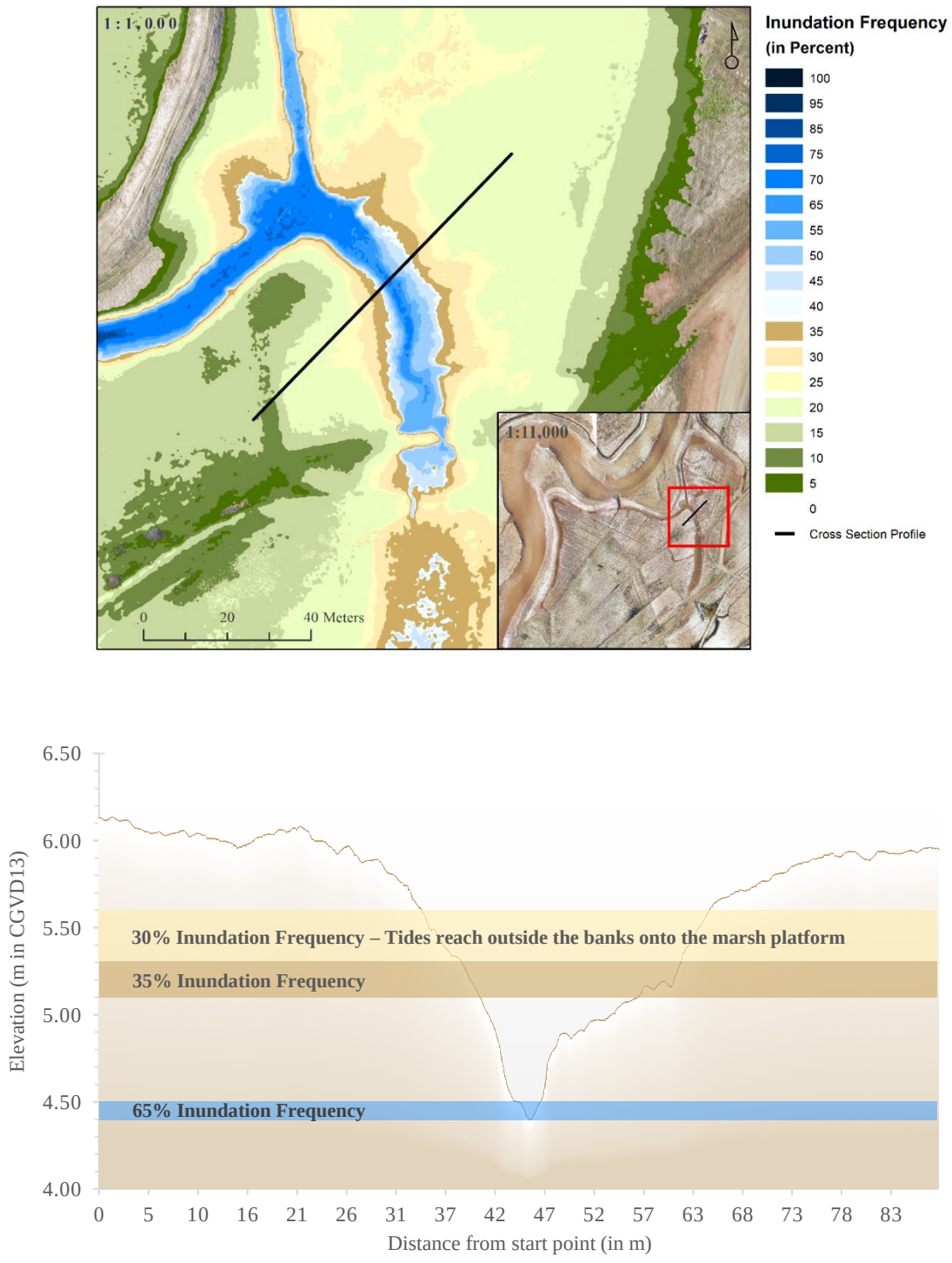

Figure 4.14: Cross-section of main channel at Converse highlighting significant sediment deposition at 35% and 65% inundation frequencies and indicating 30% mark, where inundation beyond these frequencies and elevation moves outside the channel reaching the marsh platform.

High suspended sediment concentrations increase flocculation rates, which leads to an increase of the clearance rate in a water column, and with that, the time to form flocs decreases subsequently initiating the settling (Kranck, 1980, as cited in Poirier et al., 2017). Other studies focused on suspended sediment dynamics and deposition patterns showing notable water clearance and settling during calm flow conditions (Milligan et al., 2007; O'Laughlin et al., 2014). These conditions are present usually at maximum tidal amplitude and where an increase of sediment deposition is observed.

Between 20% and 25% inundation frequencies, the muddy Vegetation and the wet Vegetation class show their largest extent (Figure 4.12) and take up together almost more than half of the total area associated with those frequency levels (Figure 4.13). When compared back with the inundation frequency map (Figure 4.10), it is evident that the areas between 20% and 25% mainly include the drainage ditches connected to the channels. Tidal channels and drainage ditches are essential in understanding the control of delivering sediment-laden waters into the marsh system. Drainage ditches, in particular, have wide-ranging impacts on restoring marshes, such as influencing and changing vegetation patterns on-site by providing a resuspension sink for sediments to be retained (Corman et al., 2012; Pieterse et al., 2017). For these reasons, a fundamental principle of restoration in these marshes is restoring hydrology (Poirier et al., 2017).

A well-designed morphology influences the hydrology of a site, which in turn provides the substrate and the surface for new vegetation to come in and colonize. The establishment and retention of tidal salt marshes is highly dependent on the sediments supplied from the creeks, while sediment deposition rates decrease with increasing distance to tidal creek networks (Christiansen et al., 2000; Temmerman et al., 2003;

Poirier et al., 2017). Because there is such a strong relationship between plant zonation, sedimentation with inundation frequency, morphology and distance to tidal creeks, we can expect to see changes within those particular areas in future site assessments (Coco et al., 2013).

Due to technical limitations, the results of this work are too premature at this stage to give any indications about plant colonization. However, it is anticipated based on the preliminary pattern that exists, pioneering salt marsh plant occupation will likely first occur in the particular spaces where there are the muddy Vegetation and wet Vegetation classes, which is mostly in the western and north-eastern sections of the site (Figure 4.6). The Sentera sensor already delivered promising results, yet this type of analysis requires an upgraded RPA system and qualitatively higher multispectral sensor products, for more robust and reliable results. A more advanced sensor providing measurements within the near-infrared in a single or multiple individual bands, would deliver more spectral information yielding in clearer results of the surface patterns at a restoration site.

Chapter 5: Conclusions

The overall goal of this research was the development of guidelines for semi-automated classification to improve the acquisition and monitoring approaches to understand primary processes and relationships between a restoration site morphology, inundation frequency, and evolution of a tidal environment. This goal was realized by establishing a framework (Figure 3.1) and implementing relatively new image analysis methods with RPAS technology and Random Forest classifier. The classification results served then as an input for further analysis to assess and understand processes using the example of the Converse salt marsh restoration site.

The application of RPAS imagery with a multispectral sensor to monitor and quantify intertidal salt marsh restoration progress

Data analysis with RPAS imagery proved their advantages of high spatial and temporal resolution, flexibility in designing image survey missions, and cost- and time-efficiency when compared to other space or airborne platforms. However, the implementation of RPAS technology in further salt marsh restoration monitoring projects is constrained by the quality of the camera sensors due to the direct impact of image data quality to classification results. One of the challenges in working with RPAS imagery is its high sensitivity to environmental conditions. Atmospheric conditions such as cloud coverage, high contents of water vapour and aerosols in the atmosphere can have an impact on reflectance values acquired through the sensors mounted on the RPA and result in different reflectance values and have not been investigated to this date.

Moreover, a varying amount of noise in image values can be detected in the data due to lens distortions, systematic errors of data acquisition from the sensor, and camera sensitivity (Mafanya et al., 2018). Those impacts on the spectral response limit the quality and validity of the raw spectral data stored as digital numbers to an unknown degree (Minarik et al., 2019). Hence, the conversion of the raw digital numbers to reflectance values in physical units does provide the conditions required to analyze and compare data acquired at different times of the day or season for change detection. Furthermore, it offers the opportunity to make comparisons with alternative sensors or even different study sites. The process of radiometric calibration allows the spectral characterization of any given feature and can only be performed with technical information about the camera sensors, which were not available for this study after requesting this information from RPA manufacturer for the RGB stock-camera FC300X (Kelcey & Lucieer, 2012). The image taken of a calibration target in the field is also subject to changing exposure values from the camera and sensor and leads to processing errors in *Pix4D discovery*. In future missions, it is critical to take a close-up capture on a bright background of the target to avoid long exposures in order to execute a successful radiometric calibration.

The use of multispectral information was very crucial in separating classes within the pre- and post-breach imagery and should be incorporated in salt marsh restoration monitoring (Ozesmi & Bauer, 2002). The sensor quality of Sentera, however, created significant challenges and obstacles for a potentially better classification outcome in this study. Pande-Chhetri et al. (2017) made similar observations and concluded that RPAS provide a great potential in wetland mapping, however, solutions to improve image quality are necessary to improve classification performances. The difficulties in recognizing features on the multispectral imagery after the band-separation impacted the

positional accuracy. Furthermore, during the analysis steps for the classification, the actual pixel values of the near-infrared seemed to be defective and showed abnormal behaviours at certain features across the dataset. For future projects, a sensor upgrade with additional bands within the near-infrared is recommended.

The RPAS model DJI Phantom 3 Professional for environmental remote sensing purposes brought up some challenges with high sensitivity to weather variations, low battery durability, and small areal coverage. Newer models can cover larger areas with improved battery efficiency, and also include onboard differential GPS technology to reduce the number of GCPs necessary on the field. An upgraded model of the camera and sensor mounted on the RPAS will also decrease technological difficulties and consequently result in a greater efficiency necessary for a semi-automated framework.

The use of Object-based Image Analysis to analyze hyperspatial imagery

Object-based Image Analysis offers a promising classification method to map the very heterogenous cover types of tidal wetlands with the opportunity to integrate ecologically meaningful information on spatial context (Dronova, 2015). Although other studies reported successful implementation of OBIA in wetland classification (Gao & Mas, 2008; Kim et al., 2011), it is still unknown to what extent technical and conceptual constraints of this approach impact the success of this method and thus speaks for the development of solutions in future studies (Moffett & Gorelick, 2013; Dronova, 2015).

Segmentation algorithms are susceptible to variations in parameter settings, to the choice of hierarchical order, and also to the image criteria used for the analysis, such as the size of image and bit depth. This consequently results in a high degree of subjectivity exerted by the analyst, which is further amplified by the trial-and-error approach used in

the segmentation step (Meinel & Neubert, 2004). For future projects, it is highly recommended to implement an algorithm that calculates 'optimal' scale parameter (Drăguţ et al., 2010; Ming et al., 2015) or to conduct a more extensive study on ensemble methods testing the most optimal segmentation parameter settings for a given sensor platform and site characteristics. Furthermore, the shift from a single- to a multi-scale segmentation approach provides higher accuracies in the classification outcomes, especially for complex evolving landscapes such as in tidal wetland restoration sites (Kim et al., 2011).

Object-based image analysis relies heavily on expert knowledge of the applied software algorithms, image interpretation skills, technical knowledge of remotely sensed data, understanding of the site to be assessed, time invested in trial and error for parameter settings, and computer capacities (Corcoran et al., 2015). For the purpose of the highest degree of automation possible, the classification was applied on the single most suitable segmentation level and later improved with manual modifications. However, for future applications, it is recommended to conduct a step-wise classification on several levels (Kim et al., 2011). The first classification outcome should only distinguish major landcover classes, and the subsequent classifications should be based within each of the main landcover classes for further separation (Barker & King, 2012).

The accuracy of wetland classification outcomes and the separation of wetland classes from other landcover classes can often be improved by incorporating multi-temporal imagery (Ozesmi & Bauer, 2002). Future post-breach monitoring tasks can be aided by collecting several imageries throughout the season and merging the outcomes from each classification.

The application of OBIA allows a simple way of extracting classification results into a GIS environment in a vector file format. This reduced several steps of data transformation to be able to correlate classified information with other datasets for further analysis. The restoration progress could quickly be identified by calculating extent and creating graphs of the landcover classes and their coverage on site. The intersection of this information with an inundation frequency map resulted in a quantitative assessment of developments and processes on the restoration trajectory at Converse. There is more potential for further analysis with the classification results by applying statistical measures to correlate landcover class, elevation, inundation frequency and duration would provide an even better understanding of the site. The associated feature values of the classified image objects can also provide further information to incorporate into the analysis and can help to create a base for a site-specific spectral library to support continuing monitoring efforts at Converse by the means of remote sensing.

Quantifying and correlating class area with hydrological analysis to interpret classification results and understand implications for the evolving landscape

The intersection of frequency inundation and class distribution is a fast solution to assess an evolving tidal marsh quantitatively and get a better idea of the coinciding conditions at a restoration site. In continuation of the monitoring process at Converse, it is recommended to implement information of the hydroperiod (length of time a particular location is covered in water) in addition to the frequency inundation, and statistically correlate this information with suspended sediment concentrations and elevation across the study site. The results of the statistical analysis considering the aforementioned factors

will give further insight into ongoing processes and will help predict potential development paths in a more reliable way.

Within the scope of this research, the frequency inundations were calculated based on long term predictions considering only the high tide values and does not represent a continuous inundation throughout a whole tidal cycle. The water levels of the predicted high tides were transformed to the local datum (CGVD13) by using the calculated offset value of 6.69 m. This value was based on a relative short-term recording (33 days) in October 2017 and does not necessarily provide the optimal offset value applicable to transform datums throughout the whole year. In particular, since the short-term deployment recorded tide levels in the fall, which is the season of the highest tides of a year. For repeated analysis, it is recommended to repeat the frequency inundation calculations based on an offset value calculated from long-term tidal recordings of water levels optimally measuring different seasons of a site.

Future directions and recommendations

For future applications, to be able to talk about a framework and a semi-automated classification process, certain topics need to get more attention before successfully implementing them; for example sample design, sample selection and size (Foody, 2002; Rougier et al., 2016), feature selection (Laliberte et al., 2012), classification technique (Maxwell et al., 2018), accuracy assessment (Stehman & Wickham, 2011; Ye et al., 2018).

OBIA is a strong method to analyze hyper-spatial data for complex environmental applications and has already proven to be successful in various other studies (Laliberte et al., 2010; Pande-Chhetri et al., 2017). However, in order to establish a reliable framework

for restoration monitoring, the individual steps of the framework have to be assessed and standardized with the help of case studies. Finally, more research has to be conducted on the choice of a proper accuracy assessment method for object-based image analysis due to the fact that many factors may influence the accuracy of OBIA results, such as the quality of the segmentation, the choice of features for the classification, and the incorporation of errors due to the analysts themselves. All these factors need to be assessed beyond simple reference point statistics and currently, many publications differ in their approaches of covering before named factors (Ye et al., 2018).

Based on this thesis, a series of key recommendations for future deployments were made (Table 5.1).

Table 5.1: Key recommendations summarizing the considerations for future salt marsh restoration site assessment and monitoring projects gained of the results of this research.

Concepts & Applications	**Key Recommendations**
OBIA	• Should be applied when using very high resolution RPAS imagery in highly heterogenous environments • Should be performed with a multi-scale analysis for general site-assessment • Segmentation step should use algorithms to extract optimal scale parameter for increased objectivity of the process • Consider other environments to perform object-based image analysis outside of *eCognition*, such as R
Pixel-based approach	• Should be applied for change detection analysis
RPAS model	• Should have PPK capability to assure higher positional accuracies with fewer GCP targets • For absolute reflectance values, RPAS camera specifics (band width and sensitivity) should be known

Camera and sensor model	• High quality multispectral sensor critical • Choose sensors with a larger the number of bands and narrower band widths • Should have spectral sensitivity factor disclosed in order to apply radiometric correction • Deploy cameras with larger Instantaneous Field of View (IFOV) to cover more ground areas in less time
Machine Learning Algorithm	• Use ML classifiers for image analysis • Random Forest is very recommended for the intertidal landscape at Converse using RPAS imagery and OBIA • Support Vector Machine has great potential; however, the analyst should have a profound understanding of different parameter settings and their impact on the end results • The creation of a spectral signature library for intertidal wetland classes is recommended in order to further improve classifier in repeated site assessments • Different packages and modules available in R and Python may be used to execute machine learning algorithms
Landscape Interpretation	• Frequency Inundation calculations should be performed on a higher timescale for long-term periods • Hydroperiod is important to incorporate and should be considered in the analysis • Elevation and suspended sediment concentrations are also critical for salt marsh establishment and should be considered in statistical correlations with other elements

On the condition of implementing a multi-scale analysis approach, Object-based Image Analysis is an effective method and will provide great potential for restoration site assessment when working within widely heterogenous landscapes, such as tidal wetlands, and when using very high resolution RPAS imagery. The method of pixel-based image analysis was not tested within the scope of this research to allow direct comparison with the object-based approach, which could have provided more suggestive conclusions in this context. However, when conducting a follow-up project at Converse, it is suggested to use a combined approach by first classifying imagery using the object-based approach

and afterwards re-classifying areas of individual landcover classes by using the pixel-based approach within the object for change detection.

The implementation of machine learning algorithms is highly recommended and should be tested in broader scale, provided that high-grad multispectral sensors are available. Lastly, for the assessment and interpretation of dominant drivers on-site, more factors influencing a tidal salt marsh establishment need to be considered in correlation to one another in order to draw rigorous conclusions on the status of the restoration success.

References

Aber, J. S., Marzolff, I., & Ries, J. B. (2010). *Small-Format Aerial Photography: Principles, Techniques and Geoscience Applications*. Amsterdam, The Netherlands: Elsevier.

Alföldi, T. T. (1975). *The use of satellite imagery for an inventory of coastal resources in the Atlantic Provinces*. Department of Energy, Mines and Resources. Ottawa: Canada Centre for Remote Sensing.

Amani, M., Salehi, B., Mahdavi, S., & Brisco, B. (2018). Spectral analysis of wetlands using multi-source optical satellite imagery. *ISPRS Journal of Photogrammetry and Remote Sensing, 144*, 119-136. doi:10.1016/j.isprsjprs.2018.07.005

Amani, M., Salehi, B., Mahdavi, S., & Granger, J. (2017). Spectral Analysis of Wetlands in Newfoundland Using Sentinel 2A and Landsat 8 Imagery. *IGTF 2017 - Imaging & Geospatial Technology Forum* (p. 8). Baltimore, Maryland: ASPRS Annual Conference.

Anderson, K., & Gaston, K. J. (2013). Lightweight unmanned aerial vehicles will revolutionize spatial ecology. *Frontiers in Ecology and the Environment, 11*(3), 138-146. doi:10.1890/120150

Antoine, C., Long, B., & Archambault, P. (2010). Salt-marsh characterization, zonation assessment and mapping through a dual-wavelength LiDAR. *Remote Sensing of Environment, 114*(3), 520-530. doi:10.1016/j.rse.2009.10.011

Artigas, F. J., & Yang, J. (2006). Spectral discrimination of marsh vegetation types in the New Jersey Meadowlands, USA. *Wetlands, 26*(1), 271-277. doi:10.1672/0277-5212(2006)26[271:SDOMVT]2.0.CO;2

Arvor, D., Durieux, L., Andrés, S., & Laporte, M.-A. (2013). Advances in Geographic Object-Based Image Analysis with ontologies: A review of main contributions and limitations from a remote sensing perspective. *ISPRS Journal of Photogrammetry and Remote Sensing, 82*, 125-137. doi:10.1016/j.isprsjprs.2013.05.003

Barker, R., & King, D. J. (2012). Blanding's Turtle (Emydoidea blandingii) Potential Habitat Mapping Using Aerial Orthophotographic Imagery and Object Based Classification. *Remote Sensing, 4*(1), 194-219. doi:10.3390/rs4010194

Bartlett, D. S., & Klemas, V. (1980). Quantitative Assessment of Tidal Wetlands Using Remote Sensing. *Environmental Management, 4*(4), 337-345. doi:10.1007/BF01869426

Belluco, E., Camuffo, M., Ferrari, S., Modenese, L., Silvestri, S., Marani, A., & Marani, M. (2006). Mapping salt-marsh vegetation by multispectral and hyperspectral remote sensing. *Remote Sensing of Environment, 105*(1), 54-67. doi:10.1016/j.rse.2006.06.006

Benz, U. C., Hofmann, P., Willhauck, G., Lingenfelder, I., & Heynen, M. (2004). Multi-resolution, object-oriented fuzzy analysis of remote sensing data for GIS-ready information. *ISPRS Journal of Photogrammetry and Remote Sensing, 58*(3-4), 239-258. doi:10.1016/j.isprsjprs.2003.10.002

Blaschke, T., Hay, G. J., Kelly, M., Lang, S., Hofmann, P., Addink, E., Feitosa, R. Q., van der Meer, F., van der Werff, H., van Coillie, F., Tiede, D. (2014). Geographic Object-Based Image Analysis – Towards a new paradigm. *ISPRS Journal of Photogrammetry and Remote Sensing, 87*, 180-191. doi: 10.1016/j.isprsjprs.2013.09.014.

Bowron, T. M., Graham, J., Ellis, K., McFadden, C., Poirier, E., & van Proosdij, D. (2019). *Managed Realignment & Restoration of the Converse Salt Marsh (NS044) - 2018-19 Summary Report*. Report No. 14, CB Wetlands & Environmental Specialists, A Report for: Department of Fisheries and Oceans & Nova Scotia Department of Agriculture, Halifax.

Bowron, T. M., Neatt, N. C., Graham, J. M., van Proosdij, D., Lundholm, J., & Lemieux, B. (2013). *Post-Restoration Monitoring (Year 7) of the Cheverie Creek Salt Marsh Restoration Project*. CB Wetlands & Environmental Environmental Specialists, A Report for: Nova Scotia Department of Transportation and Infrastructure Renewal.

Bowron, T. M., Neatt, N., Graham, J., van Proosdij, D., Lundholm, J. T., & Lemieux, B. (2015). *Post-Restoration Monitoring (Year 5) of the St. Croix River High Salt Marsh & Tidal Wetland Restoration Project*. Report No. 41, A Report for: Nova Scotia Department of Transportation and Infrastructure Renewal, Halifax, NS. doi:10.13140/RG.2.2.11132.33921

Bowron, T. M., Neatt, N., van Proosdij, D., & Lundholm, J. (2012). Salt Marsh Tidal Restoration in Canada's Maritime Provinces. In C. T. Roman, & D. M. Burdick, *Tidal Marsh Restoration - A Synthesis of Science and Management*. Washington, DC: Island Press.

Breiman, L. (2001). Random Forests. *Machine Learning, 45*(1), 5-32. doi:10.1023/A:1010933404324

Burnett, C., & Blaschke, T. (2003). A multi-scale segmentation/object relationship modelling methodology for landscape analysis. *Ecological Modelling, 168*(3), 233-249. doi:10.1016/S0304-3800(03)00139-X

Byers, S. E., & Chmura, G. L. (2007). Salt Marsh Vegetation Recovery on the Bay of Fundy. *Estuaries and Coasts, 30*(5), 869-877. Retrieved from http://www.jstor.org/stable/27654722

Canada Centre for Remote Sensing. (2015, 11 19). *Natural Resources Canada*. Retrieved 11 13, 2019, from Remote Sensing Tutorials: https://www.nrcan.gc.ca/maps-tools-publications/satellite-imagery-air-photos/tutorial-fundamentals-remote-sensing/9309

Canadian Aviation Regulations. (Last amended on 2019-05-15). *Government of Canada*. Retrieved from Justice Laws Website: https://laws-lois.justice.gc.ca/eng/regulations/SOR-96-433/FullText.html#s-900.01

Carlotto, M. J. (2009). Effect of errors in ground truth on classification accuracy. *International Journal of Remote Sensing, 30*(18), 4831-4849. doi:10.1080/01431160802672864

Chassereau, J. E., Bell, J. M., & Torres, R. (2011). A comparison of GPS and lidar salt marsh DEMs. *Earth Surface Processes and Landforms, 36*(13), 1770-1775. doi:10.1002/esp.2199

Christiansen, T., Wiberg, P. L., & Milligan, T. G. (2000). Flow and Sediment Transport on a Tidal Salt Marsh Surface. Estuarine, *Coastal and Shelf Science, 50*, 315-331. doi:10.1006/ecss.2000.0548

Coco, G., Zhou, Z., van Maanen, B., Olabarrieta, M., Tinoco, R., & Townend, I. (2013). Morphodynamics of tidal networks: Advances and challenges. *Marine Geology, 346*, 1-16. doi:10.1016/j.margeo.2013.08.005

Colomina, I., & Molina, P. (2014). Unmanned aerial systems for photogrammetry and remote sensing: A review. *ISPRS Journal of Photogrammetry and Remote Sensing, 92*, 79-97. doi:10.1016/j.isprsjprs.2014.02.013

Congalton, R. G. (1991). A Review of Assessing the Accuracy of Classifications of Remotely Sensed Data. *Remote Sensing of Environment, 37*(1), 35-46. doi:10.1016/0034-4257(91)90048-B

Connor, R. F., Chmura, G. L., & Beecher, B. C. (2001). Carbon accumulation in Bay of Fundy salt marshes: Implications for restoration of reclaimed marshes. *Global Biochemical Cycles, 15*(4), 943-954. doi:10.1029/2000GB001346

Corcoran, J., Knight, J., Pelletier, K., Rampi, L., & Wang, Y. (2015). The Effects of Point or Polygon Based Training Data on RandomForest Classification Accuracy of Wetlands. *Remote Sensing, 7*(4), 4002-4025. doi:10.3390/rs70404002

Corman, S. S., Roman, C. T., King, J. W., & Appleby, P. G. (2012). Salt Marsh Mosquito-Control Ditches: Sedimentation, Landscape Change, and Restoration Implications. *Journal of Coastal Research, 28*(4), 874-880. doi:10.2112/JCOASTRES-D-11-00012.1

Correll, M. D., Hantson, W., Hodgman, T. P., Cline, B. B., Elphick, C. S., Shriver, G. W., . . . Olsen, B. J. (2019). Fine-Scale Mapping of Coastal Plant Communities in the Northeastern USA. *Wetlands, 39*, 17–28. doi:10.1007/s13157-018-1028-3

Crooks, S., Schutten, J., Sheern, G. D., Pye, K., & Davy, A. J. (2002). Drainage and Elevation as Factors in the Restoration of Salt Marsh in Britain. *Restoration Ecology, 10*(3), 591 -602. doi:10.1046/j.1526-100X.2002.t01-1-02036.x

Daigle Enviro, R. J. (2017). *Updated Sea-Level Rise and Flooding Estimates for New Brunswick Coastal Sections: Based on IPCC 5th Assessment Report*. Climate Change Secreta, New Brunswick Department of Environment and Local Government, Moncton.

DDST. (2020). *Dykeland Decision Support Tool*. A geomatics based database management system and decision support tool developed at MP_SpARC (SMU) with the NS Department of Agriculture. Halifax, Nova Scotia, Canada.

de Jong, S. M., & van der Meer, F. D. (2004). *Remote Sensing Image Analysis: Including the Spatial Domain*. Dordrecht, The Netherlands: Kluwer Academic Publisher. doi:ISBN 1-4020-2559-9

Definiens AG. (n.d.). Developer: Reference Book. Munich, Germany.

Delacourt, C., Allemand, P., Jaud, M., Grandjean, P., Deschamps, A., Ammann, J., . . . Suanez, S. (2009). DRELIO: An Unmanned Helicopter for Imaging Coastal Areas. *Journal of Coastal Research, II*(Special Issue No. 56), 1489-1493. Retrieved from https://www.jstor.org/stable/25738037

Desplanque, C., & Mossman, D. J. (2004). Tides and their seminal impact on the geology, geography, history, and socio-economics of the Bay of Fundy, eastern Canada. *Atlantic Geology, 40*(1), 65. doi:10.4138/729

DJI. (n.d.). *DJI*. Retrieved from Phantom 3 Professional Specs: https://www.dji.com/ca/phantom-3-pro

Drăguţ, L., Tiede, D., & Levick, S. R. (2010). ESP: a tool to estimate scale parameter for multiresolution image segmentation of remotely sensed data. *International Journal of Geographical Information Science, 24*(6), 859-871. doi:10.1080/13658810903174803

Dronova, I. (2015). Object-Based Image Analysis in Wetland Research: A Review. *Remote Sensing, 7*, 6380-6413. doi:10.3390/rs70506380

Duarte, C. M., Losada, I. J., Hendriks, I. E., Mazarrasa, I., & Marbà, N. (2013). The role of coastal plant communities for climate change mitigation and adaptation. *Nature Climate Change, 3*, 961-968. doi:10.1038/NCLIMATE1970

Environment and Natural Resources Canada. (2019, 10 22). *Government of Canada*. Retrieved 01 13, 2020, from Climate Normals & Averages: https://climate.weather.gc.ca/climate_normals/results_1981_2010_e.html?searchType=stnProv&lstProvince=NS&txtCentralLatMin=0&txtCentralLatSec=0&txtCentralLongMin=0&txtCentralLongSec=0&stnID=6414&dispBack=0

European Global Navigation Satellite Systems Agency. (2019, June 26). Retrieved from What is GNSS?: https://www.gsa.europa.eu/european-gnss/what-gnss

Flanders, D., Hall-Beyer, M., & Pereverzoff, J. (2003). Preliminary evaluation of eCognition object-based software for cut block delineation and feature extraction. *Canadian Journal of Remote Sensing, 29*(4), 441-452. doi:https://doi.org/10.5589/m03-006

Foody, G. M. (2002). Status of land cover classification accuracy assessment. *Remote Sensing of Environment, 80*, 185-201. doi:10.1016/S0034-4257(01)00295-4

French, C. E., French, J. R., Clifford, N. J., & Watson, C. J. (2000). Sedimentation-erosion dynamics of abandoned reclamations: the role of waves and tides. *Continental Shelf Research, 20*(12-13), 1711-1733. doi:10.1016/S0278-4343(00)00044-3

French, P. W. (2006). Managed realignment - The developing story of a comparatively new approach to soft engineering. *Estuarine, Coastal and Shelf Science, 67*(3), 409-423. doi:10.1016/j.ecss.2005.11.035

Gallant, A. L. (2015). The Challenges of Remote Monitoring of Wetlands. *Remote Sensing, 7*(8), 10938-10950. doi:10.3390/rs70810938

Gao, Y., & Mas, J. F. (2008). A Comparison of the Performance of Pixel Based and Object Based Classifications over Images with Various Spatial Resolutions. *Online Journal of Earth Sciences, 2*(1), 27-35. Retrieved from http://people.ucalgary.ca/~gjhay/geobia/Proceedings/Sessions/Session1/6589_Y_Gao_Proc_pap.pdf

Gao, Z. G., & Zhang, L. Q. (2006). Multi-seasonal spectral characteristics analysis of coastal salt marsh vegetation in Shanghai, China. *Estuarine, Coastal and Shelf Science, 69*(1-2), 217-224. doi:10.1016/j.ecss.2006.04.016

Gilmore, M. S., Wilson, E. H., Barrett, N., Civco, D. L., Prisloe, S., Hurd, J. D., & Chadwick, C. (2008). Integrating multi-temporal spectral and structural information to map wetland vegetation in a lower Connecticut River tidal marsh. *Remote Sensing of Environment, 112*(11), 4048-4060. doi:10.1016/j.rse.2008.05.020

GMV. (2011). European Space Agency - Navipedia. Retrieved from Real Time Kinematics: https://gssc.esa.int/navipedia/index.php/Real_Time_Kinematics

Gonçalves, J. A., & Henriques, R. (2015). UAV photogrammetry for topographic monitoring of coastal areas. *ISPRS Journal of Photogrammetry and Remote Sensing, 104*, 101-111. doi:10.1016/j.isprsjprs.2015.02.009

Government of Nova Scotia. (2009). *Environmental Goals and Sustainable Prosperity Act - Annual Progress Report*. Retrieved from https://novascotia.ca/nse/egspa/docs/EGSPA.2009.Annual.Report.pdf

Government of Nova Scotia. (2011). *Nova Scotia Wetland Conservancy Policy*. Nova Scotia: Author.

Green, D. R., Hagon, J. J., Gómez, C., & Gregory, B. J. (2019). Chapter 21 - Using Low-Cost UAVs for Environmental Monitoring, Mapping, and Modelling: Examples From the Coastal Zone. In R. R. Krishnamurthy, M. P. Jonathan, S. Srinivasalu, & B. Glaeser (Eds.), *Coastal Management - Global Challenges and Innovations* (pp. 465-501). Academic Press. doi:10.1016/B978-0-12-810473-6.00022-4

Grenier, M., Labrecque, S., & Benoit, M. (2008). Accuracy Assessment Method for Wetland Object-based Classification. *Semantic Scholar*. Retrieved from https://www.semanticscholar.org/paper/ACCURACY-ASSESSMENT-METHOD-FOR-WETLAND-OBJECT-BASED-Grenier-Labrecque/5176d9026d5951d235974a998b043cff64398e3a

Guo, M., Li, J., Sheng, C., Xu, J., & Wu, L. (2017). A Review of Wetland Remote Sensing. *Sensors, 17*(4), 36. doi:10.3390/s17040777

Hansen, M., Dubayah, R., & DeFries, R. (1996). Classification Trees: An Alternative to Traditional Land Cover Classifiers. *International Journal of Remote Sensing, 17*(5), 1075–1081. doi:10.1080/01431169608949069

Hardisky, M. A., Gross, M. F., & Klemas, V. (1986). Remote Sensing of Coastal Wetlands. *American Institute of Biological Sciences, 36*(7), 453-460. Retrieved from https://www.jstor.org/stable/1310341

Harken, J., & Sugumaran, R. (2005). Classification of Iowa wetlands using an airborne hyperspectral image: A comparison of the spectral angle mapper classifier and an object-oriented approach. *Canadian Journal of Remote Sensing, 31*(2), 167-174. doi:10.5589/m05-003

Hassan, N., Hamid, J. R., Adnan, N. A., & Jaafar, M. (2014). Delineation of wetland areas from high resolution WorldView-2 data by object-based method. *8th International Symposium of the Digital Earth (ISDE8). 18*, p. 7. IOP Conference Series: Earth and Environmental Science. doi:10.1088/1755-1315/18/1/012017

Hay, G. J., Castilla, G., Wulder, M. A., & Ruiz, J. R. (2005). An automated object-based approach for multiscale image segmentation of forest scenes. *International Journal of Applied Earth Observation and Geoinformation, 7*(4), 339-359. doi:10.1016/j.jag.2005.06.005

Hodgson, M. E., Jensen, J. R., Tullis, J. A., Riordan, K. D., & Archer, C. M. (2003). Synergistic use of Lidar and color aerial photography for mapping urban parcel imperviousness. *Photogrammetric Engineering & Remote Sensing, 69*(9), 973–980. doi:https://doi.org/10.14358/PERS.69.9.973

Huang, C., Davis, L. S., & Townshend, J. R. (2002). An Assessment of Support Vector Machines for Land Cover Classification. *International Journal of Remote Sensing, 23*(4), 725–749. doi:10.1080/01431160110040323

Hugenholtz, C. H., Moorman, B. J., Riddell, K., & Whitehead, K. (2012). Small unmanned aircraft systems for remote sensing and Earth science research. *EOS, 93*(25), 236. doi:10.1029/2012EO250005

ICAO. (2011). *Unmanned Aircraft Systems (UAS) - Circular 328*. Montreal, Quebec, Canada: International Civil Aviation Organization.

IPCC. (2013). Summary for policymakers. In T. F. Stocker, D. Qin, G.-K. Plattner, M. Tignor, S. K. Allen, J. Boschung, . . . P. M. Midgley (Eds.), *Climate change 2013: The physical science basis. Contribution of Working Group I to the Fifth Assessment Report of the Intergovernmental Panel on Climate Change* (p. 1535). Cambridge, United Kingdom and New York, NY, USA: Cambridge University Press.

Jahncke, R., Brigitte, L., Peter, B., & Armand, L. (2018). Mapping wetlands in Nova Scotia with multi-beam RADARSAT-2 Polarimetric SAR, optical satellite imagery, and Lidar data. *International Journal of Applied Earth Observation and Geoinformation, 68*, 139-156. doi:10.1016/j.jag.2018.01.012

Jeong, E., Park, J.-Y., & Hwang, C.-S. (2018). Assessment of UAV Photogrammetric Mapping Accuracy in the Beach Environment. *Journal of Coastal Research, SI*(85), 176-180. doi:10.2112/SI85-036.1

Kalacska, M., Chmura, G. L., Lucanus, O., Bérubé, D., & Arroyo-Mora, J. P. (2017). Structure from motion will revolutionize analyses of tidal wetland landscapes. *Remote Sensing of Environment, 199*, 14-24. doi:10.1016/j.rse.2017.06.023

Kavzoglu, T., Erdemir, M. Y., & Tonbul, H. (2016). A region-based multi-scale approach for object-based image analysis. *ISPRS - International Archives of the Photogrammetry, Remote Sensing and Spatial Information Sciences, Commission VII*(WG VII/4), 241-247. doi:10.5194/isprs-archives-XLI-B7-241-2016

Kelcey, J., & Lucieer, A. (2012). Sensor Correction of a 6-Band Multispectral Imaging Sensor for UAV Remote Sensing. *Remote Sensing, 4*, 1462-1493. doi:10.3390/rs4051462

Kelcey, J., & Lucieer, A. (2012). Sensor Correction of a 6-Band Multispectral Imaging Sensor for UAV Remote Sensing. *Remote Sensing, 4*, 1462-1493. doi:10.3390/rs4051462

Kim, M., Madden, M., & Warner, T. (2008). Estimation of optimal image object size for the segmentation of forest stands with multispectral IKONOS imagery. In T. Blaschke, S. Lang, & G. J. Hay, *Object-Based Image Analysis* (pp. 291-307). Berlin, Heidelberg: Springer. doi:10.1007/978-3-540-77058-9_16

Kim, M., Warner, T. A., Madden, M., & Atkinson, D. (2011). Multi-scale GEOBIA with very high spatial resolution digital aerial imagery: scale, texture and image objects. *International Journal of Remote Sensing, 32*(10), 2825-2850. doi:10.1080/01431161003745608

Klemas, V. (2011). Remote Sensing of Wetlands: Case Studies Comparing Practical Techniques. *Journal of Coastal Research, 27*(3), 418-427. Retrieved from https://www.jstor.org/stable/29783262

Klemas, V. (2015). Coastal and Environmental Remote Sensing from Unmanned Aerial Vehicles: An Overview. *Journal of Coastal Research, 31*(5), 1260–1267. doi:10.2112/JCOASTRES-D-15-00005.1

Klötzli, F., & Grootjans, A. P. (2001). Restoration of Natural and Semi-Natural Wetland Systems in Central Europe: Progress and Predictability of Developments. *Restoration Ecology, 9*(2), 209-219. doi:10.1046/j.1526-100x.2001.009002209.x

Laba, M., Blair, B., Downs, R., Monger, B., Philpot, W., Smith, S., . . . Baveye, P. C. (2010). Use of textural measurements to map invasive wetland plants in the Hudson River National Estuarine Research Reserve with IKONOS satellite imagery. *Remote Sensing of Environment, 114*(4), 876-886. doi:10.1016/j.rse.2009.12.002

Laliberte, A. S., & Rango, A. (2009). Texture and Scale in Object-Based Analysis of Subdecimeter Resolution Unmanned Aerial Vehicle (UAV) Imagery. *IEEE Transactions on Geoscience and Remote Sensing, 47*(3), 761-770. doi:10.1109/TGRS.2008.2009355

Laliberte, A. S., Browning, D. M., & Rango, A. (2012). A comparison of three feature selection methods for object-based classification of sub-decimeter resolution UltraCam-L imagery. *International Journal of Applied Earth Observation and Geoinformation, 15*, 70-78. doi:10.1016/j.jag.2011.05.011

Laliberte, A. S., Herrick, J. E., Rango, A., & Winters, C. (2010). Aquisition, Orthorectification, and Object-based Classification of Unmanned Aerial Vehicle (UAV) Imagery for Rangeland Monitoring. *Photogrammetric Engineering & Remote Sensing, 76*(6), 661–672. doi:10.14358/PERS.76.6.661

Lang, S. (2008). Object-based image analysis for remote sensing applications: modeling reality - dealing with complexity. In T. Blaschke, S. Lang, & G. J. Hay (Eds.), *Object-Based Image Analysis: Spatial Concepts for Knowledge-Driven Remote Sensing Applications* (p. 817). Berlin Heidelberg: Springer Verlag.

Lang, S., Blaschke, T., & Schoepfer, E. (2006). Bridging Remote Sensing and GIS - What are the main supportive pillars? *1st International Conference on Object-based Image Analysis (OBIA 2006)* (p. 6). Salzburg, Austria: International Society for Photogrammetry and Remote Sensing Archives.

Lavender, S., & Lavender, A. (2016). *Practical Handbook of Remote Sensing*. Boca Raton London New York: CRC Press.

Lawrence, R. L., & Moran, C. J. (2015). The AmericaView Classification Methods Accuracy Project: A Rigorous Approach for Model Selection. *Remote Sensing of Environment, 170*, 115–120. doi:10.1016/j.rse.2015.09.008

Li, M., Zang, S., Zhang, B., Li, S., & Wu, C. (2014). A Review of Remote Sensing Image Classification Techniques: the Role of Spatio-contextual Information. *European Journal of Remote Sensing, 47*(1), 389-411. doi:10.5721/EuJRS20144723

Liu, D., & Xia, F. (2010). Assessing object-based classification: advantages and limitations. *Remote Sensing Letters, 1*(4), 187-194. doi:10.1080/01431161003743173

Long, N., Millescamps, B., Guillot, B., Pouget, F., & Bertin, X. (2016). Monitoring the Topography of a Dynamic Tidal Inlet Using UAV Imagery. *Remote Sensing, 8*(5), 387. doi:10.3390/rs8050387

Ma, L., Cheng, L., Li, M., Liu, Y., & Ma, X. (2015). Training set size, scale, and features in Geographic Object-Based Image Analysis of very high resolution unmanned aerial vehicle imagery. *ISPRS Journal of Photogrammetry and Remote Sensing, 102*, 14–27. doi:10.1016/j.isprsjprs.2014.12.026

Ma, L., Li, M., Ma, X., Cheng, L., Du, P., & Liu, Y. (2017). A review of supervised object-based land-cover image classification. *ISPRS Journal of Photogrammetry and Remote Sensing, 130*, 277-293. doi:10.1016/j.isprsjprs.2017.06.001

Mafanya, M., Tsele, P., Botai, J. O., Manyama, P., Chirima, G. J., & Monate, T. (2018). Radiometric calibration framework for ultra-high-resolution UAV-derived orthomosaics for large-scale mapping of invasive alien plants in semi-arid woodlands: Harrisia pomanensis as a case study. *International Journal of Remote Sensing, 39*(15-16), 5119-5140. doi:10.1080/01431161.2018.1490503

Mahdavi, S., Salehi, B., Granger, J., Amani, M., Brisco, B., & Huang, W. (2017). Remote sensing for wetland classification: a comprehensive review. *GIScience & Remote Sensing, 55*(5), 623-658. doi:10.1080/15481603.2017.1419602

Maxwell, A. E., Warner, T. A., & Fang, F. (2018). Implementation of machine-learning classification in remote sensing: an applied view. *International Journal of Remote Sensing, 39*(9), 2784–2817. doi:10.1080/01431161.2018.1433343

McCoy, R. M. (2005). *Field Methods in Remote Sensing*. New York, NY: The Guilford Press.

Meinel, G., & Neubert, M. (2004). A Comparison Of Segmentation Programs For High Resolution Remote Sensing Data. *International Archives of Photogrammetry, Remote Sensing and Spatial Information Sciences, Commission IV Papers, Vol. XXXV*, Part B4, XXth ISPRS Congress, pp. 1097-1102. Istanbul. Retrieved 07 05, 2019, from https://www.isprs.org/proceedings/XXXV/congress/comm4/comm4.aspx

Mesner, N., & Ostir, K. (2014). Investigating the impact of spatial and spectral resolution of satellite images on segmentation quality. *Journal of Applied Remote Sensing, 8*(1), 083696. doi:10.1117/1.JRS.8.083696

Millard, K., Redden, A. M., Webster, T., & Stewart, H. (2013). Use of GIS and high resolution LiDAR in salt marsh restoration site suitability assessments in the upper Bay of Fundy, Canada. *Wetlands Ecology and Management, 21*(4), 243-262. doi:10.1007/s11273-013-9303-9

Millard, K. & Richardson, M. (2015). On the Importance of Training Data Sample Selection in Random Forest Image Classification: A Case Study in Peatland Ecosystem Mapping. *Remote Sensing, 7*, 8489-8515. doi:10.3390/rs70708489

Milligan, T. G., Hill, P. S., & Law, B. A. (2007). Flocculation and the loss of sediment from the Po River plume. *Continental Shelf Research, 27*(3-4), 309-321. doi:10.1016/j.csr.2006.11.008

Minarik, R., Langhammer, J., & Hanuš, J. (2019). *Remote Sensing, 11*(20), 2428. doi:10.3390/rs11202428

Ming, D., Li, J., Wang, J., & Zhang, M. (2015). Scale parameter selection by spatial statistics for GeOBIA: Using mean-shift based multi-scale segmentation as an example. *ISPRS Journal of Photogrammetry and Remote Sensing, 106*, 28-41. doi:10.1016/j.isprsjprs.2015.04.010

Mitchell, M., & Bilkovic, D. M. (2019). Embracing dynamic design for climate-resilient living shorelines. *Journal of Applied Ecology, 56*, 1099–1105. doi:10.1111/1365-2664.13371

Mitsch, W. J., & Gosselink, J. G. (2015). *Wetlands* (Fifth ed.). Hoboken, NJ: John Wiley and Sons.

Moffett, K. B., & Gorelick, S. M. (2013). Distinguishing wetland vegetation and channel features with object-based image segmentation. *International Journal of Remote Sensing, 34*(4), 1332-1354. doi:10.1080/01431161.2012.718463

Montané, J. M., & Torres, R. (2006). Accuracy Assessment of Lidar Saltmarsh Topographic Data Using RTK GPS. *Photogrammetric Engineering & Remote Sensing, 72*(8), 961–967. doi:10.14358/PERS.72.8.961

Mowrer, T. H., & Congalton, R. G. (2000). Quantifying spatial uncertainty in natural resources theory and applications for GIS and remote sensing. *International Symposium on Spatial Accuracy Assessment in Natural Resources and Environmental Sciences*. Fort Collins, Colo.

Mui, A., He, Y., & Weng, Q. (2015). An object-based approach to delineate wetlands across landscapes of varied disturbance with high spatial resolution satellite imagery. *ISPRS Journal of Photogrammetry and Remote Sensing, 109*, 30-46. doi:10.1016/j.isprsjprs.2015.08.005

Munday Jr., J. C., & Alföldi, T. T. (1979). LANDSAT test of diffuse reflectance models for aquatic suspended solids measurement. *Remote Sensing of Environment, 8*(2), 169-183. doi:10.1016/0034-4257(79)90015-4

NASA. (2013, March). The Electromagnetic Spectrum. Retrieved from National Aeronautics and Space Administration - Goddard Space Flight Center: https://imagine.gsfc.nasa.gov/science/toolbox/emspectrum1.html

O'Laughlin, C., van Proosdij, D., & Milligan, T. G. (2014). Flocculation and sediment deposition in a hypertidal creek. *Continental Shelf Research, 82*, 72-84. doi:10.1016/j.csr.2014.02.012

Ollerhead, J., Davidson-Arnott, R. G., & Scott, A. (2005). Cycles of saltmarsh extension and contraction, Cumberland Basin, Bay of Fundy, Canada. In V. M. Rossello, Sanjaume, Eulalia, Mateu, & Joan (Eds.), *Geomorphologia Littoral* (pp. 293-305). Publicacions Universitat de Valencia. Retrieved from https://www.researchgate.net/publication/233986222_Cycles_of_saltmarsh_extension_and_contraction_Cumberland_Basin_Bay_of_Fundy_Canada

Ouyang, Z.-T., Zhang, M.-Q., Xie, X., Shen, Q., Guo, H.-Q., & Zhao, B. (2011). A comparison of pixel-based and object-oriented approaches to VHR imagery for mapping saltmarsh plants. *Ecological Informatics, 6*(2), 136-146. doi:10.1016/j.ecoinf.2011.01.002

Ozesmi, S. L., & Bauer, M. E. (2002). Satellite remote sensing of wetlands. *Wetlands Ecology and Management, 10*(5), 381-402. doi:10.1023/A:1020908432489

Pal, M. (2005). Random Forest Classifier for Remote Sensing Classification. *International Journal of Remote Sensing, 26*(1), 217-222. doi:10.1080/01431160412331269698

Pal, M., & Mather, P. M. (2003). An assessment of the effectiveness of decision tree methods for land cover classification. *Remote Sensing of Environment, 86*(4), 554–565. doi:10.1016/S0034-4257(03)00132-9

Pande-Chhetri, R., Abd-Elrahman, A., Liu, T., Morton, J., & Wilhelm, V. L. (2017). Object-based classificatin of wetland vegetation using very high-resolution unmanned air system imagery. *European Journal of Remote Sensing, 50*(1), 564–576. doi:10.1080/22797254.2017.1373602

Pieterse, A., Puleo, J. A., McKenna, T. E., & Figlus, J. (2017). In situ measurements of shear stress, erosion and deposition in man-made tidal channels within a tidal saltmarsh. Estuarine, *Coastal and Shelf Science, 192*, 29-41. doi:10.1016/j.ecss.2017.04.028

Pix4D. (2017, Dec. 14). Pix4Dmapper Manual. Retrieved https://support.pix4d.com/hc/en-us/articles/204272989-Offline-Getting-Started-and-Manual-pdf, from Pix4D Support.

Poirier, E., van Proosdij, D., & Milligan, T. G. (2017). The effect of source suspended sediment concentration on the sediment dynamics of a macrotidal creek and salt marsh. *Continental Shelf Research, 148*, 130-138. doi:10.1016/j.csr.2017.08.017

Porter, C., Lundholm, J., Bowron, T., Lemieux, B., van Proosdij, D., Neatt, N., & Graham, J. (2015). Classification and environmental correlates of tidal wetland vegetation in Nova Scotia, Canada. *Botany, 93*(12), 825-841. doi:10.1139/cjb-2015-0066

Province of Nova Scotia. (2017, 12 10). Nova Scotia's Wetlands. Retrieved from Nova Scotia Canada: https://novascotia.ca/nse/wetland/

Robin, C., Nudds, S., Macaulay, P., Godin, A., de Lange Boom, B., & Bartlett, J. (2016). Hydrographic Vertical Separation Surfaces (HyVSEPs) for the Tidal Waters of Canada. *Marine Geodesy, 39*(2), 195-222. doi:10.1080/01490419.2016.1160011

Rokitnicki-Wojcik, D., Wei, A., & Chow-Fraser, P. (2011). Transferability of object-based rule sets for mapping coastal high marsh habitat among different regions in Georgian Bay, Canada. *Wetlands Ecological Management, 19*, 223–236. doi:10.1007/s11273-011-9213-7

Roman, C. T., & Burdick, D. M. (2012). *Tidal Marsh Restoration - A Synthesis of Science and Management*. (C. T. Roman, & D. M. Burdick, Eds.) Washington, DC: Island Press.

Rougier, S., Puissant, A., Stumpf, A., & Lachiche, N. (2016). Comparison of sampling strategies for object-based classification of urban vegetation from Very High Resolution satellite images. *International Journal of Applied Earth Observation and Geoinformation, 51*, 60-73. doi:10.1016/j.jag.2016.04.005

Sadro, S., Gastil-Buhl, M., & Melack, J. (2007). Characterizing Patterns of Plant Distribution in a southern California salt marsh using remotely sensed topographic and hyperspectral data and local tidal fluctuations. *Remote Sensing of Environment, 110*(2), 226-239. doi:10.1016/j.rse.2007.02.024

Schmidt, K. S., & Skidmore, A. K. (2003). Spectral discrimination of vegetation types in a coastal wetland. *Remote Sensing of Environment, 85*(1), 92-108. doi:10.1016/S0034-4257(02)00196-7

Sentera. (2017). Retrieved from http://www.cybernetech.co.jp/pdf/precision_ndvi_single_sensor.pdf

Sentera. (n.d.). sentera. Retrieved from The Sentera High-Precision Single Sensors: https://sentera.com/wp-content/uploads/2018/01/Single_NDRE_NDVI_Lit4064A_WEB.pdf

Shaw, J., Taylor, R. B., Forbes, D. L., Ruz, M.-H., & Solomon, S. (1998). *Sensitivity of the Coasts of Canada to Sea-Level Rise*. Geological Survey of Canada Bulletin 505. Ottawa: Natural Resources Canada. doi:https://doi.org/10.4095/210075

Silvestri, S., Marani, M., Settle, J., Benvenuto, F., & Marani, A. (2002). Salt marsh vegetation radiometry - Data analysis and scaling. *Remote Sensing of Environment, 80*(3), 473-482. doi:10.1016/S0034-4257(01)00325-X

Sim, J., & Wright, C. C. (2005). The Kappa Statistic in Reliability Studies: Use, Interpretation, and Sample Size Requirements. *Physical Therapy, 85*(3), 257-268. doi:10.1093/ptj/85.3.257

Simmons, M., Davis, D., Griffiths, L., & Muecke, A. (1984). *Natural History of Nova Scotia* (Vol. 2). Halifax: Nova Scotia Department of Education and Department of Lands and Forests.

Singh, K., Walters, B. B., & Ollerhead, J. (2007). Climate Change, Sea-Level Rise and the Case for Salt Marsh Restoration in the Bay of Fundy, Canda. *Environments, 35*(2), 71-84.

Smith, G. M., & Milton, E. J. (1999). The use of the empirical line method to calibrate remotely sensed data to reflectance. *International Journal of Remote Sensing, 20*(13), 2653-2662. doi:10.1080/014311699211994

Stehman, S. V., & Wickham, J. D. (2011). Pixels, blocks of pixels, and polygons: Choosing a spatial unit for thematic accuracy assessment. *Remote Sensing of Environment, 115*, 3044-3055. doi:10.1016/j.rse.2011.06.007

Stuckens, J., Coppin, P. R., & Bauer, M. E. (2000). Integrating contextual information with per-Pixel Classification for Improved Land Cover Classification. *Remote Sensing of Environment, 71*(3), 282-296. doi:10.1016/S0034-4257(99)00083-8

Temmerman, S., Govers, G., Wartel, S., & Meire, P. (2003). Spatial and temporal factors controlling short-term sedimentation in a salt and freshwater tidal marsh, Scheldt Estuary, Belgium, SW Netherlands. *Earth Surface Processes and Landforms, 28*, 739-755. doi:10.1002/esp.495

Tibbetts, J. R., & van Proosdij, D. (2013). Development of a relative coastal vulnerability index in a macro-tidal environment for climate change adaptation. *Journal of Coastal Conservation, 17*(4), 775-797. doi:10.1007/s11852-013-0277-9

Tilley, D. R., Ahmed, M., Son, J. H., & Badrinarayanan, H. (2007). Hyperspectral Reflectance Response of Freshwater Macrophytes to Salinity in a Brackish Subtropical Marsh. *Journal of Environmental Quality, 36*(3), 780-9. doi:10.2134/jeq2005.0327

Timm, B. C., & McGarigal, K. (2012). Fine-scale remotely-sensed cover mapping of coastal dune and salt marsh ecosystems at Cape Cod National Seashore using Random Forests. *Remote Sensing of Environment, 127*, 106–117. doi:10.1016/j.rse.2012.08.033

Tiner, R. W. (2013). *Tidal Wetlands Primer - An Introduction to Their Ecology, Natural History, Status, and Conservation*. Amherst and Boston: University of Massachusetts Press.

van Beijma, S., Comber, A., & Lamb, A. (2014). Random forest classification of salt marsh vegetation habitats using quad-polarimetric airborne SAR, elevation and optical RS data. *Remote Sensing of Environment, 149*, 118-129. doi:10.1016/j.rse.2014.04.010

van Proosdij, D., & Page, S. (2012). *Best Management Practices for Climate Change Adaptation in Dykelands: Recommendations for Fundy ACAS sites*. Department of Geography, Saint Mary's University and CBWES Inc. Halifax: Atlantic Climate Adaptation Solutions Association. doi:10.13140/2.1.3113.0405

van Proosdij, D., Milligan, T., Bugden, G., & Butler, K. (2009). A Tale of Two Macro Tidal Estuaries: Differential Morphodynamic Response to the Intertidal Zone to Causeway Construction. *Journal of Coastal Research, SI:56*, 772-776.

van Proosdij, D., Ross, C., & Matheson, G. (2018). *Risk Proofing Nova Scotia Agriculture: A Risk Assessment System Pilot (AgriRisk)*. Maritime Provinces Spatial Analysis Research Centre, Department of Geography and Environmental Studies. Halifax: Saint Mary's University.

Warner, B. G., & Rubec, C. D. (1997). *The Canadian Wetland Classification System* (2nd ed.). (Authors, Ed.) Waterloo, ON, Canada: Wetland Research Centre, University of Waterloo.

Watts, A. C., Bowman, W. S., Abd-Elrahman, A. H., Mohamed, A., Wilkinson, B. E., Perry, J., . . . Lee, K. (2008). Unmanned Aircraft Systems (UASs) for Ecological Research and Natural-Resource Monitoring (Florida). *Ecological Restoration, 26*, 13-14. doi:10.3368/er.26.1.13

Webster, T., McGuigan, K., & MacDonald, C. (2011). *Lidar processing and Flood Risk Mapping for Coastal Areas in the District of Lunenburg, Town and District of Yarmouth, Amherst, Count Cumberland, Wolfville and Windsor*. Nova Scotia Community College, Centre of Geographic

Science, Applied Geomatics Research Group. Middleton: Atlantic Climate Solutions Association (ACASA). Retrieved from https://atlanticadaptation.ca/en/islandora/object/acasa%3A448

Woodcock, C. E., & Strahler, A. H. (1987). The factor of scale in remote sensing. *Remote Sensing of Environment, 21*(3), 311-332. doi:10.1016/0034-4257(87)90015-0

Ye, S., Pontius, R. G., & Rakshit, R. (2018). A review of accuracy assessment for object-based image analysis: From per-pixel to per-polygon approaches. *ISPRS Journal of Photogrammetry and Remote Sensing, 141*, 137–147. doi:10.1016/j.isprsjprs.2018.04.002

Yoon-Kyung, L., Jeong-Won, P., Jong-Kuk, C., Yisok, O., & Joong-Sun, W. (2012). Potential uses of TerraSAR-X for mapping herbaceous halophytes over salt marsh and tidal flats. *Estuarine, Coastal and Shelf Science, 115*, 366-376. doi:10.1016/j.ecss.2012.10.003

Yu, L., Liang, L., Wang, J., Zhao, Y., Cheng, Q., Hu, L., . . . Gong, P. (2014). Meta-discoveries from a synthesis of satellite-based land-cover mapping research. *International Journal of Remote Sensing, 35*(13), 4573–4588. doi:10.1080/01431161.2014.930206

Yu, Q., Gong, P., Clinton, N., Biging, G., Kelly, M., & Schirokauer, D. (2006). Object-based Detailed Vegetation Classification with Airborne High Spatial Resolution Remote Sensing Imagery. *Photogrammetric Engineering and Remote Sensing, 72*(7), 799-811. doi:10.14358/PERS.72.7.799

Zhao, J., Niu, Y., Lu, Z., Yang, J., Li, P., & Liu, W. (2018). Applicability assessment of UAVSAR data in wetland monitoring: A case study of Louisiana wetland. *The International Archives of the Photogrammetry, Remote Sensing and Spatial Information Sciences, XLII*-3, 2375–2378. doi:10.5194/isprs-archives-XLII-3-2375-2018

Zimmerman, P. L., Housman, I. W., Perry, C. H., Chastain, R. A., Webb, J. B., & Finco, M. V. (2013). An accuracy assessment of forest disturbance mapping in the western Great Lakes. *Remote Sensing of Environment, 176-185*. doi:10.1016/j.rse.2012.09.017

Zweig, C. L., Burgess, M. A., Percival, F. H., & Kitchens, W. M. (2015). Use of Unmanned Aircraft Systems to Delineate Fine-Scale Wetland Vegetation Communities. *Wetlands, 35*, 303–309. doi:10.1007/s13157-014-0612-4

Appendix I

Site Name / ID:_____ Field Day No: ____ Date:_____

Loc_

Name:

RTK ID: _____ RTK ID: _____

Height: Height:

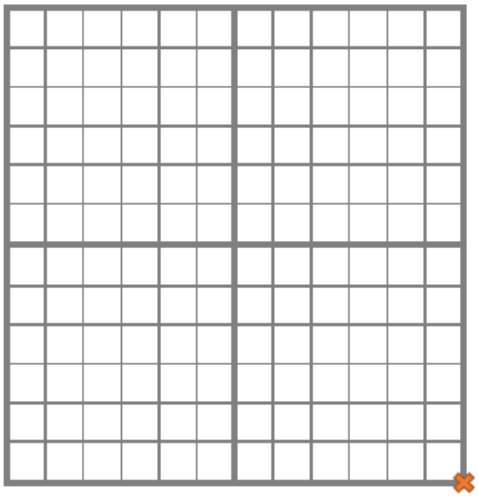

RTK ID: _____ RTK ID: _____

Height: Height:

DETAILS ABOUT MS IMAGES (LOW ALTITUDE):	
TIME	
CLOUD COVERAGE	
WEATHER CONDITION	
FOLDER OF IMAGERY	

Pic IDs with description:

Appendix II

```
from PIL import Image
from PIL import ImageFilter
import os

origin='C:\\Users\\[redacted]\\'
destination='C:\\Users\\[redacted]\\BandIsolated1\\'

os.makedirs(destination)
for x in range (9,17):
    folder='imagery_'
    for d in range (4-len(str(x))):
        folder=folder+'0'
    folder=folder+str(x)
    os.makedirs(destination+folder)
    for file in os.listdir(origin+folder):
        if file.endswith('.jpg'):
            im=Image.open(origin+folder+'\\'+file)
            exif=im.info['exif']
            img=im.load()
            [xs,ys]=im.size
            for x in range (xs):
                for y in range (ys):
                    [r,g,b]=img[x,y]
                    newR=1.0*r-1.012*b
                    newB=9.605*b-0.618*r
                    img[x,y]=(int(newR),int(newR),int(newB))

            #im=im.filter(ImageFilter.SMOOTH)
            im.save(destination+folder+'\\'+file, exif=exif)
```

Appendix III

Calculating distance following the Pythagoras Theorem:

$$X\ Difference\ [\boldsymbol{X\ Diff}] = X_{P1} - X_{P3}$$

$$Y\ Difference\ [\boldsymbol{Y\ Diff}] = Y_{P1} - Y_{P3}$$

$$Distance = \sqrt[2]{(X\ Diff)^2 + (Y\ Diff)^2}$$

$$Side = \left(\sin \frac{(45 \times \pi)}{180}\right) \times Distance$$

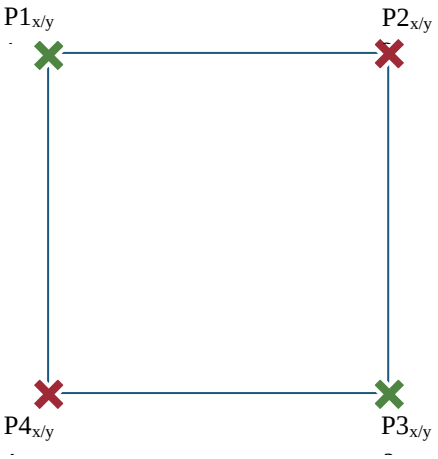

Calculate Bearing with the use of ARCTAN:

$$Bearing\ (Rad)\ [\boldsymbol{BR}] = \tan^{-1}\frac{X\ Diff}{Y\ Diff}$$

$$Bearing\ (Deg)[\boldsymbol{BD}] = BR \times \frac{180}{\pi}$$

$$Bearing\ Side\ 1\ [\boldsymbol{BS1}] = BD - 45$$

$$Bearing\ Side\ 2\ [\boldsymbol{BS2}] = BD + 45$$

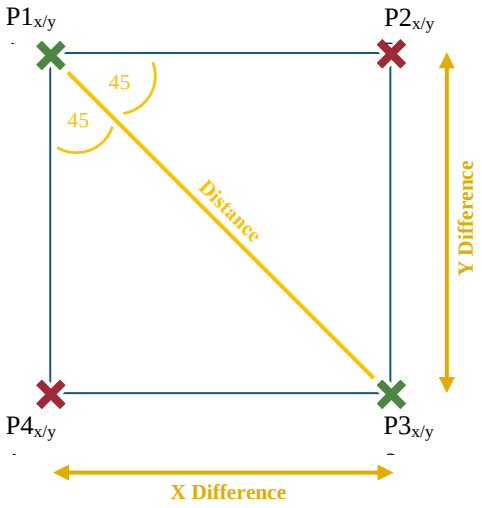

Calculate missing coordinates:

$$\boldsymbol{X_{P2}} = \left(Side \times \left(\sin \frac{(BS1 \times \pi)}{180}\right)\right) + X_{P1}$$

$$\boldsymbol{Y_{P2}} = \left(Side \times \left(\cos \frac{(BS1 \times \pi)}{180}\right)\right) + Y_{P1}$$

$$\boldsymbol{X_{P4}} = \left(Side \times \left(\sin \frac{(BS2 \times \pi)}{180}\right)\right) + X_{P1}$$

$$\boldsymbol{Y_{P4}} = \left(Side \times \left(\cos \frac{(BS2 \times \pi)}{180}\right)\right) + Y_{P1}$$

Appendix IV

Figure AIV.1: Overview of post-breach orthomosaic in true colour composite.

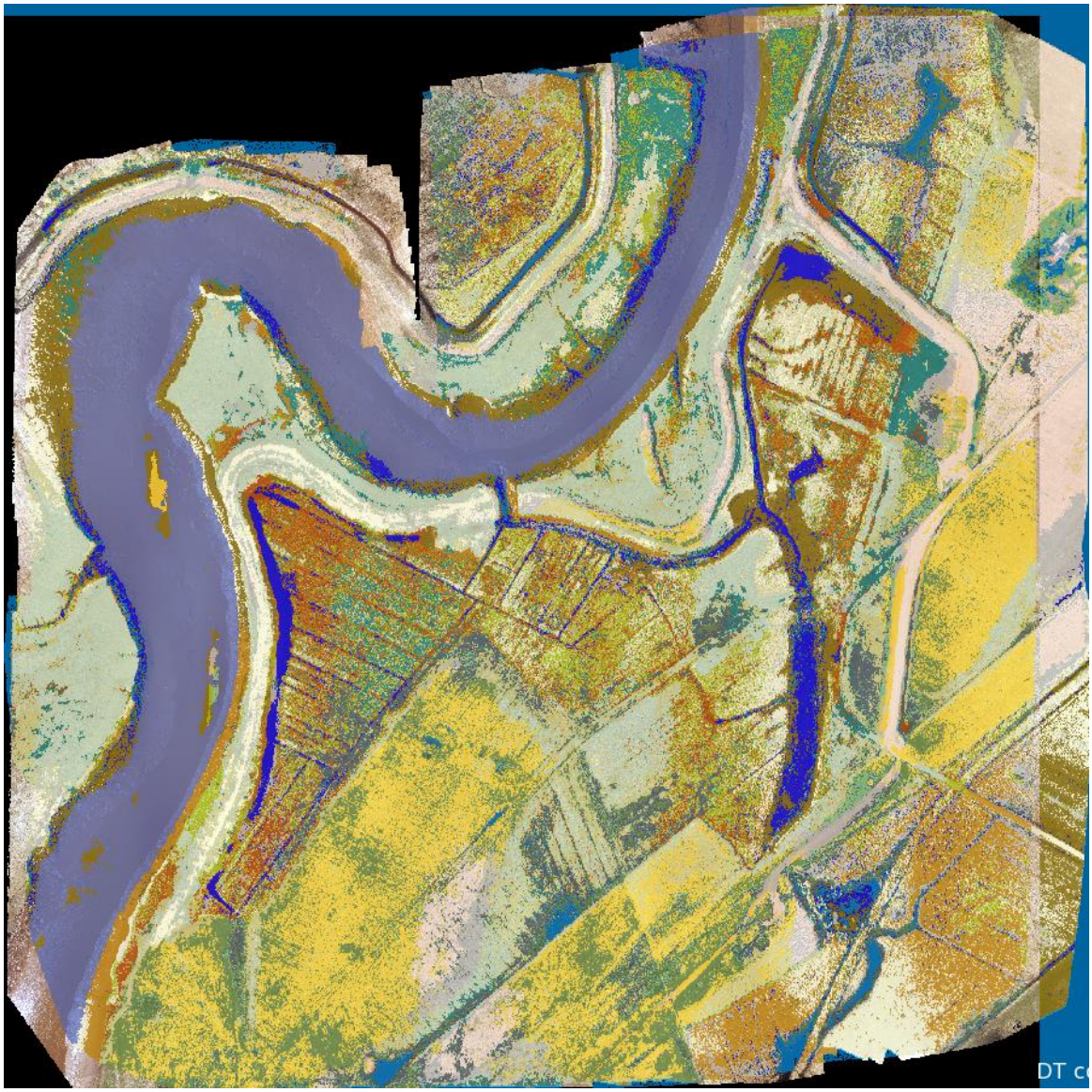

Figure AIV.2: Classification output of Decision Tree algorithm.

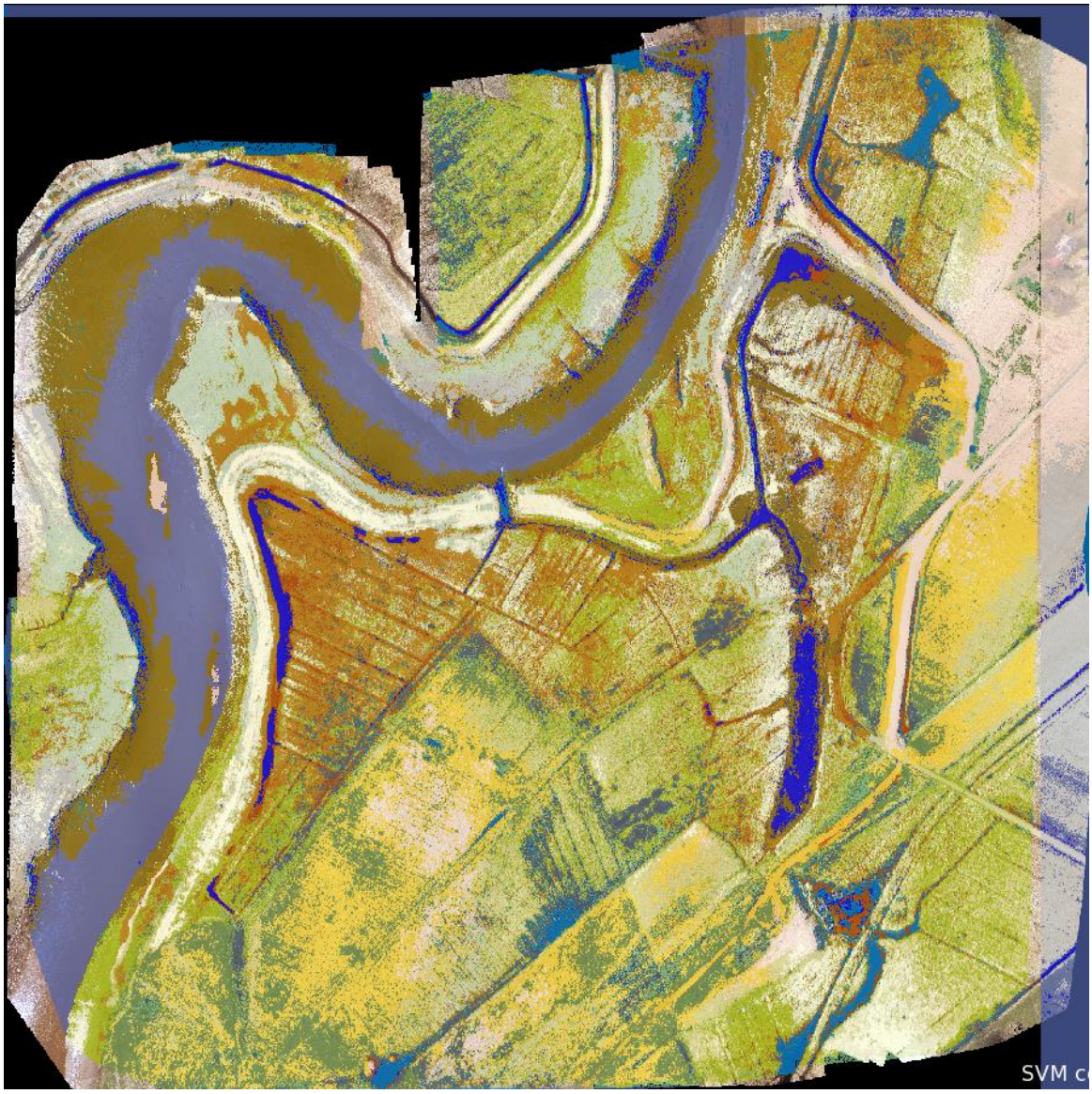

Figure AIV.3: Classification output of Support Vector Machine algorithm with linear kernel.

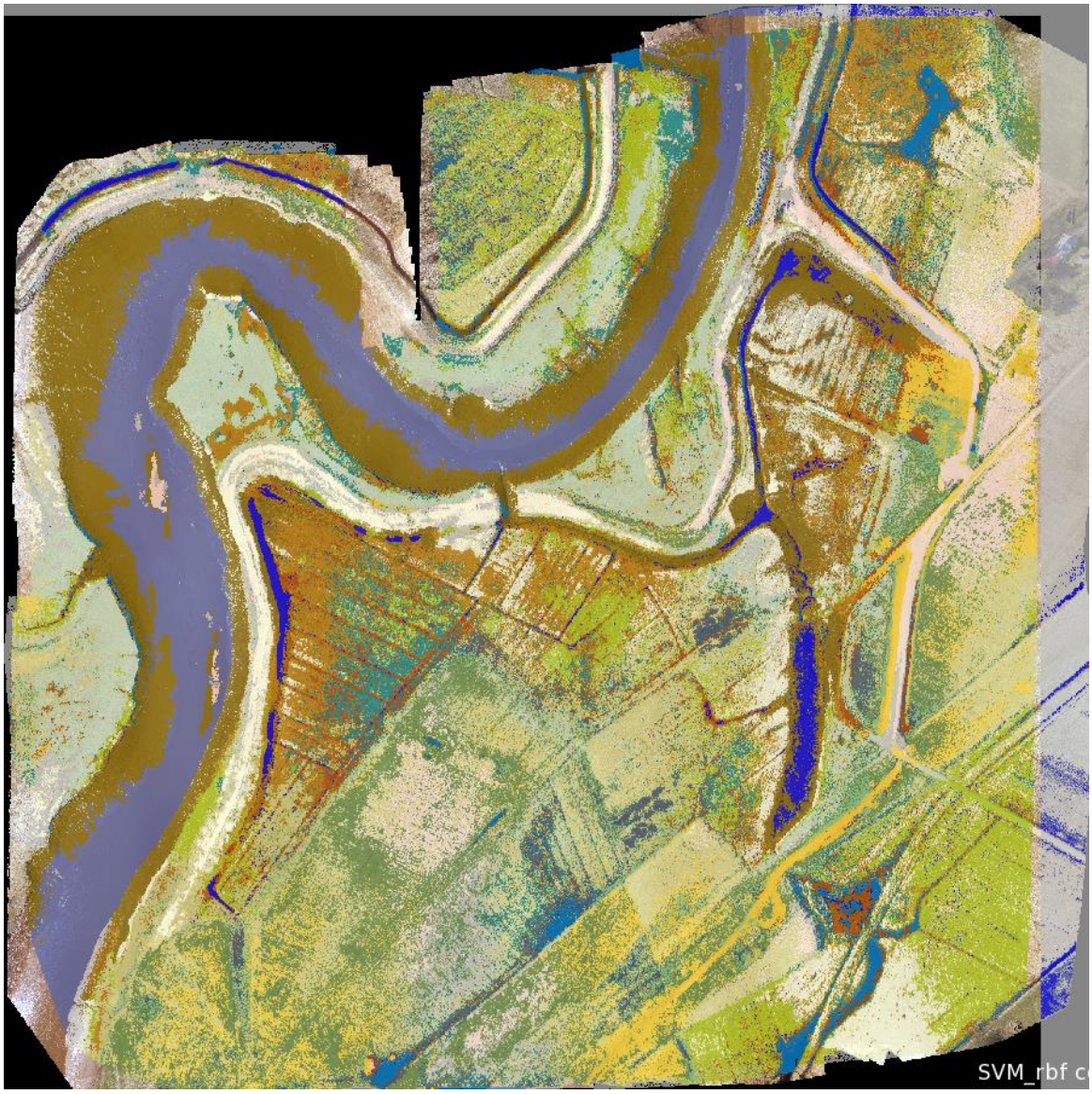

Figure AIV.4: Classification output of Support Vector Machine algorithm with RBF kernel.

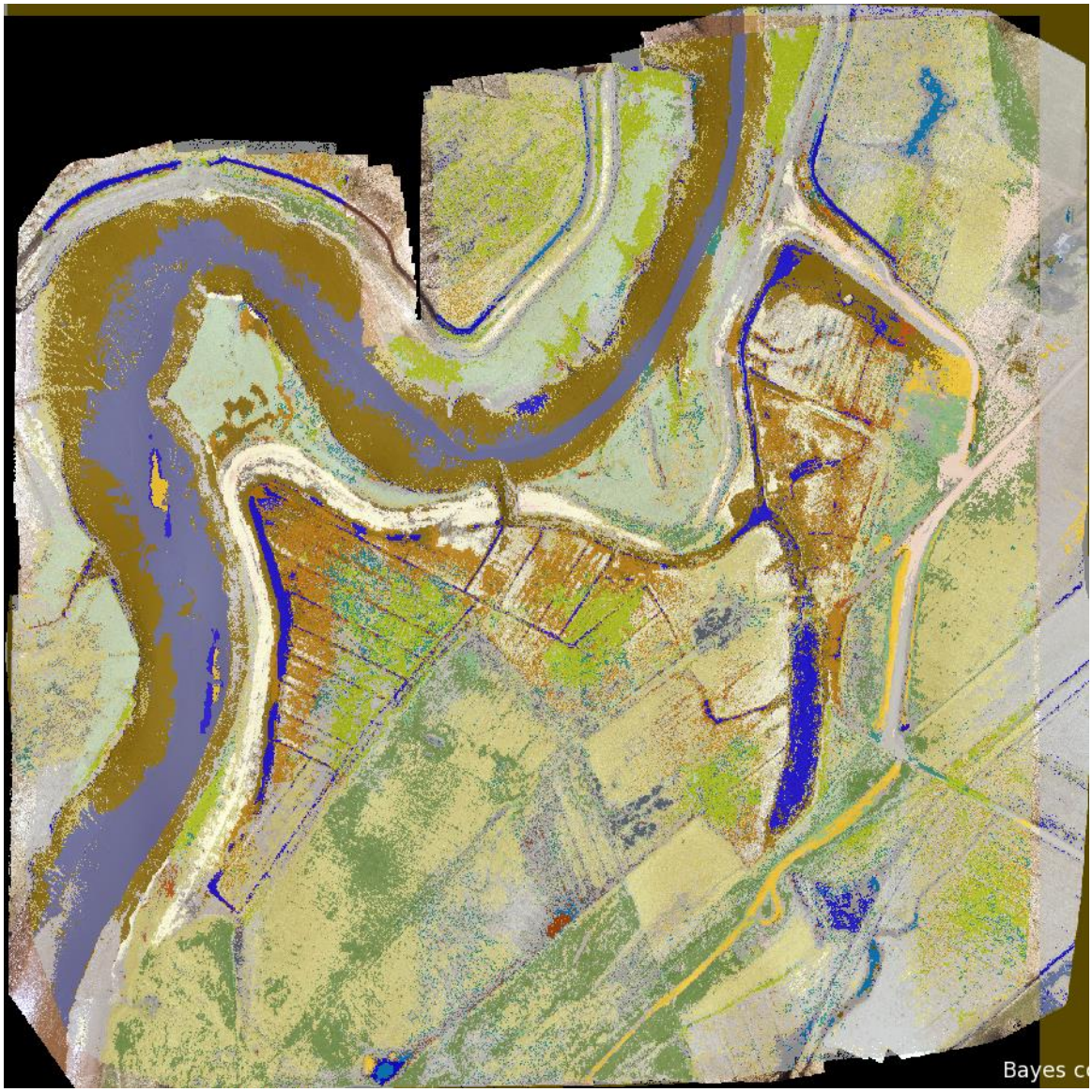

Figure AIV.5: Classification output of the Bayes algorithm.